DISS. ETH NO. 24531

DESIGN AND CHARACTERIZATION OF A COMPACT HYBRID FMT-MRI SYSTEM

A thesis submitted to attain the degree of

DOCTOR OF SCIENCES of ETH ZURICH

(Dr. sc. ETH Zurich)

presented by

ANDREAS ELMER
MSc Microengineering, EPF Lausanne

born on 19.03.1985

citizen of Glarus Süd GL

accepted on the recommendation of

Prof. Dr. Markus Rudin, examiner
Prof. Dr. Martin Wolf, co-examiner

2017

Zusammenfassung

Multimodale Bildgebung, die strukturelle, funktionelle, metabolische und/oder molekulare Informationen liefert, ermöglicht neue Arten der Visualisierung von Krankheitsmechanismen und der Überwachung von Therapieeffekten. Ein attraktives multimodales Bildgebungssystem für Studien mit Kleinnagern ist die Kombination von Fluoreszenztomographie (FT) und Magnetresonanztomographie (MRT). FT bietet eine hohe Empfindlichkeit und liefert molekulare Informationen, indem es die Verteilung von fluoreszierenden Stoffen in lebenden Tieren quantifiziert. Ausserdem gibt es für FT eine breite Palette an Fluoreszenzproben, welche in der Mikroskopie häufig verwendet werden. MRT erzeugt mit einer hohen Auflösung gute Kontraste für Weichteile und kann funktionelle Informationen liefern. Deshalb bildet eine Kombination von FT und MRT ein äusserst potentes Bildgebungssystem für präklinische Studien. Zusätzlich können vom MRT-System gewonnene strukturelle Informationen mitberücksichtigt werden, um die Rekonstruktion der FT, ein ‘’inkorrekt gestelltes Problem’’, zu lösen, was zu einer verbesserten Rekonstruktionsgenauigkeit der Fluorophor-Verteilung führen sollte.

Die Machbarkeit dieses Ansatzes wurde mit einer ersten Generation eines Hybrid-FT-MRT-Systems (FMT-MRI 1.0) aufgezeigt. Dieses System wies technische Nachteile auf, wie zum Beispiel eine kleine Bildsensorgrösse des Detektors, ein eingeschränktes Sichtfeld, eine tiefe Empfindlichkeit, eine limitierte Eindringtiefe und eine schwierige und instabile Handhabung, die das System für biologische Studien ungeeignet machten.

Das Ziel dieser Doktorarbeit war, diese Probleme anzugehen und das FT-MRT-System weiterzuentwickeln. Die Zielsetzung war, ein kompaktes Hybrid-FT-MRT-System zu entwerfen, das für Routineanwendungen geeignet ist. Die grössten Herausforderungen bei der Entwicklung eines FT-Einsatzes für einen 9.4T MRT-Scanner für Kleintiere waren die knappen Platzverhältnisse, die Einwirkung durch das starke magnetische Feld und schwierige elektromagnetische Interferenzbedingungen (EMI). Zudem sollte auch die Empfindlichkeit der Fluoreszenzdetektion erhöht werden. Dies wurde durch ein System der zweiten Generation (FMT-MRI 2.0) erreicht, das einen neuen, empfindlichen, gekühlten und abgeschirmten CMOS-Detektor enthielt. Die Installation wurde auf ein lineares Führungssystem befestigt, damit der FT-Einsatz stabil eingeführt werden konnte.

Die Verbesserungen wurde in einem Experiment aufgezeigt, welches die vaskulären Eigenschaften (Blutvolumen, vaskuläre Permeabilität) eines Maus-Tumor-Modells erfasste. Tumorangiogenese ist ein wichtiger Schritt in der Entwicklung eines Tumors. Sich neu bildende Gefässe sind typischerweise chaotisch, weisen eine grosse Fenestration auf und sind also undicht. Die Beurteilung der vaskulären Permeabilität von Tumoren hat sich zu einer wichtigen Methode für die Diagnose und zur Überprüfung von Therapieeffekten entwickelt. Die klinische Standardmethode hierfür ist die dynamisch-

kontrastverstärkte MRT (DCE-MRI), die das Austreten von Kontrastmittel misst, das normalerweise auf Gadolinium basiert. Der Zweck unserer Studie war, zu evaluieren, ob durch die Verwendung von preiswerten Bildgebungsverfahren, wie die Fluoreszenzbildgebung, die vermehrt erhältlich wird, analoge Informationen gewonnen werden können. Die Studie wurde mit Mäusen durchgeführt, die subkutan implantierte Brusttumore aufwiesen. Die vaskuläre Permeabilität wurde durch das simultane Messen von MRT- und Fluoreszenzsignalen erfasst, nachdem eine Mischung des Fluoreszenzfarbstoffs Cy5.5 und des MRT-Kontrastmittels GdDOTA verabreicht wurde. Die Resultate zeigten, dass beide Arten identische Resultate lieferten, abgesehen von der besseren räumlichen Auflösung der MRT. Zusätzlich benutzten wir eine Mischung der intravaskulären Substanzen Endorem (Ionennanopartikel) und Angiosense, um die Perfusion zu messen. Wiederum war die Übereinstimmung zwischen den zwei Modalitäten ausgezeichnet, was den Wert der Fluoreszenzbildgebung für die Charakterisierung der Neoangiogenese in Tumoren unterstreicht.

Während der neue Kameraaufbau die nötige Empfindlichkeit für biologische Anwendungen mitbrachte, benötigte das System noch immer eine mühsame und zeitaufwändige Kalibrierung vor der Datenerhebung. Deshalb wurde ein völlig neu gestaltetes Hybrid-FT-MRT System der dritten Generation (FMT-MRI 3.0) entwickelt, mit Fokus auf einfachere und schnellere Handhabung, höhere Empfindlichkeit und verbesserte Stabilität, Leistung und Vielseitigkeit.

Die Hauptkomponenten des FT-Systems, d.h. die Kollimatoren, die Laserscanner-Geräte und der Bilddetektor sind in einer fixierten geometrischen Anordnung in einer stabilen Box montiert, dem FT-Einsatz, der in den MRT-Scanner eingeschoben werden kann. Dies vereinfacht die Bedienung drastisch, da der mühsame Kalibrationsschritt vor einer FT-Messung nicht mehr benötigt wird. Ein solches Design erfordert, dass alle Komponenten innerhalb des FT-Einsatzes miniaturisiert und MRT-kompatibel sind.

Die Laserquelle befindet sich noch immer ausserhalb des Magnets und der Laserstrahl wird mittels einer Monomodefaser zum FT-Einsatz geleitet, mit einer GRIN-Linse kollimiert und auf einen kleinen MEMS-Spiegel gelenkt, damit die Lichtquelle die Probenoberfläche abtasten kann. Zwei MEMS-Spiegel sind verwendet worden, um eine Systembedienung im Reflektions- und Transmissionsmodus zu ermöglichen.

Das Fluoreszenzlicht, das von der Probe emittiert wird, wird mit einem sCMOS-Bildsensor (sCMOS: engl. für scientific CMOS), einem neuen Detektor mit verbesserten Spezifikationen, unter anderem in Bezug auf Quanteneffizienz, Auslese-Rauschen und Pixelauflösung, aufgenommen. Eine selbstgebaute Kühlungseinheit, die auf einem thermoelektrischen Kühler basiert, reduziert das Dunkelstrom-Rauschen und erhöht damit weiter die Empfindlichkeit des Sensors. Ein selbstgebautes und mit einem 3D-Drucker produziertes Kameragehäuse, mittels physikalischer Dampfablagerung mit einem 2.5 µm dünnen Film aus Aluminium beschichtet, reduziert elektrisches Übersprechen des Kameraelements

bestehend aus dem sCMOS-Sensor und den entsprechenden Schaltkreisen mit dem MRT-System. Eine Fischaugenlinse, welche die Fokalebene mit der Probenoberfläche abgleicht, gewährt ein genügend grosses Sichtfeld; die intrinsische Verzerrung, die mit dieser Linse einhergeht wird digital korrigiert.

Die Probe wird auf einer Auflage platziert, die mit einem Anästhesiegerät und stereotaktischer Fixierung ausgestattet ist, welche für eine komfortable Handhabung der Maus seitlich vom FT-Einsatz entfernt werden kann. Ein neues optisches Filter-Modul vereinfacht die Filterhandhabung, um die Bandpass-Filter für den gewünschten Spektralbereich auszuwählen. Der FT-Einsatz enthält eine Transceiver-Radiofrequenz-Oberflächenspule (verwendet kapazitive Kopplung) mit einem rechteckigen Fenster, das für die Detektion von Fluoreszenzsignalen benötigt wird. Für den Betrieb des FT-Systems wurde ein einfach bedienbares MATLAB-basiertes Programm entwickelt.

Die technische Systemcharakterisierung zeigte bezüglich der MEMS-Spiegel-basierten Lichtquellenpunkte-Abtastung einen hohen Grad an Reproduzierbarkeit auf mit Standardabweichungen der Lichtquellenpunkte-Position, die weit unter der Breite des Laserstrahls waren, sowohl mit, wie auch ohne statischem Magnetfeld (9.4T). Allerdings war das Abtastungsraster bei der Aufzeichnung von MRT-Daten stark verzerrt. Dies ist höchstwahrscheinlich mechanischen Vibrationen zuzuschreiben, die durch den Wechsel von Gradientenströmen in hohen magnetischen Feldern verursacht werden. Korrekturmassnahmen beinhalten eine Reduktion der Rauschquelle durch die Verwendung von „stillen“ Gradienten oder der Reduktion der Schwingungsanfälligkeit des Laserscanners durch eine Dämpfung der Halterung des FT-Einsatzes, durch den Gebrauch von MEMS-Spiegel mit anderen Resonanzeigenschaften, oder durch die Synchronisierung der FT-Datenerfassung mit der MRT-Sequenz durch die Ausnützung von Intervallen in der MRT-Erfassung, die keinen Gradientwechsel haben.

Erste Experimente mit einem Phantom, wie auch erste in vivo Experimente haben gezeigt, dass die Anforderungen des kompakten Designs weitgehend erfüllt worden sind: eine einfach Handhabung, eine hohe Empfindlichkeit, das Vorhandensein von Reflektions- und Transmission-Modus und gute MRT-Bildqualität. Weitere Verbesserungen sind nötig bezüglich der Interferenz der MRT-Datenerfassung mit dem Lichtquellenpunkteraster-Abtasten. Der offensichtlichste Ansatz hierfür ist die Synchronisierung der zwei Messungen, um Zeitfenster zu nutzen, die keinen Gradientwechsel aufweisen.

Zusammenfassend ist das FMT-MRI 3.0 ein neuartiger Ansatz eines Hybrid-FT-MRT-Systems mit einem kompakten Design, deutlich vereinfachter Handhabung und verbesserter System-Gesamtleistung. Es birgt grosses Potential für molekulare Bildgebung in Kleintieren mit vielversprechenden zukünftigen Anwendugen in der biomedizinischen Grundlagenforschung wie dem Nachweis und der Charakterisierung von Krankheitsphänotypen und die Auswertung neuer Therapien.

Summary

Multimodality imaging providing structural, functional, metabolic and/or molecular information offers new possibilities for visualization of diseases mechanism and monitoring the effect of therapy. An attractive multimodality imaging system for experimental studies in small rodents is the combination of both fluorescence molecular tomography (FMT) and magnetic resonance imaging (MRI). FMT features high sensitivity and can yield molecular information by delivering quantitative information on the distribution of fluorophores inside living animals. Moreover, it comes with a broad range of fluorescent probes, which have been extensively used in microscopy. As MRI provides good soft tissue contrast with high resolution and can deliver functional information, the combination of FMT and MRI should constitute a powerful imaging system for preclinical studies. In addition, use of prior structural information derived from the MRI system can be included when solving the ill-posed reconstruction problem of FMT, which should lead to improved reconstruction accuracy of the fluorophore distribution.

A first generation hybrid FMT-MRI system (FMT-MRI 1.0) was used to demonstrate feasibility of the approach. Yet, the system suffered from technical limitations such as small array size of the detector, limited field-of-view (FOV), low sensitivity, limited depth penetration and difficult and non-robust handling, which made the system unpractical for biological studies.

The aim of this PhD thesis was to address these issues and further develop FMT-MRI. The goal was the design and construction of a compact hybrid FMT-MRI suited for routine application. The main challenges in developing an FMT insert for a 9.4T small animal MRI scanner were space constraints and exposure to the strong magnetic field and challenging electromagnetic interference (EMI) conditions. In addition, the sensitivity of fluorescence detection should be increased. This was achieved in a 2nd generation system (FMT-MRI 2.0), which included a now sensitive cooled and shielded CMOS detector. The setup was mounted to a linear guiding system for robust insertion of the FMT probe.

The enhanced performance was demonstrated in a study assessing vasculature properties (blood volume, vascular permeability) in a murine tumor model. Tumor neoangiogenesis is an important step in the development of tumors. The newly formed vessels are typically chaotic, show large fenestration, and are hence leaky. Assessing tumor vascular permeability has emerged as important method for diagnosis and for monitoring therapy response. The standard clinical method for this is dynamic contrast enhanced MRI (DCE-MRI), which measures the extravasation of typically gadolinium-based contrast agents. This method is inherently translational. The purpose of our study was to evaluate whether analogous information can be obtained using low-cost imaging modalities such as fluorescent imaging, which will be increasingly available. The study was performed in mice carrying subcutaneous

implanted mammary tumors. Vascular permeability was assessed by simultaneously monitoring changes in MRI and fluorescence signals following the administration of a mixture of the fluorescent dye Cy5.5 and the MRI contrast agent GdDOTA. The results revealed that both modalities yielded identical results apart from the superior spatial resolution of MRI. In addition, we used a mixture of the intravascular agents Endorem (iron nanoparticles) and Angiosense to measure perfusion. Again, there was excellent correspondence between the two modalities demonstrating the value of fluorescence imaging for characterizing neoangiogenesis in tumors.

While the new camera setup provided the sensitivity necessary for biological applications, the system still required tedious and time-consuming calibration prior to data collection. Therefore, a completely redesigned 3rd generation hybrid FMT MRI system (FMT-MRI 3.0) was developed with a focus on simpler and faster handling, higher sensitivity and an increased robustness, power and versatility.

The basic idea is a system-in-a-box design. The main components of the FMT system, i.e. the beam collimator, the scanning device(s) and the image detector are mounted in a fixed geometry arrangement in a rigid box, the FMT probe, which can be inserted into the MRI scanner. This drastically simplifies operation, since the cumbersome calibration step prior to a FMT measurement is not anymore required. Such a design requires all components within the FMT probe to be miniaturized and MRI-compatible.

The laser source is still located outside the magnet and the laser beam guided using a single-mode fiber to the FMT probe, collimated with a GRIN lens and directed onto a small MEMS mirror for scanning the light sources across the sample surface. Two MEMS mirrors have been used to enable system operation in reflection and transmission mode.

The fluorescent light emitted by the sample is recorded with a scientific CMOS (sCMOS) image sensor, a novel detector with improved specifications such as quantum efficiency, readout noise and pixel resolution. A home-built cooling module based on a thermoelectric cooler reduces the dark current noise, further enhancing the sensitivity of the sensor. An in-house manufactured camera casing produced with a 3D printer and coated with a 2.5 µm thin film of aluminum using physical vapor deposition reduces cross-talk of the camera module consisting of the sCMOS sensor and the corresponding circuitry with the MRI system. Use of a fish eye lens for adjusting the focal plan to the sample surface, warrants a sufficiently large FOV; the intrinsic distortion associated with this lens is corrected digitally.

The sample is positioned on a support equipped with anesthesia equipment and stereotactic fixation that can be removed laterally from the FMT probe for convenient preparation of the mouse. A new optical filter module simplifies filter manipulation for selecting the bandpass filters for the desired

spectral domain. The FMT probe comprised a radiofrequency surface transceiver coil with a rectangular window required for detection of fluorescence signals. Balanced coupling was used. FMT system operation was controlled by a MatLab based software tool designed in a user-friendly manner in order to be suited for operation by non-experts.

Technical system characterization demonstrated a high degree of reproducibility regarding MEMS-based source scanning with standard deviations in source position well below the width of the laser beam both in the presence and absence of a static magnetic field (9.4T). Yet, the scanning grid was heavily distorted when recording during an MRI data acquisition. This is most likely attributed to mechanical vibrations induced by the switching of gradient currents in a high magnetic field. Corrective measures include reduction of the noise source by use of 'silent' gradients or reduction of the sensitivity of the scanning devices by damping the FMT probe mount, by using MEMS with different resonance properties, or by synchronizing FMT data acquisition to MRI sampling by exploiting intervals in the MRI acquisition that are devoid of gradients switching.

First experiments using a phantom as well as a first in vivo experiment demonstrated that the requirements of the compact design have been largely met: ease of operation, high sensitivity, availability of both reflection and transmission mode and good MRI image quality. Further improvements are required regarding the interference of MRI data acquisition with laser source scanning. Here the most obvious approach is synchronization of the two measurements to exploit time windows that do not involve gradient switching.

In summary, the FMT-MRI 3.0 system is a novel approach of a hybrid FMT MRI system with a compact design and a clearly easier handling and improved overall system performance. It carries great potential for molecular imaging in small animals. Future promising applications are in basic biomedical research such as the detection and characterization of disease phenotypes and the evaluation of novel therapies.

Contents

Chapter 1

Introduction

1.1 Motivation

More than a century ago, in November 1895, Wilhelm Röntgen, an alumnus of the polytechnical school of Zurich, made a fascinating discovery: a new type of rays called X-rays were able to image the bones of his wife's hand (Fig. 1.1). The discovery quickly proved its value for diagnostics and emerged as an important tool for physicians [1, 2].

Fig. 1. 1 The first human radiograph showing Roentgen's wife's hand [1].

Since then many imaging modalities based on different physical principles have emerged helping physicians obtain more and more detailed anatomical and physiological information from within the human body. Today they constitute an indispensable tool for clinical diagnosis and for monitoring therapy responses. Imaging modalities provide information about structure and function of underlying tissue and distribution of compounds, which might specifically aggregate at a certain site and help to untangle the mechanism of diseases. Typically, anatomical and functional changes are late indicators of a pathologic process and moreover lack specificity. Final diagnosis often requires the histological analysis of a biopsy specimen, i.e. analysis at the cellular and molecular level. Hence, it would be attractive to visualize these molecular

characteristics in vivo. This is one objective of so-called molecular imaging techniques, which map the distribution of exogenous or endogenous molecular reporters indicating the presence of specific molecular targets. Molecular imaging gives an insight into processes happening at cellular scale level and provides quantitative information non-invasively in the living organism [3]. Examples of applications are imaging of gene expression, the product of genes and the pharmacokinetics and biodistribution of drugs used e.g. in oncology and neuroscience [3-8]. It may thus help to recognize diseases at an early stage prior to the occurrence of structural abnormalities [3]. It can improve costly and time-consuming drug development, e.g. by stratifying patient populations, by optimizing dose finding and by providing biomarkers as early readout of therapy response [6, 9]. Based on the physical principle imaging modalities differ with regard to spatial and temporal resolution provided, depth penetration, energy of radiation, sensitivity, and type and the nature of imaging probes [10] (Fig 1.2).

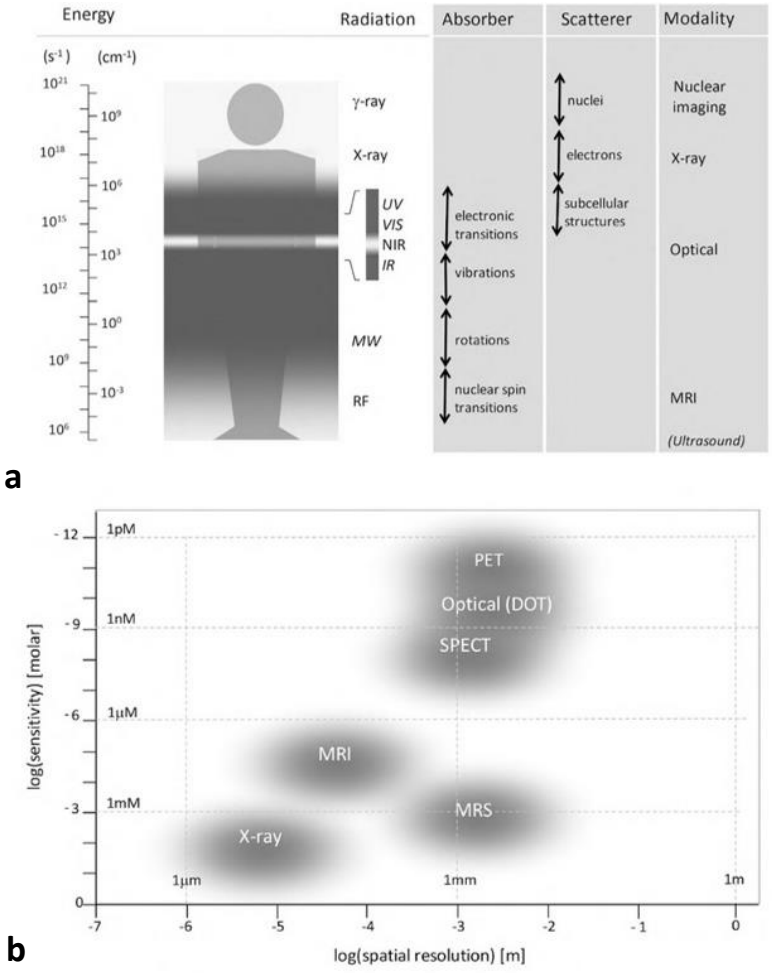

Fig. 1. 2 Comparison of different imaging modalities (a) Energy of radiation used in various imaging modalities. Nuclear imaging and x-ray modalities use ionizing radiation. Imaging modalites at lower radiation energy levels (optical, MRI using electromagnetic wave and ultrasound with acoustic wave) are non-ionzizing. (b) Graph showing spatial resolution and sensitivity of varous imaging modalities. Imaging modalities with high spatial resolution have low sensitivity and vice-versa. Images copied from [3].

Molecular imaging requires high sensitivity, since it images processes that happen at low frequency [3]. Examples of imaging modalities with high sensitivity are positron emission tomography (PET) and single photon emission computer tomography (SPECT), as well as bioluminescence and fluorescence based optical imaging modalities (Fig. 1.2b), which are also the most common modalities for molecular imaging. PET and SPECT are established imaging modalities in clinics; however they use ionizing radiation for imaging and the former requires expensive cyclotron for on-site production of the short-life radiopharmaceuticals [11].

Molecular imaging in small animals has emerged as an important field for basic research, development of novel imaging solutions, and for facilitating translation between in vitro research, experimental studies in animals and clinical applications [12]. While PET and SPECT are today available for and widely used in animal research, optical imaging has recently gained a lot of attention as the techniques are low cost, use non-ionizing radiation and stable tracers. Fluorescence microscopy is an indispensable tool for biologists for decades and a plethora of fluorescent probes and techniques have been developed. While giving access to structures at a scale of 100-200nm, the method suffers from a small field of view and very limited depth penetration of few hundred microns, which is due to scattering of the light inside the biological tissue [13]. However, it was discovered already in the late 1970s that light in the near-infrared (NIR) domain can penetrate brain tissue to remarkable depth [14]. NIR fluorescence imaging methods have been rapidly developed during the last two to three decades, including tomographic approaches such as diffuse optical tomography (DOT) [14-18] and fluorescence molecular tomography (FMT) [15, 19-21].

Both DOT and FMT assess the light distribution at the surface of the sample elicited by a point light source. Light propagation inside a highly scattering biological tissue is modeled by an approximation to the radiative transfer equation, the diffusion equation and is in many aspects analogous to the diffusion of particles [22, 23]. Yet the problem is ill-posed, similar to the problem of source reconstruction from EEG signals measured at the scalp [24]; and three-dimensional reconstruction of optical parameters (absorption and scattering coefficients, fluorescent dye distribution) is difficult and based on iterative procedures. Yet FMT provides high sensitivity and reconstruction of the three-dimensional distribution of fluorescent reporter gene/probe has been demonstrated, though the method suffers from low resolution due to high scattering of light and is prone to artifacts due to the ill-posed nature of the FMT reconstruction problem [25, 26]. Additional difficulties arise when objects are irregular and heterogeneous, as is the case e.g. when imaging intact organisms. Any additional information that would help to confine the problem better would be of great value. This sparked the interest in hybrid imaging techniques, i.e. the combination of a molecular imaging modality and an imaging modality that provides highly resolved structural information. The obvious combination is x-ray computer tomography (XCT) as PET-XCT instruments meanwhile belong to clinical standard-of-care [27, 28]. In fact FMT-XCT systems have been reported [29, 30] and first applications have demonstrated that incorporation of anatomical constraints significantly improved reconstruction quality [18, 31, 32].

Magnetic resonance imaging (MRI) is an attractive alternative to XCT, as it provides high-value soft-tissue contrast and may also add functional information. Similar to XCT, MR images can be used for prior information and improve FMT reconstruction in two ways: (i) introduction of geometrical constraints to FMT reconstruction (ii) segmentation and classification of tissues based on MR images and attributing tissue specific optical parameters. This should improve the accuracy of the light propagation modelling used in FMT reconstruction [13]. Development of a hybrid FMT-MRI system is challenging from an engineering point-of-view due to the strong static and transient magnetic fields involved and the resulting concerns regarding electromagnetic interference (EMI). Also, MR-compatible i.e. non-magnetic materials have to be used throughout [33]. Yet many examples have demonstrated that engineering of MRI compatible equipment is feasible: various electronic and mechanical systems working in MRI-scanners such as MR compatible robots or drills assisting surgeons during operations have been developed [34-38].

1.2 Fluorescence Molecular Tomography

In FMT, the distribution of a fluorescence reporter (e.g. fluorescence proteins, fluorescent quantum dots or fluorescence dyes) is determined inside a diffusive tissue. In a typical FMT protocol a laser scans a grid pattern on a biological tissue consecutively at both excitation and emission mode with a detector imaging at excitation and emission wavelength of a specific fluorescence reporter, respectively. The FMT raw data obtained reconstructs the 3D distribution of the fluorescence reporter using a diffusive light propagation model for biological tissues.

Photon propagation in a scattering medium is described using an ensemble perspective. Photon flux is described by the radiative transfer equation (RTE), which can be derived and approximated from the Maxwell's equation and simplifies modelling of light in scattering medium, since it is a scalar representation [39]. In a highly scattering tissue, which is typically the case in biological tissues, this equation is further simplified to the diffusion equation assuming that scattering is nearly isotropic after light has propagated some distance and provided the absorption coefficient is much smaller than the scattering coefficient ($\mu_a \ll \mu_s$), which is the case for biological tissue. [40].

The diffusion equation reads [3]:

$$\frac{1}{c}\frac{\partial}{\partial t}U(\vec{r},t) - \vec{\nabla}\cdot\left(D(\vec{r})\cdot\vec{\nabla}\big(U(\vec{r},t)\big)\right) + \mu_a \cdot U(\vec{r},t) = S_0(\vec{r},t) \qquad (1.1)$$

with the optical diffusion coefficient given by

$$D(\vec{r}) = \frac{1}{3(\mu_a(\vec{r})+\mu\prime_s(\vec{r}))} \qquad (1.2)$$

and the reduced scattering coefficient $\mu'_s = (1-g)\cdot\mu_s$, g being the anisotropy factor (g=0 for isotropic scattering), c the speed of light, S_0 a source term and U being the average light intensity.

The diffusive equation can be analytically solved for few homogeneous geometries (e.g. slab or cylinder), but has generally to be solved with numerical approximations (using e.g. finite element method), in the

case of biological samples [3]. This allows solving the forward problem: Calculating how light propagates from a given light source and knowing its intensity at a given position e.g of a biological tissue. The forward problem also calculates the excitation light intensity that reaches a fluorescence reporter knowing the source on the given tissue. The inverse problem, which is ill-posed in FMT, is the estimation of the light source (i.e. the fluorescence reporter) knowing the light that arrives at the detector. The source term in equation (1.1) can be replaced by

$$S_{em} = \eta c_{fl}(\overrightarrow{r}) U_{ex}(\overrightarrow{r}) \tag{1.3}$$

With η the quantum yield and c_{fl} the concentration of the fluorescence reporter and U_{ex} the light intensity that origins from the excitation source located at the fluorescent dye and obtained in the forward model. In continuous wave-mode equation (1.1) can be simplified and the diffusion equation at a specific fluorescence reporter is given by:

$$-\vec{\nabla} \cdot (D(\overrightarrow{r}) \cdot \vec{\nabla}(U_{em}(\vec{r})) + \mu_a \cdot U_{em}(\vec{r}) = \eta c_{fl}(\overrightarrow{r}) U_{ex}(\overrightarrow{r}) \tag{1.4}$$

The inverse problem is solved numerically (e.g using the Algebraic Reconstruction Technique or Conjugate Gradient method) [21, 25]. Using the normalized Born approximation has shown to increase robustness of FMT reconstruction and is calculated by taking the ratio of the fluorescent and excitation field and eliminates several parameters related to the detection instruments [41]. For more detailed information about diffusive light propagation the reader is referred to [3, 40, 42, 43].

FMT is usually used in the near-infrared domain 650nm < λ<900nm where the extinction coefficient inside the biological tissue (main absorbers: hemoglobin, oxygenated hemoglobin and water) is minimum and therefore depth penetration of FMT is deeper [3].

In summary, FMT poses an excellent method for molecular imaging in small animals using non-ionizing radiation. It potentially enables many new approaches in diagnostics, drug development and basic biomedical research.

1.3 Magnetic Resonance Imaging

MRI has been described extensively in several textbooks, e.g. [3, 44-46]. In the following, we will discuss the basics required in the context of this thesis.

If a magnetic nucleus with nuclear spin I=1/2 is placed in a static magnetic field B_0 it will orient either parallel or antiparallel to the field. The energy of the two states differs, i.e. giving rise to the so-called Zeeman splitting. The energy difference between the two states is given by

$$\Delta E = \hbar \cdot \gamma \cdot B_0 \tag{1.5}$$

with $\hbar$ being the Planck constant ($\hbar = h/2\pi$) and γ the gyromagnetic ratio of the nucleus. At thermal equilibrium at body temperature a slight excess of the proton spins occupy the lower energy state (approximately 30ppm at B_0=9.4T). Transitions between these two states are induced by irradiation at the resonance frequency

$$\omega_{Larmor} = \gamma B_0 \ , \tag{1.6}$$

the so-called Larmor frequency. As a result the population difference between the two states diminishes. Moreover, the proton magnetic moments align along the time-dependent radiofrequency field giving rise to a non-vanishing transverse magnetization component that rotates around the static magnetic field at the precession frequency. This time-dependent transverse magnetization component induces a voltage in a detector coil, the nuclear magnetic resonance signal. When the electromagnetic irradiation is terminated, phase coherence is lost (the free induction decay, FID) and the proton spins return back to the thermal equilibrium distribution between the two states. The time constant describing the loss of phase coherence is called T_2*, while the time constant for the return to the equilibrium state is called longitudinal relaxation time T_1. The loss of phase coherence is due to two processes, a deterministic process caused by static magnetic field inhomogeneity and a second stochastic contribution due to fluctuation in local magnetic fields due to intra- and intermolecular dynamics. The second term is called transverse relaxation time T_2. Relaxation times are tissue specific and hence a source of contrast in MRI.

The multiparametric signal dependence is exploited to optimize contrast in MRI. Spin-echo sequences such as rapid acquisition with relaxation enhancement (RARE) [47] emphasize T_2 effects (T_2-weighted MRI), while gradient echo images experiments such as fast low-angle shot imaging (FLASH) [48] emphasize T_1 effects (for short echo and repetition delays) or T_2* (for long echo and medium to long repetition delay). Similar echo planar imaging (EPI) [49] yields T_2* dominated contrast.

The Larmor frequency is given by equation 1.6 and is proportional to the magnetic field. A gradient magnetic field overlaid on a static magnetic field can therefore be applied to make the resonance frequency dependent on its position:

$$\omega(\overrightarrow{x}) = \gamma \cdot (B_0 + G_x \cdot x) \tag{1.7}$$

With G_x a gradient magnetic field (e.g from a gradient coil) along the x-axis. Using a radio frequency pulse of frequency bandwidth

$$\Delta\omega < \omega_{max} - \omega_{min} \tag{1.8}$$

for excitation only a slice will be resonating, which can be used for spatial encoding.

One type of coils used for excitation of the protons is the surface coil. When using surface coil it's important to keep in mind that sensitivity for signal picking up decreases with distance from the coil depending on its geometry and therefore the sample should be close to the coil [50].

Thus, MRI enables 3-dimensional imaging of biological soft-tissue at relatively high spatial resolution and therefore poses a valuable tool for obtaining structural and functional information in both preclinical research and clinics.

1.4 Hybrid Systems

The first hybrid system developed was a SPECT-XCT system proposed in 1989 and realized in 1994 [51, 52]. Today there are combinations of modalities available and research and development of such devices is a hot topic [53]. The optimal 'all-in-one' imaging modality does not exist. Some are very sensitive e.g PET and optical imaging technologies but suffer from poor resolution. As they image the distribution of labeled compounds they do not provide anatomical information. Other modalities such as MRI and XCT yield high spatial resolution images and intrinsic tissue contrast, thus providing anatomical information, however are of limited value for providing molecular information. Therefore, the idea of combining imaging modalities providing complementary information appears logical. Moreover, prior information derived from one technique may be used in the image reconstruction process for the other. For example in PET-XCT, XCT images can be used for attenuation correction when reconstructing PET data [54]. The clinically most established hybrid systems today are PET-XCT and PET-MRI [3]. Recently a study involving a trimodality system PET-XCT-MRI was published [55]. A disadvantage of PET-XCT is its high radiation exposure for the patient, and ways to reduce it are an important research topic [56]. PET-MRI is used mainly for molecular imaging applications, in particular in neuroimaging and diagnosis of neurological disorders [57]. Incorporating a PET system into an MRI required some compromises and therefore the overall performance of PET is reduced as compared to stand-alone PET systems [58]. In general, molecular imaging with PET requires an on-site cyclotron and radiochemistry for generation of the probes, due to the short half-life of the isotopes used in PET. An interesting alternative for preclinical imaging is using the stable fluorescent probes in combination with a structural imaging modality. A FMT-XCT system has been reported using laser source and a CCD camera for fluorescence detection mounted on the XCT gantry. Using XCT derived prior information for the reconstruction of FMT data significantly improved the results [31, 59]. An interesting alternative is FMT-MRI. MRI comes with high-value soft-tissue contrast, can also add functional/physiological information, and thus constitutes a versatile imaging modality. A number of multimodal probes combining an MRI contrast agent with a fluorescent reporter have been developed and used in vivo experiments[60, 61].

Multimodal imaging comes in two flavors: one strategy is sequentially imaging with the two modalities, using a sample holder that is compatible with both systems to ensure coregistration of images. Yet

simultaneous imaging would be favorable, as data are intrinsically co-registered. Moreover, when studying dynamic process, simultaneous images are unavoidable.

A true hybrid FMT-MRI may be realized by guiding light in and out of the MRI magnet using optic fibers and several such systems have been reported [62, 63]. This approach has however clear limitations. Glass-fibers have limited bending radii and thus need quite some radial space, and thus large magnetic bore diameters. In fact, these systems typically use clinical MRI magnets, which due to the lower field strength are not optimal for mouse imaging. Moreover, the number of source-detection pairs is limited and there is no flexibility regarding the FMT excitation scheme, which is suboptimal for FMT reconstruction. As fibers should be in close contact with the sample for optimal coupling, the experiment becomes rather cumbersome and inflexible [62-65]. Alternatively the laser light could be introduced into the magnet as a free-beam in a non-contact arrangement. Detection could occur either using a camera coupled to the sample using an optical fiber bundle, which suffers from similar spatial restriction as systems using fibers for both excitation and detection. Instead the image sensor might be positioned directly at the sample location, which however requires the camera to be compatible with the harsh condition at the center of the MRI magnet. This strategy was pursued in a hybrid system using a single-photon avalanche detector (SPAD-detector), which was inspired by the SPAD used in the PET-MRI modality[42, 66], and which will be described in more detail in Chapter 2 of the thesis. This last system constituted the starting point for the current PhD project.

1.5 Aim of the Thesis

Proof of principle of simultaneous FMT and MRI measurements has been demonstrated using a previous hybrid FMT-MRI system (FMT-MRI 1.0). This system was characterized by an image sensor inside the MRI bore and an illumination module located outside the MRI with the light transmitted into the magnet in a free laser beam configuration [42, 66]. The design suffered from several shortcomings in performance such as low sensitivity, small field-of-view, and the necessity to carefully calibrate the optical system prior to every experiment, a cumbersome process even for experts.

The goal of this thesis was to overcome these deficiencies and develop a compact system that is easy to operate even for non-experts. The prerequisite for the new FMT-MRI design were:

- to evaluate and incorporate a novel image sensor with improved sensitivity and increased resolution (pixel resolution and field-of-view)
- to further enhance the sensitivity by cooling the image sensor
- to mount all optical components required for the FMT experiment, i.e. collimators, scanners and wavelength filter, and detector in a fixed geometrical arrangement to avoid calibration steps prior to each experiment.
- to enhance the flexibility of the system by incorporating both reflection and transmission mode operation

- to enhance the flexibility of the system by enabling operation at multiple colors via wavelength specific bandpass filters
- to minimize crosstalk between modalities by adequate shielding measures
- to design a light-tight enclosing to avoid stray light interference
- to facilitate animal handling such that their preparation does not interfere with the optical and MRI setup

The FMT probe should be designed as compact cylindrical probe with a minimal number of connectors for optical fibers, rf cable, control and detector cables for the image sensor and tubings for cooling water and anesthesia gases. Challenges in designing the FMT insert for the hybrid system were space constraints determined by the inner diameter of magnet bore and gradient system and exposure of all components to strong static and dynamic magnetic fields and radiofrequency fields, i.e. sources of potential electromagnetic interference.

1.6 Outline

Chapter 1 of this thesis describes some basics of FMT and MRI, and then discusses multimodal imaging systems that are described in the literature.

Chapter 2 discusses the development of hybrid FMT-MRI systems at AIC at UZH/ETH with a focus on the newest, the FMT-MRI 3.0. Considerations during the design of the systems are explained and the individual components are described in detail.

Chapter 3 deals with the characterization of the hybrid FMT-MRI 3.0 system and includes first experiments with a tissue-mimicking phantom and a mouse to demonstrate feasibility of hybrid FMT-MRI readouts in a biological system.

Chapter 4 demonstrates the potential of true hybrid imaging using an earlier system version (FMT-MRI 2.0). Simultaneous dynamic imaging experiments were carried out to characterize structural and functional properties of tumor neovasculature in mice carrying subcutaneous tumors.

Finally, Chapter 5 critically assesses the performance of the FMT-MRI 3.0 system, highlights aspects that should be further improved and concludes with an outlook describing potential future developments.

1. Goodman, P.C., *The new light: discovery and introduction of the X-ray.* AJR. American journal of roentgenology, 1995. **165**(5): p. 1041-1045.
2. Spiegel, P.K., *The first clinical X-ray made in America--100 years.* AJR. American journal of roentgenology, 1995. **164**(1): p. 241-243.
3. Rudin, M., *Molecular imaging: basic principles and applications in biomedical research*. 2013: World Scientific.
4. Weissleder, R. and M.J. Pittet, *Imaging in the era of molecular oncology.* Nature, 2008. **452**(7187): p. 580-589.
5. Jacobs, A.H., H. Li, A. Winkeler, R. Hilker, C. Knoess, A. Rueger, N. Galldiks, B. Schaller, J. Sobesky, and L. Kracht, *PET-based molecular imaging in neuroscience.* European journal of nuclear medicine and molecular imaging, 2003. **30**(7): p. 1051-1065.
6. Rudin, M. and R. Weissleder, *Molecular imaging in drug discovery and development.* Nature reviews Drug discovery, 2003. **2**(2): p. 123-131.
7. Hanahan, D. and R.A. Weinberg, *The hallmarks of cancer.* cell, 2000. **100**(1): p. 57-70.
8. Hanahan, D. and R.A. Weinberg, *Hallmarks of cancer: the next generation.* cell, 2011. **144**(5): p. 646-674.
9. Weissleder, R., M.C. Schwaiger, S.S. Gambhir, and H. Hricak, *Imaging approaches to optimize molecular therapies.* Science translational medicine, 2016. **8**(355): p. 355ps16-355ps16.
10. Weissleder, R., *A clearer vision for in vivo imaging.* Nature biotechnology, 2001. **19**(4): p. 316-316.
11. Green, M., J. Seidel, J.J. Vaquero, E. Jagoda, I. Lee, and W. Eckelman, *High resolution PET, SPECT and projection imaging in small animals.* Computerized medical imaging and graphics, 2001. **25**(2): p. 79-86.
12. Ntziachristos, V., J. Ripoll, L.V. Wang, and R. Weissleder, *Looking and listening to light: the evolution of whole-body photonic imaging.* Nature biotechnology, 2005. **23**(3): p. 313-320.
13. Ntziachristos, V., *Going deeper than microscopy: the optical imaging frontier in biology.* Nature methods, 2010. **7**(8): p. 603-614.
14. Jobsis, F.F., *Noninvasive, infrared monitoring of cerebral and myocardial oxygen sufficiency and circulatory parameters.* Science, 1977. **198**(4323): p. 1264-1267.
15. Arridge, S.R., *Optical tomography in medical imaging.* Inverse problems, 1999. **15**(2): p. R41.
16. Arridge, S.R. and W.R. Lionheart, *Nonuniqueness in diffusion-based optical tomography.* Optics letters, 1998. **23**(11): p. 882-884.
17. Hebden, J.C., A. Gibson, R.M. Yusof, N. Everdell, E.M. Hillman, D.T. Delpy, S.R. Arridge, T. Austin, J.H. Meek, and J.S. Wyatt, *Three-dimensional optical tomography of the premature infant brain.* Physics in medicine and biology, 2002. **47**(23): p. 4155.
18. Ntziachristos, V., A. Yodh, M. Schnall, and B. Chance, *Concurrent MRI and diffuse optical tomography of breast after indocyanine green enhancement.* Proceedings of the National Academy of Sciences, 2000. **97**(6): p. 2767-2772.
19. Patterson, M.S., B. Chance, and B.C. Wilson, *Time resolved reflectance and transmittance for the noninvasive measurement of tissue optical properties.* Applied optics, 1989. **28**(12): p. 2331-2336.
20. Ripoll, J., *Light diffusion in turbid media with biomedical application.* These de doctorat, Faculty of the Universidad Autonoma de Madrid, 2000.
21. Ntziachristos, V., C.-H. Tung, C. Bremer, and R. Weissleder, *Fluorescence molecular tomography resolves protease activity in vivo.* Nature medicine, 2002. **8**(7): p. 757-761.
22. Haskell, R.C., L.O. Svaasand, T.-T. Tsay, T.-C. Feng, B.J. Tromberg, and M.S. McAdams, *Boundary conditions for the diffusion equation in radiative transfer.* JOSA A, 1994. **11**(10): p. 2727-2741.
23. Ishimaru, A., *Diffusion of light in turbid material.* Applied optics, 1989. **28**(12): p. 2210-2215.
24. Daunizeau, J., J. Mattout, D. Clonda, B. Goulard, H. Benali, and J.-M. Lina, *Bayesian spatio-temporal approach for EEG source reconstruction: conciliating ECD and distributed models.* IEEE Transactions on Biomedical Engineering, 2006. **53**(3): p. 503-516.

25. Shi, J., B. Zhang, F. Liu, J. Luo, and J. Bai, *Efficient L1 regularization-based reconstruction for fluorescent molecular tomography using restarted nonlinear conjugate gradient.* Optics letters, 2013. **38**(18): p. 3696-3699.
26. Graves, E.E., J. Ripoll, R. Weissleder, and V. Ntziachristos, *A submillimeter resolution fluorescence molecular imaging system for small animal imaging.* Medical physics, 2003. **30**(5): p. 901-911.
27. Boellaard, R., M.J. O'Doherty, W.A. Weber, F.M. Mottaghy, M.N. Lonsdale, S.G. Stroobants, W.J. Oyen, J. Kotzerke, O.S. Hoekstra, and J. Pruim, *FDG PET and PET/CT: EANM procedure guidelines for tumour PET imaging: version 1.0.* European journal of nuclear medicine and molecular imaging, 2010. **37**(1): p. 181.
28. Beyer, T., D.W. Townsend, T. Brun, and P.E. Kinahan, *A combined PET/CT scanner for clinical oncology.* The Journal of nuclear medicine, 2000. **41**(8): p. 1369.
29. Ale, A., V. Ermolayev, E. Herzog, C. Cohrs, M.H. De Angelis, and V. Ntziachristos, *FMT-XCT: in vivo animal studies with hybrid fluorescence molecular tomography-X-ray computed tomography.* Nature methods, 2012. **9**(6): p. 615-620.
30. Nahrendorf, M., P. Waterman, G. Thurber, K. Groves, M. Rajopadhye, P. Panizzi, B. Marinelli, E. Aikawa, M.J. Pittet, and F.K. Swirski, *Hybrid in vivo FMT-CT imaging of protease activity in atherosclerosis with customized nanosensors.* Arteriosclerosis, thrombosis, and vascular biology, 2009. **29**(10): p. 1444-1451.
31. Hyde, D., R. de Kleine, S.A. MacLaurin, E. Miller, D.H. Brooks, T. Krucker, and V. Ntziachristos, *Hybrid FMT–CT imaging of amyloid-β plaques in a murine Alzheimer's disease model.* Neuroimage, 2009. **44**(4): p. 1304-1311.
32. Hyde, D., E. Miller, D. Brooks, and V. Ntziachristos. *New techniques for data fusion in multimodal FMT-CT imaging*. in *Biomedical Imaging: From Nano to Macro, 2008. ISBI 2008. 5th IEEE International Symposium on*. 2008. IEEE.
33. Schenck, J.F., *The role of magnetic susceptibility in magnetic resonance imaging: MRI magnetic compatibility of the first and second kinds.* Medical physics, 1996. **23**(6): p. 815-850.
34. Oborn, B.M., S. Dowdell, P.E. Metcalfe, S. Crozier, R. Mohan, and P.J. Keall, *Future of Medical Physics: Real-time MRI guided Proton Therapy.* Medical Physics, 2017.
35. Zhang, S., M. Uecker, D. Voit, K.-D. Merboldt, and J. Frahm, *Real-time cardiovascular magnetic resonance at high temporal resolution: radial FLASH with nonlinear inverse reconstruction.* Journal of Cardiovascular Magnetic Resonance, 2010. **12**(1): p. 39.
36. Chinzei, K., N. Hata, F.A. Jolesz, and R. Kikinis. *MR compatible surgical assist robot: System integration and preliminary feasibility study*. in *MICCAI*. 2000. Springer.
37. Winterwerber, K., *Entwicklung einer im Magnetresonanztomografen einsatzfähigen chirurgischen Bohrmaschine.* 2011.
38. Gassert, R., *MR-compatible robotics to investigate human motor control.* Ecole Polytechnique Federale de Lausanne, 2006.
39. Ripoll, J., *Derivation of the scalar radiative transfer equation from energy conservation of Maxwell's equations in the far field.* JOSA A, 2011. **28**(8): p. 1765-1775.
40. Wang, L.V. and H.-i. Wu, *Biomedical optics: principles and imaging*. 2012: John Wiley & Sons.
41. Ntziachristos, V. and R. Weissleder, *Experimental three-dimensional fluorescence reconstruction of diffuse media by use of a normalized Born approximation.* Optics letters, 2001. **26**(12): p. 893-895.
42. Stuker, F., C. Baltes, K. Dikaiou, D. Vats, L. Carrara, E. Charbon, J. Ripoll, and M. Rudin, *Hybrid small animal imaging system combining magnetic resonance imaging with fluorescence tomography using single photon avalanche diode detectors.* IEEE transactions on medical imaging, 2011. **30**(6): p. 1265-1273.
43. Lorenzo, J.R., *Principles of diffuse light propagation: light propagation in tissues with applications in biology and medicine*. 2012: World Scientific.
44. Hornak, J.P., *The basics of MRI*. 1996, Rochester Institute of Technology.

45. Haacke, E.M., R.W. Brown, M.R. Thompson, and R. Venkatesan, *Magnetic resonance imaging: physical principles and sequence design*. Vol. 82. 1999: Wiley-Liss New York:.
46. Levitt, M.H., *Spin dynamics: basics of nuclear magnetic resonance*. 2001: John Wiley & Sons.
47. Hennig, J., A. Nauerth, and H. Friedburg, *RARE imaging: a fast imaging method for clinical MR.* Magnetic resonance in medicine, 1986. **3**(6): p. 823-833.
48. Frahm, J., A. Haase, and D. Matthaei, *Rapid NMR imaging of dynamic processes using the FLASII technique.* Magnetic resonance in medicine, 1986. **3**(2): p. 321-327.
49. Mansfield, P., D. Guilfoyle, R. Ordidge, and R. Coupland, *Measurement of T1 by echo-planar imaging and the construction of computer-generated images.* Physics in medicine and biology, 1986. **31**(2): p. 113.
50. Lawry, T., M. Weiner, and G. Matson, *Computer modeling of surface coil sensitivity.* Magnetic resonance in medicine, 1990. **16**(2): p. 294-302.
51. Kaplan, I. and L. Swayne, *Composite SPECT-CT images: technique and potential applications in chest and abdominal imaging.* American Journal of Roentgenology, 1989. **152**(4): p. 865-866.
52. Blankespoor, S., B. Hasegawa, J. Brown, J. Heanue, R. Gould, C. Cann, and M. Dae. *Development of an emission-transmission CT system combining x-ray CT and SPECT*. in *Nuclear Science Symposium and Medical Imaging Conference, 1994., 1994 IEEE Conference Record*. 1995. IEEE.
53. Padmanabhan, P., A.M. Nedumaran, S. Mishra, G. Pandarinathan, G. Archunan, and B. Gulyás, *The Advents of Hybrid Imaging Modalities: A New Era in Neuroimaging Applications.* Advanced Biosystems, 2017.
54. Kinahan, P., D. Townsend, T. Beyer, and D. Sashin, *Attenuation correction for a combined 3D PET/CT scanner.* Medical physics, 1998. **25**(10): p. 2046-2053.
55. Veit-Haibach, P., F.P. Kuhn, F. Wiesinger, G. Delso, and G. von Schulthess, *PET–MR imaging using a tri-modality PET/CT–MR system with a dedicated shuttle in clinical routine.* Magnetic Resonance Materials in Physics, Biology and Medicine, 2013: p. 1-11.
56. Tonkopi, E., A.A. Ross, and A. MacDonald, *JOURNAL CLUB: CT dose optimization for whole-body PET/CT examinations.* American Journal of Roentgenology, 2013. **201**(2): p. 257-263.
57. Heiss, W.-D., *The potential of PET/MR for brain imaging.* European journal of nuclear medicine and molecular imaging, 2009. **36**: p. 105-112.
58. Delso, G., E. ter Voert, F. de Galiza Barbosa, and P. Veit-Haibach. *Pitfalls and limitations in simultaneous PET/MRI*. in *Seminars in nuclear medicine*. 2015. Elsevier.
59. Hyde, D., R. Schulz, D. Brooks, E. Miller, and V. Ntziachristos, *Performance dependence of hybrid x-ray computed tomography/fluorescence molecular tomography on the optical forward problem.* JOSA A, 2009. **26**(4): p. 919-923.
60. Niedre, M. and V. Ntziachristos, *Elucidating structure and function in vivo with hybrid fluorescence and magnetic resonance imaging.* Proceedings of the IEEE, 2008. **96**(3): p. 382-396.
61. Zhang, Y., B. Zhang, F. Liu, J. Luo, and J. Bai, *In vivo tomographic imaging with fluorescence and MRI using tumor-targeted dual-labeled nanoparticles.* International journal of nanomedicine, 2014. **9**: p. 33.
62. Li, B., F. Maafi, R. Berti, P. Pouliot, E. Rhéaume, J.-C. Tardif, and F. Lesage, *Hybrid FMT-MRI applied to in vivo atherosclerosis imaging.* Biomedical optics express, 2014. **5**(5): p. 1664-1676.
63. Davis, S.C., K.S. Samkoe, J.A. O'Hara, S.L. Gibbs-Strauss, H.L. Payne, P.J. Hoopes, K.D. Paulsen, and B.W. Pogue, *MRI-coupled fluorescence tomography quantifies EGFR activity in brain tumors.* Academic radiology, 2010. **17**(3): p. 271-276.
64. Davis, S.C., B.W. Pogue, R. Springett, C. Leussler, P. Mazurkewitz, S.B. Tuttle, S.L. Gibbs-Strauss, S.S. Jiang, H. Dehghani, and K.D. Paulsen, *Magnetic resonance–coupled fluorescence tomography scanner for molecular imaging of tissue.* Review of Scientific Instruments, 2008. **79**(6): p. 064302.

65. Davis, S.C., K.S. Samkoe, K.M. Tichauer, K.J. Sexton, J.R. Gunn, S.J. Deharvengt, T. Hasan, and B.W. Pogue, *Dynamic dual-tracer MRI-guided fluorescence tomography to quantify receptor density in vivo.* Proceedings of the National Academy of Sciences, 2013. **110**(22): p. 9025-9030.
66. Stuker, F., *Hybrid imaging: combining fluorescence molecular tomography with magnetic resonance imaging.* 2011.

Chapter 2

System Design

In this chapter the design and construction of a hybrid Fluorescent Molecular Tomography (FMT)-Magnetic Resonance Imaging (MRI) system for preclinical imaging is described.

The objective of this PhD thesis consists in the development of a compact FMT system that can be used as an insert for a small animal MRI scanner with a clear bore size of ≥120mm (inner diameter if the gradient system is missing) for imaging with mice. In the current design, we used a Bruker BioSpec 94/30 system (Bruker BioSpin GmbH, Ettlingen Germany). The FMT system consists of an illumination module, a laser scanner module, an imaging module and an operation software (Fig. 2.1). The illumination module comprises the light source, typically a fiber-coupled diode laser that generates the laser beam for excitation of the fluorescent dye. The laser scanner module comes typically with a mirror that deflects the laser beam and an actuation mechanism that allows for scanning of the illumination points across the sample. The imaging module consisting of an image sensor (detector array) records an image for each illumination point both at the excitation and emission wavelength

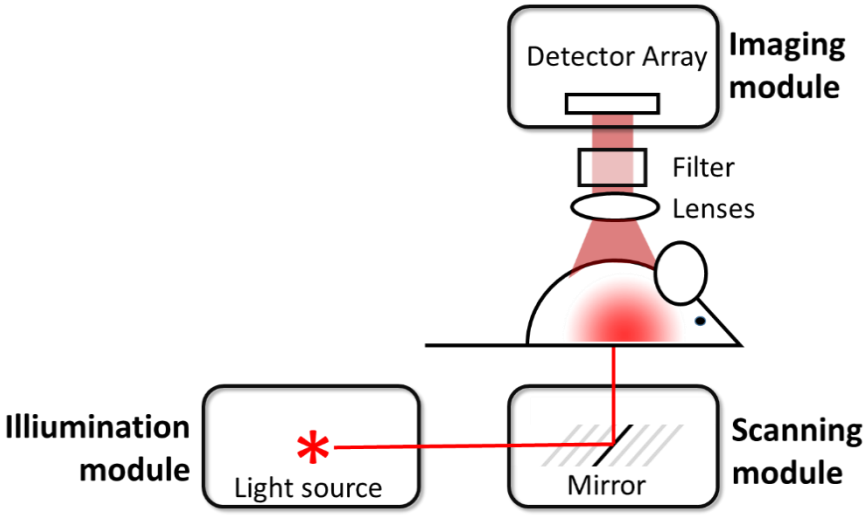

Fig. 2.1 Basic building blocks of FMT imaging system. It shows the illumination module, the scanning module and the imaging module. The illumination module produces the light source for the FMT system. The scanning module scans the FMT source pattern. The imaging module detects the signal of both the sources and the fluorescence. A bandpass filter has to be switched correspondingly.

selected. A band-pass filter in front of the sensor is used to enable detection of a specific wavelength domain. An operation software controls the proper interplay of illumination, scanning and detector modules.

In a first part of this chapter, the 1st and 2nd generation hybrid FMT-MRI systems (FMT-MR 1.0 and 2.0) developed in the Animal Imaging Center at ETH Zurich are discussed (Sections 2.1 and 2.2). The 3rd generation hybrid FMT-MRI system (FMT-MRI 3.0), which constitutes the major part of this PhD project, involved a radical change in system design (Section 2.3). Scanning and imaging modules were combined in a fixed frame, which allowed avoiding tedious recalibration before each experimental session. The miniaturization also involved the using of alternative scanning devices.

2.1 Hybrid FMT-MRI 1.0 System

The FMT-MRI 1.0 system was developed in the Animal Imaging Center at ETH Zurich by Stuker et al [2, 5] (Fig. 2.2). The system was developed to demonstrate proof-of-principle of FMT-MRI hybrid imaging. The core element of the imaging module was a single photon avalanche diode (SPAD) detector as image sensor bonded on its printed circuit board (PCB). The use of the avalanche photon detector in hybrid PET/MRI systems was the inspiration for using a SPAD detector for a hybrid FMT-MRI system [2]. The image sensor comprised an array of 32x32 pixels arranged in a square of 0.96mm length. The fill factor was of 3.15% and a maximum photon detection probability of 35%, fill factor not included, was measured [5]. The illumination module comprised a diode laser source, while the scanning module consisted of two galvanometrically driven mirrors (ScanCube, ScanLabs, Puchheim, Germany). Both the illumination and scanning module were placed outside the MRI magnet in a minimal magnetic fringe field to ascertain proper operation. Following the deflection by the mirrors the free laser beam was directed towards the center of the MRI bore, where it hit another mirror mounted on top of the animal support. This mirror deflected the laser beam onto the sample. Proper reorientation of the ScanCube mirrors allowed scanning the desired source pattern on the sample surface. Depending on the choice of the bandpass filter the intensity distribution of the incident (excitation light) or emitted (fluorescence) wave was detected by the SPAD detector.

Feasibility of hybrid imaging was demonstrated in a biological application with nude mice bearing a subcutaneous colon cancer xenograft which was simultaneously imaged with both FMT to map protease activity using the probe (ProSense680, Perkin Elmer, USA) and MRI to provide a structural reference map (Fig. 2.3).

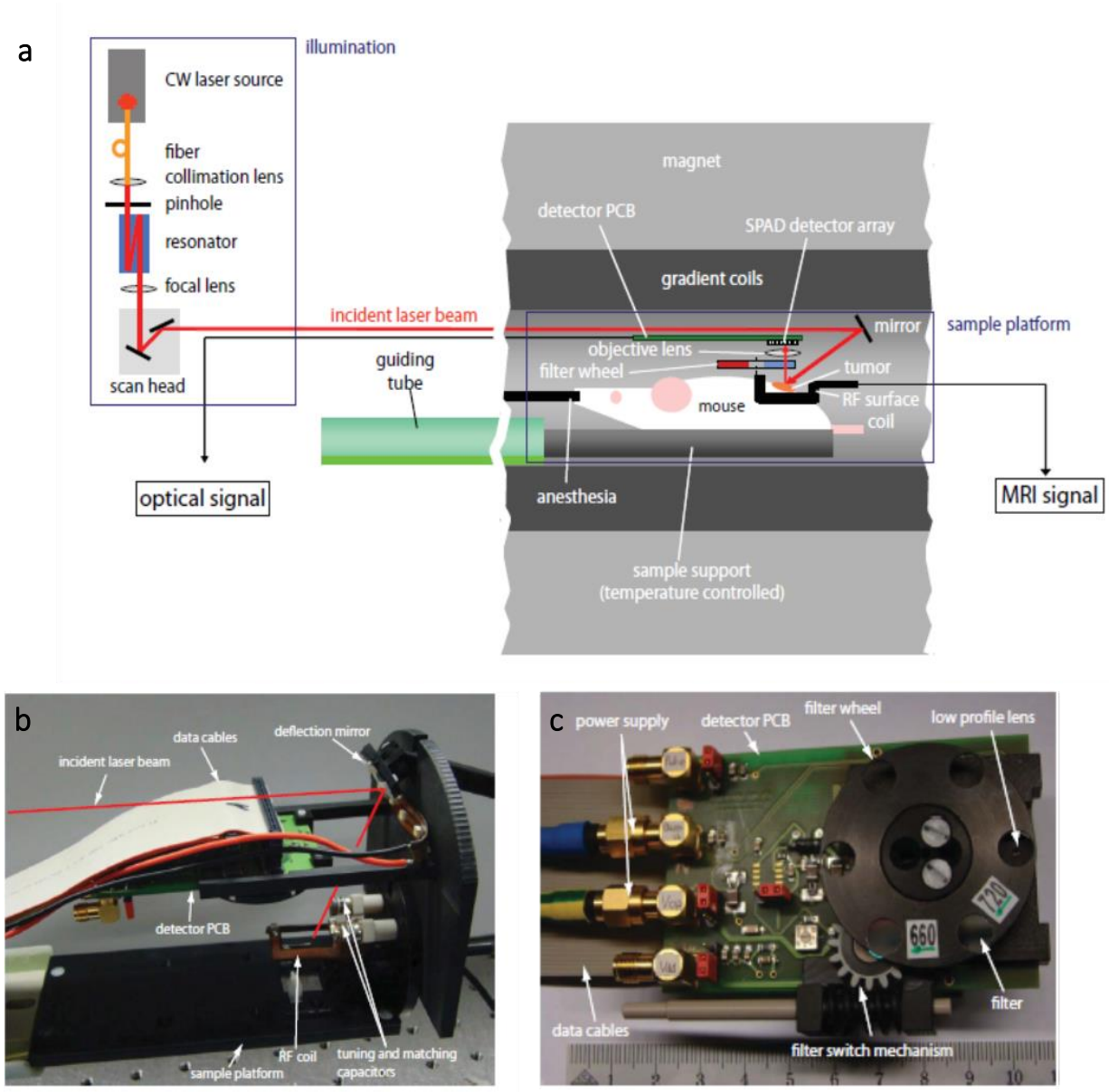

Fig. 2.2 FMT-MRI 1.0 (a) Schematics of the system with the illumination module including laser scanner on the left side and the FMT probe on the right side. The laser is transmitted in a free-beam configuration to the mirror mounted on the FMT probe, which deflects the beam onto the sample. A galvanometrically driven mirror scans the FMT sources. The FMT data is imaged with the detector PCB. (b) FMT-MRI 1.0 with the detector PCB having a SPAD image sensor mounted. A 1.5cm large deflection mirror is located on top of the camera for deflecting the laser beam onto the sample. (c) Close-up view of camera PCB frontside. The filter module consists of a filter wheel with filter mounted at 660nm and 720nm [2].

While the FMT-MRI 1.0 achieved proof-of-principle, its limitations became quickly evident. Precise positioning of the animal support, containing the top mirror for sample illumination and the imaging module, inside the MRI scanner was necessary, since the laser beam had to hit and scan the top mirror

with a side length of around 1.5cm from a distance of 2m after exiting the laser scanner. Tedious geometric alignment and calibration was required to properly position the source pattern on the tumor of the mouse. Any movement of the animal support be it due to filter changing or control of animal physiology, required recalibration. In particular for non-rigid objects such as mice it was difficult to exactly reproduce the original source pattern. However, source patterns during the recording of the excitation and emission scheme should be exactly superimposed to warrant correct FMT data.

Apart from these operational issues, the system suffered from additional shortcomings. 1) The sensitivity was rather low as compared to a stand-alone reference system based on a commercial high-performance cooled CCD camera. In a study using a tissue mimicking phantom comprising a capillary containing a fluorescence dye buried at 1mm depth of the phantom yielded a signal-to-noise ratio (SNR) of 3.7$\pm$0.4 [5]. At a signal-to-noise ratio below 2 small structures are difficult to detect and according to the Rose criterion an SNR of at least 5 is required to be able to distinguish two features on an image at 100% certainity [6-8], thus this indicates insufficient sensitivity. High sensitivity is crucial as signals emanating from the molecular processes in molecular imaging are intrinsically weak after passing through absorbing and scattering biological tissue. 2) This hybrid FMT-MRI 1.0 system had only FMT in reflection geometry implemented. This yields somewhat higher intensity but intrinsically strong surface weighting of the signals and interference by tissue autofluorescence at the surface. For imaging deeper lying structures it would be beneficial to work with transmission mode [5]. 3) The FMT-MRI-1.0 system based on the SPAD array had a field-of-view of 8mm x 8mm, too small for many biological applications. It would be preferable to substantially increase the field-of-view as sampling of only a small surface area critically reduces the accuracy of reconstruction [5].

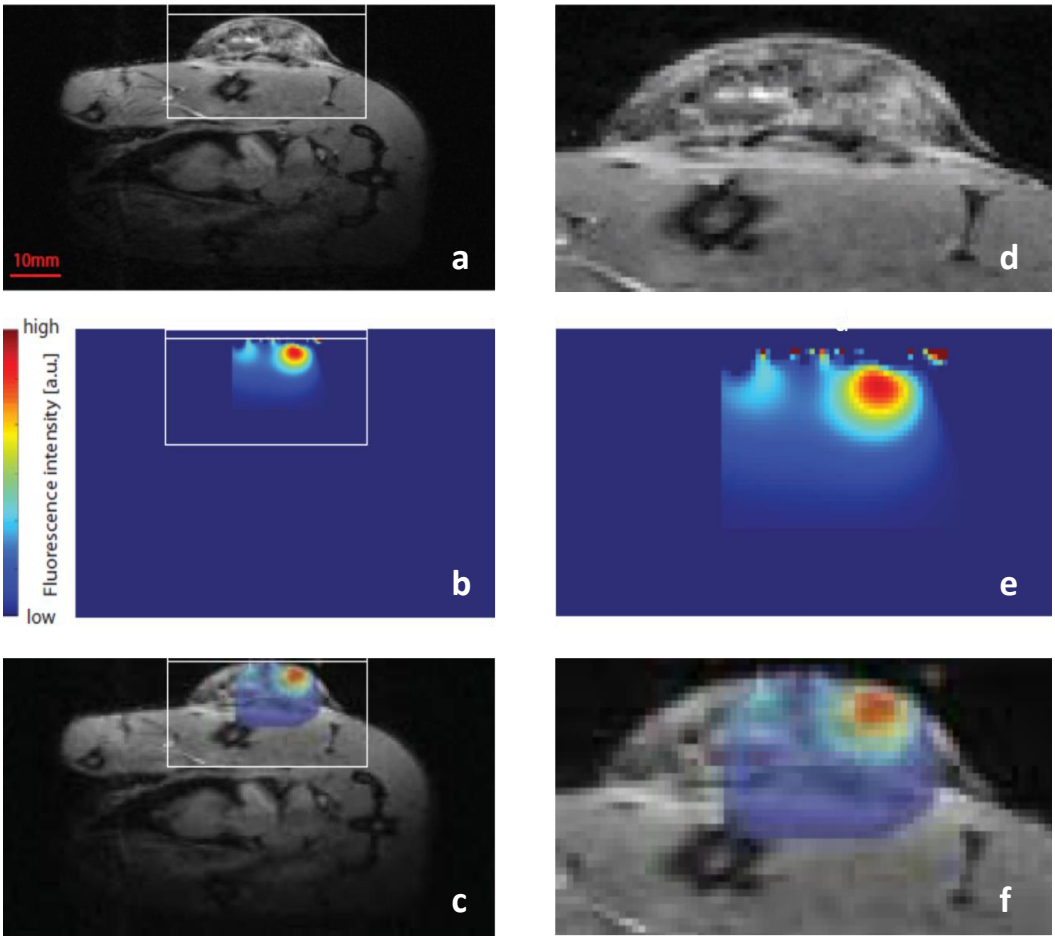

Fig. 2.3 Simultaneous imaging with the hybrid FMT-MRI 1.0 system of a subcutaneous colon cancer xenograft on the left flank of a nude mice. a) MR image of the mouse at the left flank containing the tumor b) Fluorescence Molecular Tomography recorded simultaneously at the same position c) Overlay of the two images d)-f) Zoom-in of a)-c) at the tumor site [5].

2.2 Hybrid FMT-MRI 2.0 System

In view of these deficiencies a hybrid FMT-MRI 2.0 system was designed (Fig. 2.4). While the general layout was conserved, changes made consisted in the replacement of the SPAD detector by a CMOS detector (CSEM, Neuchâtel, Switzerland), the installation of a rail system as guidance for the FMT probe and a “side-scanning strategy” that allowed mounting the camera at a larger distance from the sample. Unfortunately, the rail system turned out to be impractical again, i.e. the issue regarding calibration before each measurement series was not resolved. This was due to insufficient stability of the rail system (flexibility of rail bars, gaps between rails and wheels). While the CMOS camera did not contain strongly magnetic parts, a requirement for placing it into the 9.4T-field of the small animal MRI scanner, it caused dramatic signal degradation on the MR image when running inside the MRI scanner

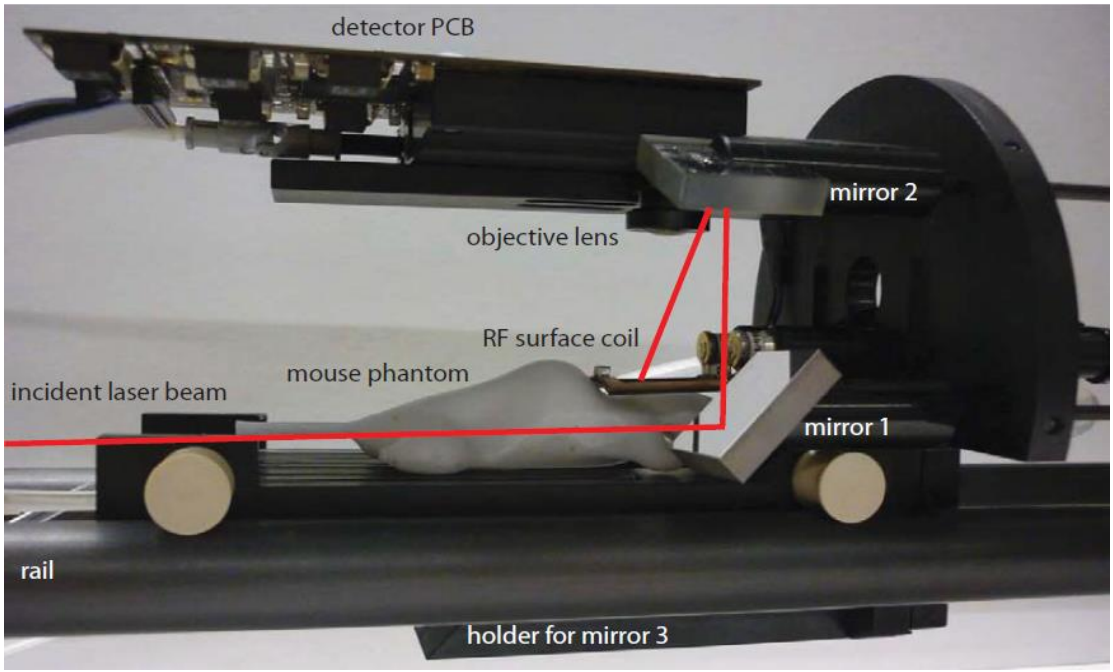

Fig. 2.4 FMT probe of hybrid FMT-MRI 2.0. Four wheels support the FMT probe on the rail bars. A CMOS image sensor is bonded onto the detector PCB. The laser excitation in the reflection geometry is done in the side-scanning configuration allowing to mount the detector at a larger distance from the sample [2].

(Fig. 2.5). Also, the side-scanning strategy turned out to be difficult for proper adjustment of the laser beam to the sample surface and care had to be taken to avoid any interference of the beam with components within the FMT probe.

The task in this PhD thesis was to overcome the previously described deficiencies and to develop a robust and sensitive hybrid FMT-MRI system. Several steps were taken to improve the system: i) The CMOS camera was shielded to avoid cross-talk with the MRI. ii) The image sensor was cooled with a thermoelectric cooler and placed inside a thermally insulating box to increase the sensitivity. iii) The FMT probe was placed on a new linear guiding system.

i) Camera shielding: When characterizing the camera inside the MRI bore interference issues and reduced sensitivity were observed. Stripes and SNR reduction appeared on the MR image whenever the camera was operated inside the MRI-scanner. In a first step, voltage regulators were removed as suspected source of the noise. The camera was then driven by an external power supply. Secondly, the line artefacts have been found to originate from an 80 MHz-oscillator that provides the clock signal for an FPGA used by the control electronics for the camera. This interference could be eliminated by carefully shielding the camera with copper tape (Conrad, Hirschau, Germany) wrapped around the casing. Shielding increased the SNR on the MR images

by a factor of 32 (Fig. 2.5). Therefore, the shielded hybrid FMT-MRI system allowed for truly simultaneous imaging with MRI and FMT. Shielding the camera also improved the SNR of the camera images even when it was located outside the bore (Fig. 2.6 d).

ii) Sensitivity increase by camera cooling: For a further increase of the sensitivity of the camera, a cooling module was developed. A thermoelectric cooler (TEC) (Deltron, Kirchberg, Switzerland) cooled the image sensor. The heat generated by the image sensor was transferred to the TEC using a copper fork (Fig. 2.6e) surrounding the image sensor for equal cooling from several sides. The hot side of the TEC was also cooled with an aluminium block constantly flushed with water to prevent overheating. A housing made of polymethacrylimid hard foam thermally insulated the camera from surrounding warm air. Pure nitrogen gas (N_2) was blown into the housing to prevent water condensation on the camera which could have possibly produced a short-circuit. This allowed operating the image sensor at temperatures below 0° C. Cooling reduced the noise considerably leading to an SNR increase of 3- to 4-fold (Fig. 2.6a-d).

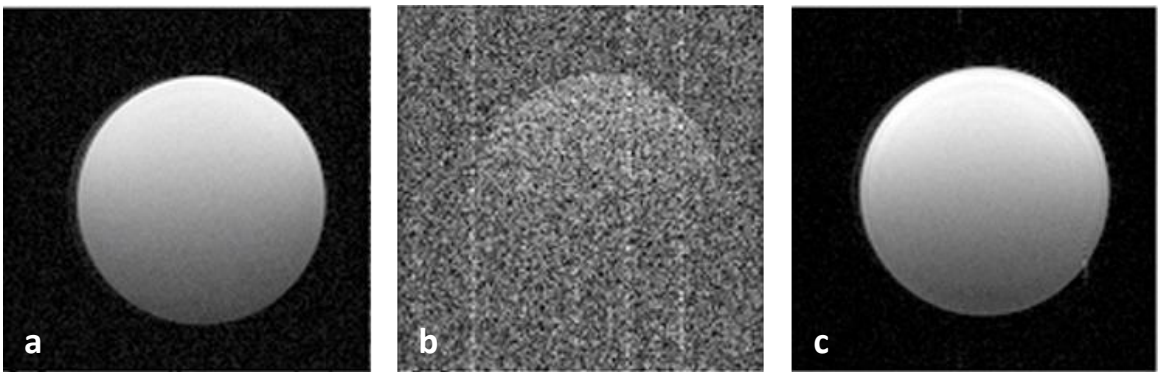

Fig. 2.5 MRI slice of a phantom consisting of a tube filled with water imaged with FLASH, 128x128 pixel resolution, FOV 20mm, TE/TR 4/100. (a) No camera running during recording. SNR=77. (b) CMOS camera placed inside MRI bore and running simultaneously with MRI scan. SNR=3. (c) Same as (b) but camera fully shielded with copper tape. SNR=97.

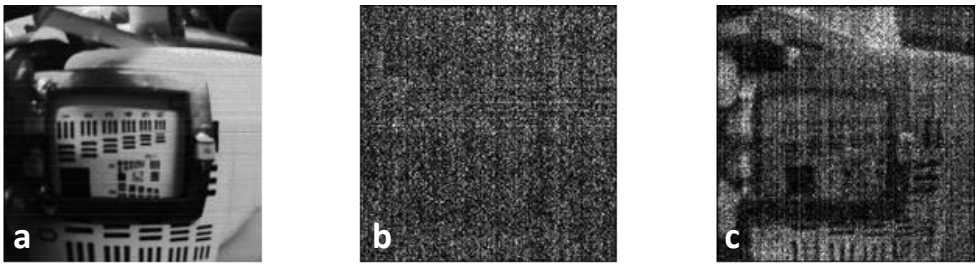

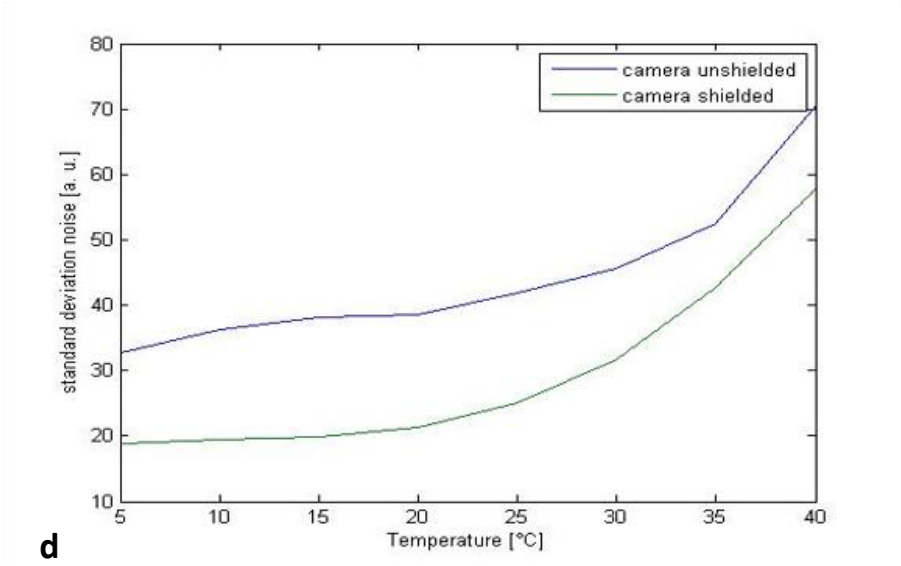

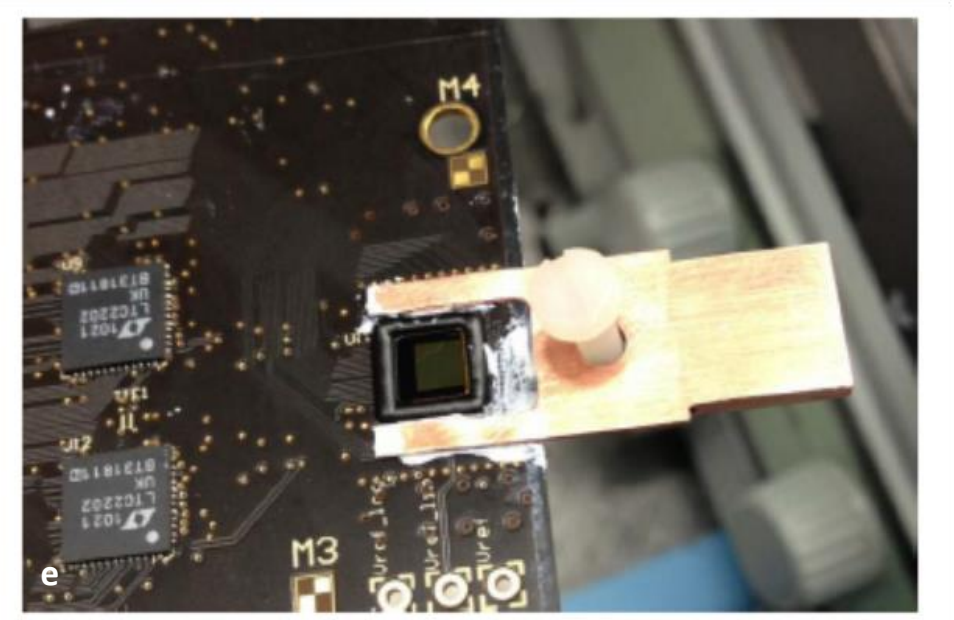

Fig. 2.6 Benefit of cooling to CMOS camera. (a)-(c) Camera scene of USAF chart and surface coil taken with CMOS camera. (a) At daylight conditions. (b) In low-light conditions. (c) Same light condition as in (b), but camera is cooled to 0° C improving the SNR 3-4-fold. (d) Noise level of the camera in function of the temperature. Shielding and cooling of the camera lead to considerable reduction of the noise. The effect of cooling reaches a floor level at lower temperature. (e) Copper fork surrounding the CMOS image sensor for effectively transferring the cooling by the thermoelectric cooler to the sensor.

iii) Improved positioning of the system: The FMT-MRI 2.0 system was placed on top of a linear guide system (Fig. 2.7a), which is explained in more detail in the chapter on the 3rd generation system (Chapter 2.3). This allowed for robust and repeatable insertion of the FMT probe into the MRI bore.

A schematic of the improved FMT-MRI 2.0 system is shown in Fig. 2.7. This updated system showed significantly improved robustness and sensitivity in particular with regard to fluorescence detection and was therefore used for an in vivo study demonstrating the potential of simultaneous FMT-MRI measurements. In particular, it was used to assess blood volume and vascular permeability in subcutaneously implanted tumors in mice using simultaneous injection of fluorescent dyes and MRI contrast agents. This study is a chapter on its own described later in this thesis (Chapter 4).

Despite significant improvements regarding performance and handling, this version of the FMT-MRI 2.0 system still required extensive calibration procedures. In addition, the image sensor of the system broke at the end of the study probably due to mechanical tensions related to temperature gradients.

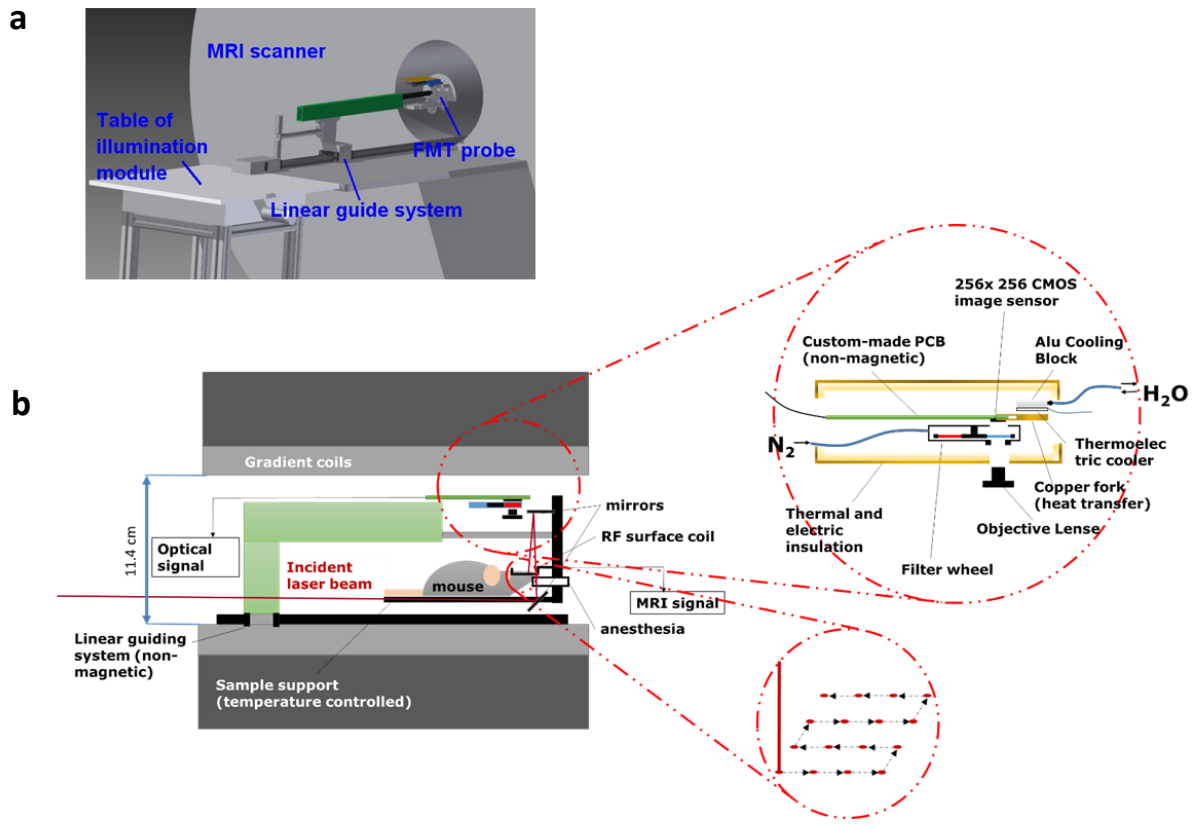

Fig. 2.7 Schematics of the hybrid FMT-MRI system 2.0. The FMT probe is attached to the linear guiding system for precise positioning. The camera is shielded and cooled. The cooling module consists of a thermoelectric cooler that is cooled with an aluminium block.

The camera was a prototype camera meant to be cooled, yet had not undergone sufficient testing by the company to characterize the behavior in response to cooling. Development of this camera type was not further pursued by the company, hence a new camera had to be found. As a consequence, we decided to build a third generation system with a complete redesign based on the experience gained with the FMT-MRI 2.0.

2.3 Hybrid FMT-MRI 3.0 System

With the FMT-MRI 3.0 system a radical redesign of the hybrid system was undertaken based on experience with the FMT-MRI 2.0. The focus of the new design was on simpler and faster handling, higher sensitivity and an increased robustness, power and versatility. The important step was to combine scanning and imaging modules in a fixed frame, which enabled avoiding the tedious recalibration before each experimental session. The miniaturization also involved the using of alternative scanning devices. The FMT probe should be connected to the illumination module via a fiber optic cable. The design concept is illustrated in Fig. 2.8

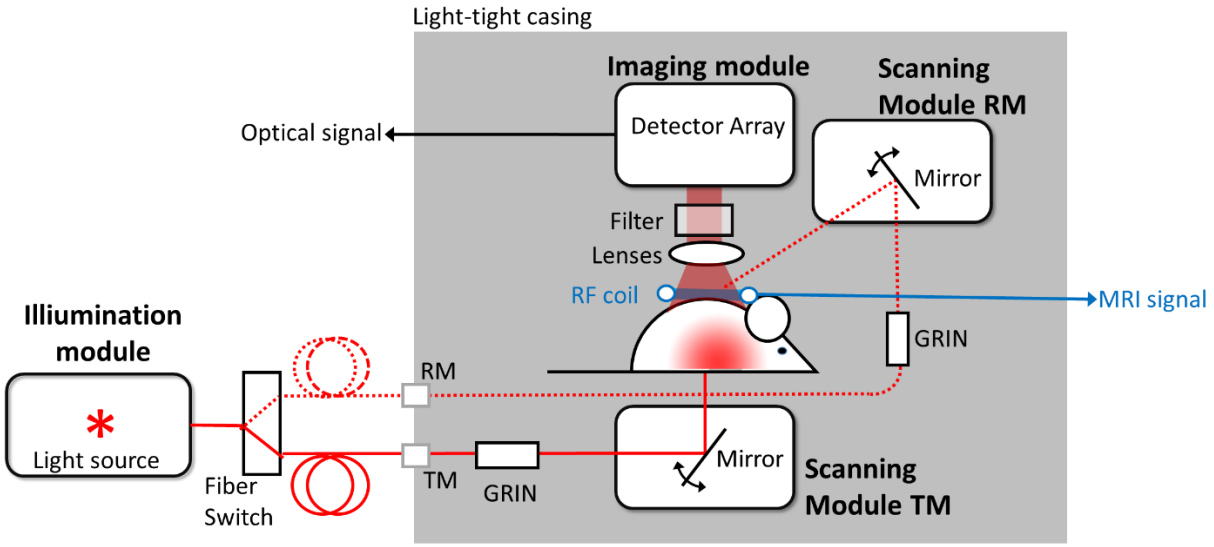

Fig. 2.8 Schematics of the hybrid FMT-MRI 3.0. The system is built inside a light-tight casing with fiber connections for the light source emanating of the illumination module. Inside the casing, GRIN lenses collimate the laser beam exiting the glass fiber and the beam is scanned with scanning module in both reflection mode from the top and transmission mode from the bottom. This excites the fluorescent dye inside the biological samples. The imaging module detects the signal from both the FMT sources and the fluorescent dye. The MR signal is read out with a RF coil.

The system should be sensitive, versatile and easy to operate, i.e. calibration should be intrinsically warranted through position of optical components in a fixed reference frame. As a consequence the scanning devices had to be incorporated into the FMT probe placed within the magnet and should

therefore be small and insensitive against effects imposed by static and dynamic magnetic fields as well as by radiofrequency fields. Microelectromechanical systems (MEMS) have been selected for the purpose. System specifications were defined to increase user-friendliness and robustness, to enhance sensitivity in particular of the optical readout and to improve versatility (reflection and transmission mode operation).

Specifically,

1) factors contributing to robustness and improved user-friendliness are

- Fixed arrangement of optical components, which eliminated tedious calibration procedure prior to experiments. This was achieved by using MRI-compatible MEMS devices enabling laser scanning across the surface of the object.
- Design of a new filter module that allowed improved reliability of filter switching even in the dark. The previous filter wheel-design required multiple rotations of a handle and setting the filter during an experiment was difficult and error-prone, since there was no feedback mechanism indicating the correct position.
- Incorporation of a removable animal support with adjustable position of radiofrequency coil, anesthesia mask and stereotactic fixation; correspondingly the animal could be placed in the FMT probe without interfering with optical components thereby warranting optical alignment.
- All components (MEMS, imaging module, MRI surface coil) were positioned in a closed cylindrical containment that was light tight and contained radiofrequency shielding for all electronic components associated with the optical sensor. Connection to the 'outside world' is achieved through connectors for optical fibers, radiofrequency cables, signal cables, power leads as well as for water tubing (thermoelectrical cooling system).
- Design of new MATLAB based program for controlling the FMT system

2) factors contributing to enhanced sensitivity are

- Closable system-in-a-box design that largely avoided background signals due to stray light
- Incorporation of a new camera type with a novel scientific image sensor and improved specifications such as quantum efficiency, readout noise, and pixel resolution. In addition, the new camera could be efficiently cooled.
- The use of graded-index (GRIN) lenses enabled improving the laser beam profile.
- Incorporation of image distortion correction for the fisheye lens used to increase the field of view.

3) factors contributing to enhanced versatility are

- Incorporation of both reflection and transmission mode scanning
- Potential to operate system in multicolor mode by extending the current filter module (currently not implemented)

In the following subchapters we will describe the individual hard- and software components for FMT-MRI 3.0 design.

2.3.1 Imaging Module

The imaging module in the hybrid FMT-MRI system maps the light distribution at the sample surface elicited by the incident laser light both at the excitation and the emission wavelength. At the excitation wavelength the signal is governed by absorption and scattering properties of the sample, while at the emission wavelength in addition fluorescence properties such as fluorescence quantum yield have to be considered. Images are collected for each point of the irradiation scheme and data are stored as image stacks. The basic components of the imaging modules are the camera consisting of the objective lens, the image sensor and readout electronics. The objective lens maps the surface pattern onto the image sensor. The light is converted to electrons at the surface of the pixels (photoelectric effect, PE) [9]. The electric potential created by the electrons is then read out by the readout electronics.
In addition, the imaging module comprises bandpass filters for selecting the wavelength range of interest, a module for cooling the image sensor for sensitivity enhancement, and is placed inside a shielded box to minimize interference with the MRI measurements.

2.3.1.1 Camera

A camera system suited for operation in a high field MRI magnet with small bore diameter comes with demanding constraints. It has to be geometrically compact to fit inside the magnet bore (free access diameter 114mm in our case), must be MRI compatible, i.e. insensitive to static and dynamic magnetic fields as well as radiofrequency fields, but should nevertheless provide highly sensitivity and a large dynamic range. There is a variety of image sensors available for low light imaging [10]. The most common image sensors on the market today are charged-coupled device (CCD) and complementary metal-oxide semiconductor (CMOS) image sensors. In both types of image sensors photons are converted to electrons by the photoelectric effect. However, they differ in the way data are read out. In CCDs, PE electrons are transported row by row to the neighboring pixels. At the edge of the sensor they are transferred to the readout register where they are serially read out and converted to a digital

value. CMOS image sensors have in each pixels transistors preprocess signals at the pixel level (e.g. amplification) and each pixel can be addressed individually [11]. Image sensors are quickly evolving. In general, scientific cameras for low light applications were until recently usually CCD image sensors while CMOS image sensors were for the choice for imaging at high frame rates. In 2009 a consortium of leading scientific camera manufacturer (Andor, PCO and FairChild Imaging/BAESystems) presented a new image sensor type called scientific CMOS (sCMOS). This type of image sensor is based on CMOS image sensors, but with optimized pixel architecture and readout scheme. This novel sensor combines the advantages of both CCD and CMOS image sensors: It has high sensitivity, low readout noise, high frame rate, high resolution and high dynamic range [12] ,[4] (Fig. 2.9). The sensitivity of a pixel in an image sensor can be described by the signal-to-noise ratio. The signal in a single pixel is proportional to the number of electrons N_e generated in the PE process,

$$N_e = Q_E \, N_P \tag{2.1}$$

where N_P indicates the number of photons impinging on the pixel and Q_E is the quantum efficiency or the probability of a photon generating a free electron within the pixel. The noise consists of several

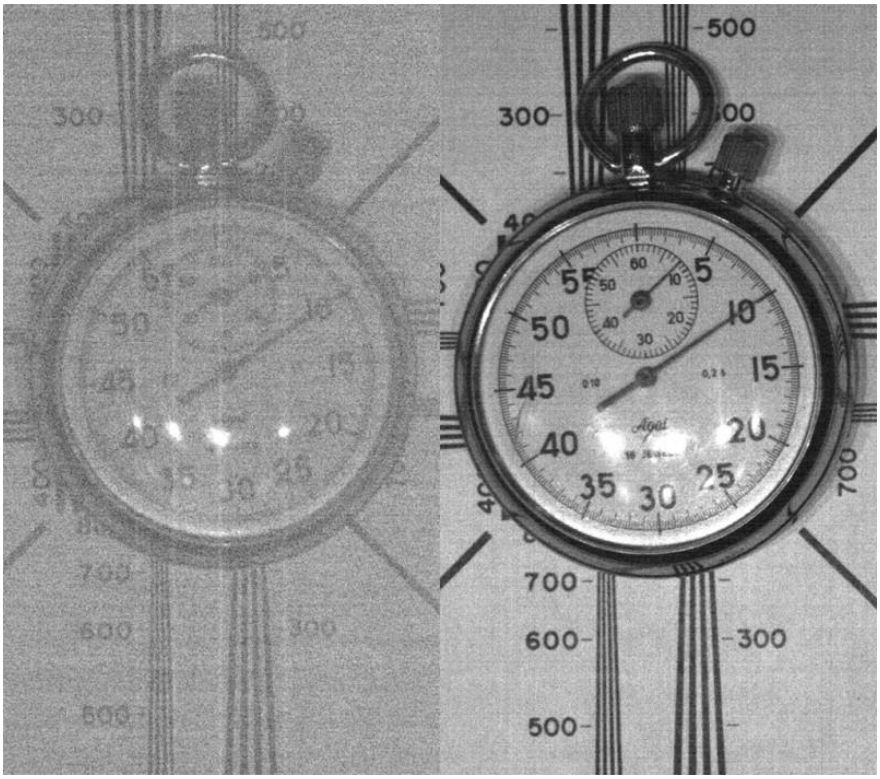

Fig. 2.9 Comparison of a low-light scene of a cooled CCD camera at 1 ms exposure time and cooled to 10° C (left side) and with a prototype of a sCMOS image sensor, no cooling at 1.3ms exposure time (right side) demonstrating the superior performance of the latter sensor [4].

contributions: The shot noise, the dark current noise and the read out noise. The shot noise is the intrinsic noise of a light signal and follows the Poisson distribution:

$$\delta_{Signal}^2 = \sqrt{Q_E\, N_P} \tag{2.2}$$

The dark current is an intrinsic physical property of a photodiode (which is the photosensitive part of a camera pixel) and depends approximately exponentially on the temperature [13]. The dark current generates an undesired signal in a pixel, which is not depending on the light. It can be corrected in a straightforward manner by subtracting a dark frame (obtained in the absence of any incident light) from the actual image (both recorded with the same integration time). Yet, the dark current also contributes to the noise, as it follows the Poisson distribution, as well. Cooling of the camera and choosing small integration times minimizes dark current noise contribution, which can be effectively neglected.

Readout noise originates from the readout electronics of the image sensor. The manufacturer of the camera has to carefully design the readout electronics to minimize this noise contribution, which is a critical figure of merit for a sensitive camera. Sources of this noise include output amplifier noise, on-chip electronic noise, any uncorrected offset noise or pixel reset noise [14]. For a more detailed description on noise associated to a camera the reader is referred to [15].

Combining the various contributions we obtain [16]:

$$SNR = \frac{Signal}{Noise} = \frac{Q_E\, N_P}{\sqrt{Q_E\, N_P + \delta_{darkcurrent}^2 + \delta_{readout}^2}} \tag{2.3}$$

For imaging at low light levels the camera should be characterized by high quantum efficiency as SNR scales approximately with $\sqrt{Q_e}$, also by low read out noise and additionally the image sensor should be cooled.

Additionally, there is a noise contribution arising from the fact that not every pixel has the same properties. This is called fixed pattern noise. This is due to process variations during production of an imaging sensor leading e.g. in small differences in the properties of the transistors [17]. Two types of fixed pattern noise arise: dark-signal-non-uniformity (DSNU) and Pixel-response-non-uniformity (PRNU). DSNU is due to variations of the dark current in the pixels and PRNU is a difference in sensitivity of the pixels [13]. DSNU and PRNU can be corrected for by subtracting a dark frame and attributing each pixel with a correcting gain and offset, respectively [18].

Finding a suitable camera for the FMT-MRI 3.0 system was challenging. Most of the commercially available scientific cameras have an integrated cooling with fan. The fans have usually an integrated

electric motor and are therefore not MRI compatible. Some cameras have magnetic parts such as nickel-plated electrodes or inductances and are not MRI-compatible, either. Moreover, in most cases they are too bulky. The camera has not only to fit inside the small animal MRI bore which has a diameter of 11.4cm, but it should also be able to record well-focused images of the sample placed in the middle of the MRI bore.

The best option for our purpose was a pco.edge board-level (PCO, Kelheim, Germany), which is provided without casing and which comprises a highly sensitive sCMOS image sensor (CIS2020) mounted on a PCB with 60mm width. This narrow geometry allows to place the board at around 4 cm distance to the z-axis of the MRI bore leaving enough working distance to record well-focused images

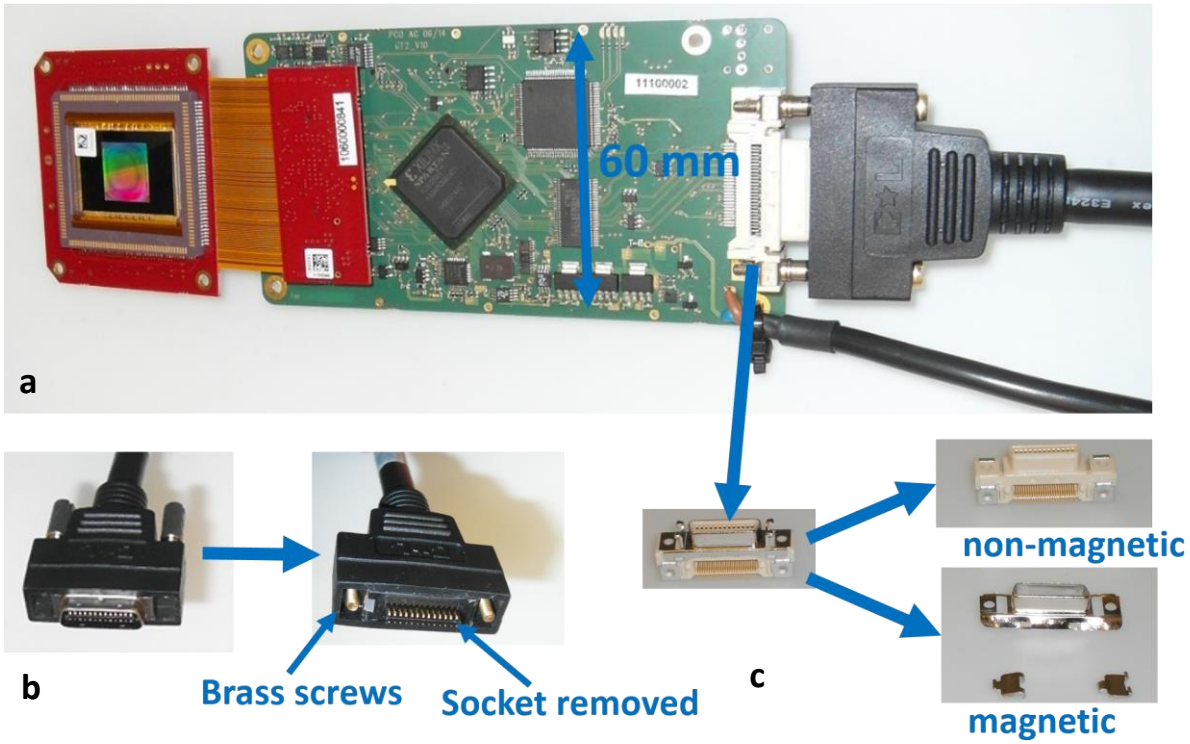

Fig. 2.10 pco.edge board level with CIS2020 image sensor and its modification to make it MRI-compatible (a) modified power cable and removed switching regulator (b) Magnetic socket removed and screws replaced on the data cable connector male side (c) and socket removed on female side.

and ensure sufficient large FOV covering of typically 25 x 25 mm^2. In addition, the PCB has a 21 x 21mm^2 square opening behind the image sensor that allows for efficient thermoelectric cooling. A permanent magnet was used to test the camera for magnetic components. A switching regulator and the data cable socket (male and female parts) had to be removed and magnetic screws were replaced with brass screws (Fig. 2.10). The modified camera did not experience any attractive forces when placed in the magnetic field.

The image sensor has a read out noise of 0.9e- (median) and the peak quantum efficiency is above 70% (Fig. 2.11). It has significantly higher sensitivity than the image sensor of the FMT-MRI 2.0 (Table 2.1). The pixel resolution is 2048x2048 and it comes with a PRNU below 0.5%, a DSNU below 1e- rms and a dark current value of 0.5e- per pixel and per second at 5°C. The dynamic range is 33000:1.

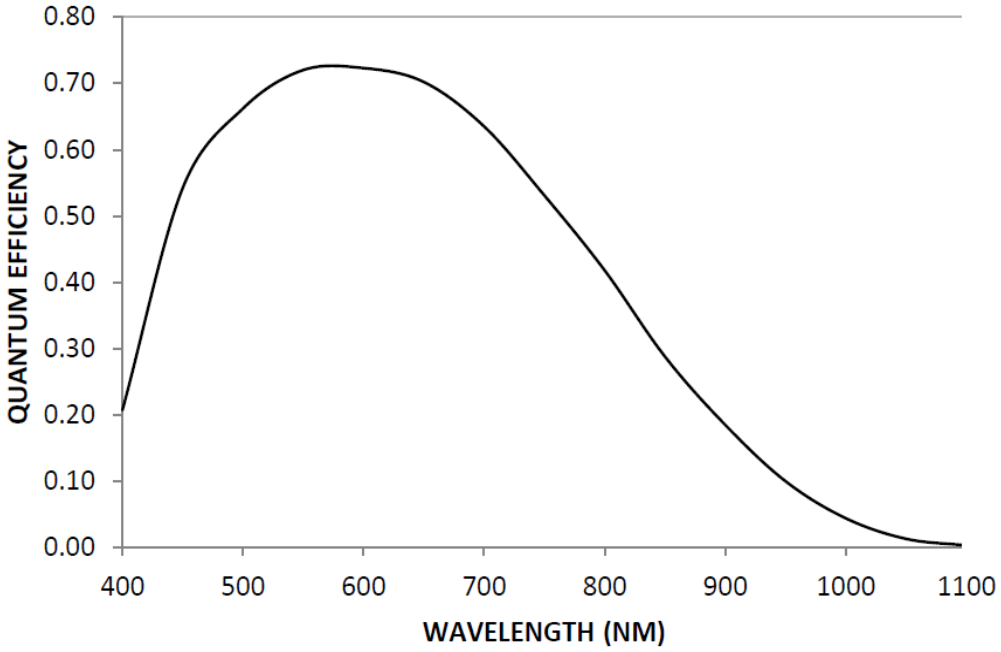

Fig. 2.11 Quantum efficiency of the image sensor CIS2020 [19]

Imager Type	LL_256_HDR	CIS2020
Photosensor	CMOS	sCMOS
Company	CSEM	PCO
Quantum efficiency (700nm)	25% (est.)	64%
Read out noise	1.2 e-	0.9 e- (median)
Pixel resolution	256x256	2048x2048
Pixelsize	11µmx11µm	6.5µmx6.5µm

Table 2.1 Comparison of image sensor used in FMT-MRI 2.0 system and FMT-MRI 3.0 system

2.3.1.2 Cooling Module

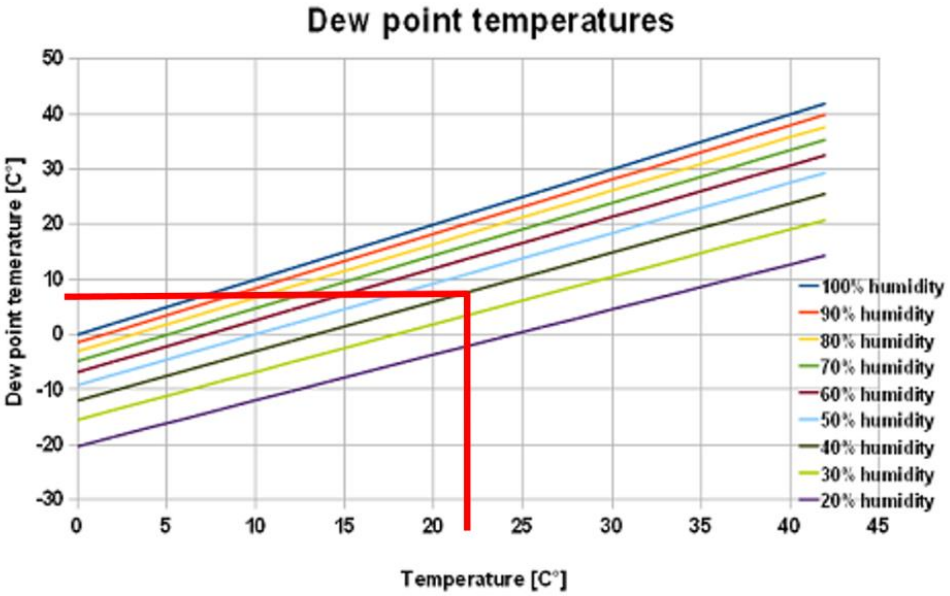

Fig. 2.12 Dew point temperatures in dependence of the humidity. The red lines show the case for the lab environment: 22°C and a humidity of 40% [20].

The dark current depends in an approximately exponential manner on the temperature [21]. The dark current of the CIS2020 sensor has been reported as 0.5 e-/pixel/s at 5° C [22]) and 35 e-/pixel/s at 20°C. However, it was observed, that the image sensor reaches temperatures up to 70°C during normal operation. This led to the conclusion that cooling is a crucial aspect for low-light imaging, as already seen with the camera of the FMT-MRI 2.0 system (Fig. 2.6).

The CMOS image sensor used for the FMT-MRI 2.0 was cooled to temperatures below 0° C. This rendered the cooling system more complex as a constant flow of N_2 had to be applied to prevent water condensation on the image sensor and electronic circuitry. Water droplets might have caused short-circuits and damaged the electronic circuitry. Given the space constraints of the FMT-MRI 3.0 system, we decided to cool the image sensor at a temperature above the dew point temperature. In the controlled environment of the laboratory in AIC at ETH Zurich, the temperature is kept constant at 22° C and the humidity is of 40%. Under this condition the dew point is 8°C (Fig. 2.12). Including a safety margin it was decided to cool the camera to 10°C. At this temperature, there is still substantial benefit of cooling with regard to the sensor sensitivity.

Cooling was achieved by using a thermoelectric cooling (TEC) device (Deltron, Kirchberg, Switzerland) of dimensions 20 x 20 x 2.6 mm^3 matching the square opening in the PCB board at the back end of the sensor. There were substantial Lorentz forces exerted on the TEC power leads according to

$$\vec{F}_L = I \int \overrightarrow{dl}\, x\vec{B} \qquad (2.4)$$

where I is the electric current, $\overrightarrow{dl}$ is an infinitesimal short piece of length of the electric conductor and $\vec{B}$ the magnetic flux (9.4T in our case) . Thus, the two power lines feeding the TEC were twisted to neutralize the forces imposed on the cable, which can reach several Newtons at 9.4T and a current at several Amperes used for the TEC.

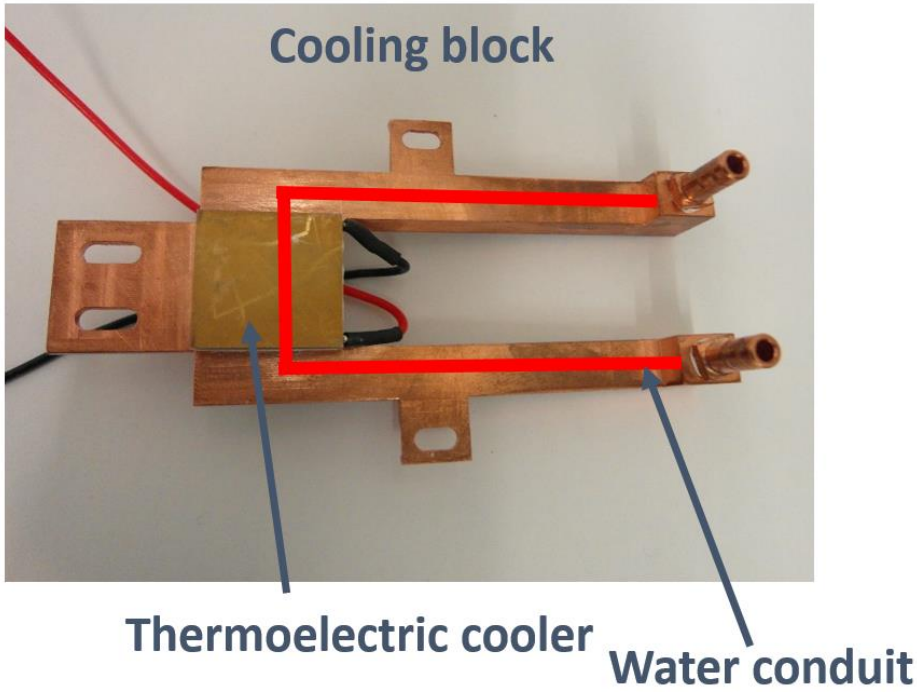

Fig. 2.13 Copper cooling block with TEC and the tubing connection site on the right side.

The TEC has to be cooled in order to dissipate the heat transmitted from the sensor. A home-built water cooling system consisting of a water-flushed copper block was designed for this purpose (Fig. 2.13). Copper was chosen for its excellent thermal conductance properties. Connections for the water tubes were kept at a distance to any electronic device to prevent water condensation or minimizing the impact of potential leakage that might cause short-circuits in the electronic circuitry. The water channels in the copper block were drilled and unnecessary openings sealed with copper screws to

make them water tight. The copper block was tested with air at 1 bar under water to check for tightness by watching. Furthermore, the block was flushed with water for 24 hours revealing no leakage. The assembly of the cooling device and the camera PCB is shown in Fig. 2.14. In operation for FMT studies, the TEC is used at cooling power values clearly below its maximum capacity. The required current is around 1A (maximal allowed current amplitude: 11.3 A). At the beginning of camera operation, when the camera has not yet heated up, even less power is needed.

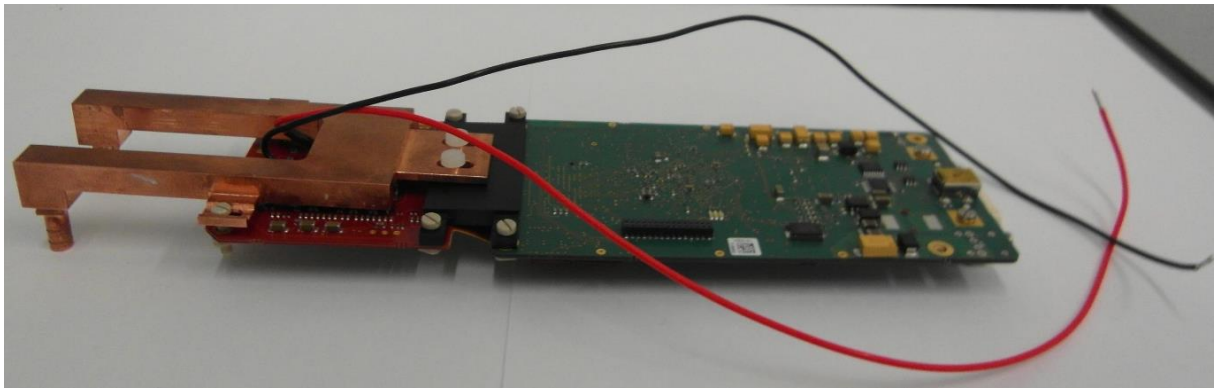

Fig. 2.14 PCO.edge board-level with TEC and copper block for cooling.

2.3.1.3 EMC Considerations

MRI involves strong electromagnetic interactions and hence any electronic equipment operated in an MRI scanner is subject to electromagnetic interference. Apart from the static magnetic field (9.4T) there are magnetic field gradients of up to 400mT/m that are switched in the sub-millisecond time range, also inducing strong vibrations. The MRI experiment involves powerful radiofrequency pulses, while image acquisition is based on the reception of weak radiofrequency signals that require sensitive detection circuitry rendering susceptible to interference of nearby electronic devices such as the camera PCB. The camera and the scanning modules have to operate in this hostile environment, which demands for measures to minimize cross-talk between the MRI and FMT systems. To evaluate the severity of the problem the cross-talk was assessed prior to any measure taken. The camera was positioned inside the MRI bore together with a water-filled tube and a surface coil was used for recording the MR signal readout. The sensitivity of MRI was dramatically reduced as soon as the camera was switched on: zipper artefacts indicative of specific frequencies recorded appeared on the images and the signal-to-noise ratio was degraded from SNR=181 to SNR=10 (Fig. 2.15).

High sensitivity in MRI is important not only to catch weak signals, but also because it is of high interest for fast readouts when recording dynamic signals. The deterioration of the MRI signal in the non-

shielded case clearly indicates the necessity of incorporating effective shielding measures in our system design. While current shielding theory yields large deviations from results obtained under practical conditions [23] it is nevertheless helpful in providing guidelines and as a rule of thumb to improve shielding performance.

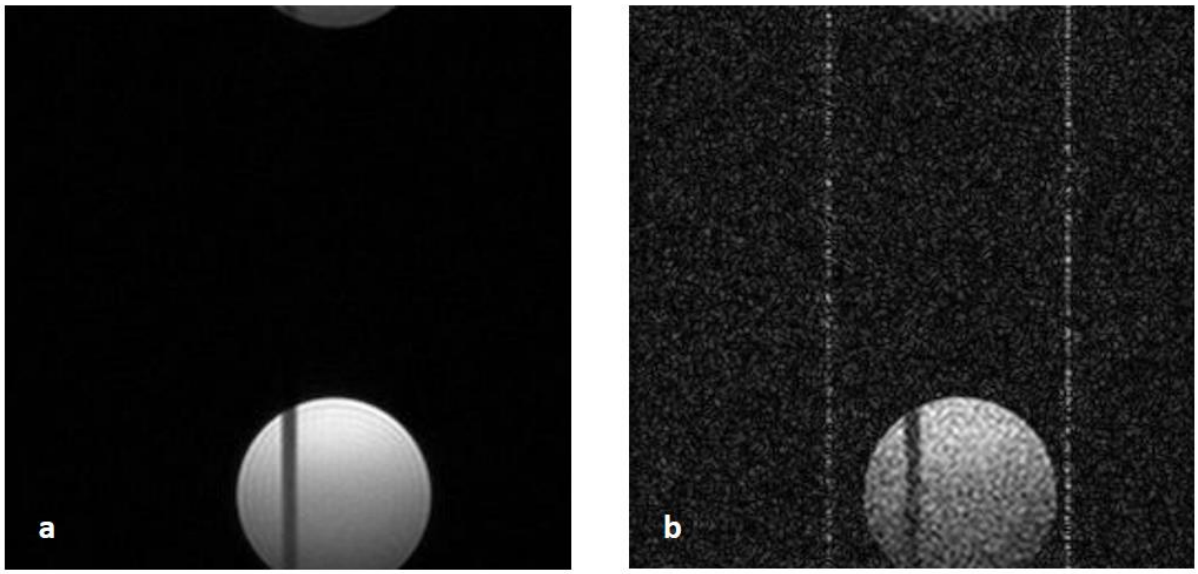

Fig. 2.15 Transverse cross-section of a water-filled tube recorded with the 9.4T MRI (a) without and (b) with camera running simultaneously.

The shielding effectiveness of a single shield is given by:

$$S = A + R + B \tag{2.5}$$

where A is the penetration loss due to absorption of the incident electromagnetic wave, R is the reflection loss due to single reflections at the shield and B a corrective term related to multiple reflections, which can be negative or positive [23]. Real shielding enclosures have discontinuities such as holes, seams, input/output lines and power lines. The shielding effectiveness is usually limited by those discontinuities and not the shielding material [24]. Special attention has therefore to be paid on these discontinuities. Shielding can be improved if seams are closed with metallic gaskets. Good contact is necessary and pressure should be applied to close it. Each hole decreases the effectiveness of the shielding and therefore both the number and diameter of the holes should be minimized.

The shielding effectiveness of a compact shield enclosure with a single hole of diameter D can be approximated by [24]:

$$S = 20\log(\frac{\lambda}{2D}) \tag{2.6}$$

with λ as the wavelength of the electromagnetic wave. Obviously, a camera box requires at least one opening to allow light reaching the sensor. Another critical source of leakage are wires penetrating the enclosure. These wires have to be shielded or filtered.

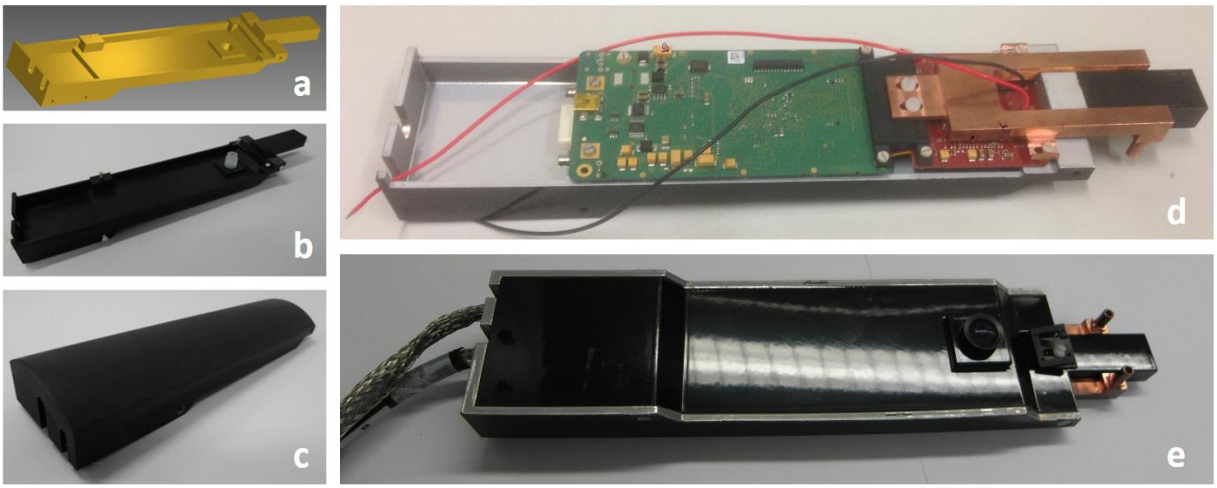

Fig. 2.16 Camera box. (a) CAD design and (b) 3D production of bottom piece. (c) 3D production of the lid. (d) Bottom piece with thin film of aluminum produced with PVD, camera board and cooling module. (e) Closed shielding box flipped with shielded data and power cable.

In the FMT-MRI 2.0 system, the camera was shielded with copper tape. While copper tape was efficient in shielding, it could not be considered a robust long-term solution, as bits and pieces got loose over time. Also, access to the camera was cumbersome. Therefore, based on this experience it was decided to go for a new solution in the FMT-MRI 3.0 system: A camera box made of ABS covered with a thin film of aluminum (Fig. 2.16). The thin film is deposited with physical vapor deposition (Kaltbrunner, Grenchen, Switzerland), which is a process where Aluminum is heated up to high temperature and its vapor is deposited on the substrate, in our case the camera casing, inside a vacuum chamber. The thin film of aluminum has a thickness of 2.5 µm. For frequencies >30 MHz thin coating on plastic is sufficient for shielding, as electrical currents are flowing in the surface layers of the structure only [24]. Damping was specified as 74dB at 250 MHz and 78 dB at 500 MHz; thus, we expect the damping of approximately 76dB at a ^{1}H resonance frequency of 400 MHz at 9.4T. The cylindrical cover of the box was designed such that the distance of the image sensor to the sample (focal plane) could be maximized. A larger distance of the sample to the image sensor increases the FOV of the camera. Additionally, care was taken to design cover and the bottom part of the box substantially overlapping to maintain the efficacy of shielding. The thread (M12) for the objective lens is designed such that the objective lens can never be screwed into the image sensor to avoid potential damage. The corresponding opening in the shield

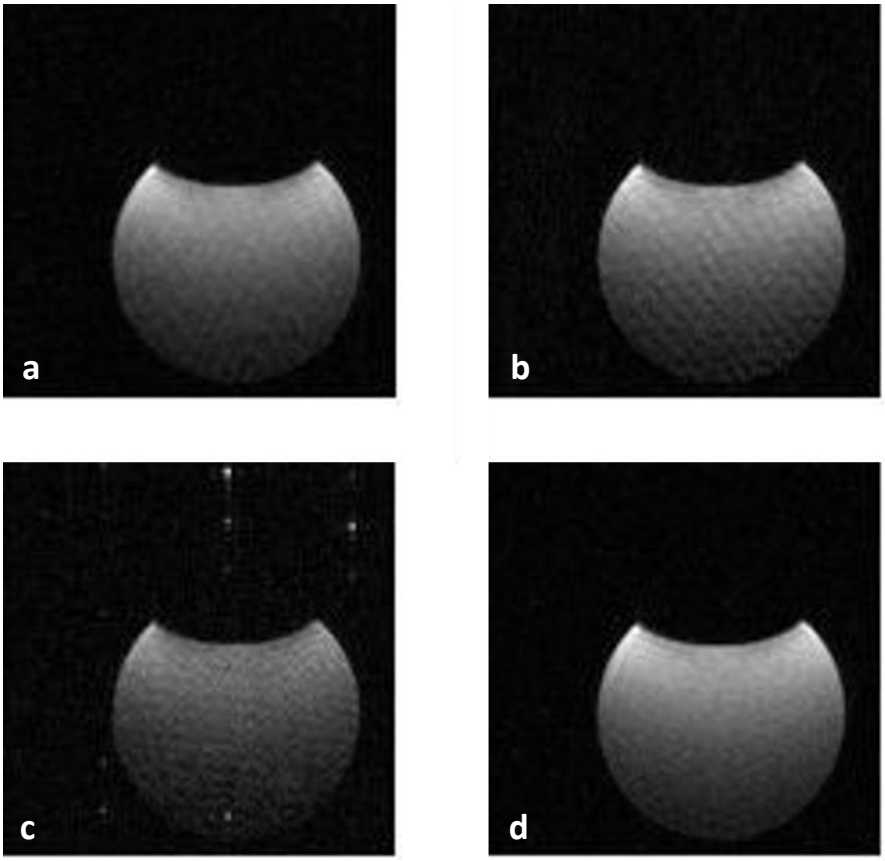

Fig. 2.17 MR readout of a tube filled with water combined with shielded camera in various situations recorded with FLASH, TE=2.51ms, TR=12.5ms, Matrix 110x110, FOV=22mmx22mm (a) Everything switched off, (b) Computer running (c) Camera program started (d) Camera power cable unplugged.

was 10.1mm, which reduced the shielding efficacy to 31dB. The box design near the objective lens was adjusted to allow space for the MEMS mirror used in reflection mode. This MEMS mirror should be placed as close as possible to the objective lens to prevent coil shadows on the sample and as far away as possible from the sample surface in order to maximize the scanning field of the MEMS mirror, which has limited angular coverage of $\pm$14 degrees.

Bottom and cover of the shielding box were sealed with Amucor shielding gaskets (Holland Shielding Systems, Dordrecht, Netherlands) to prevent leakage of radio waves at the seam. Moreover, the power cable leaving the box is shielded with cable shielding (Holland Shielding Systems, Dordrecht, Netherlands). The camera data cable comes with a shielding layer. All shielding surfaces are electrically connected to ground.

To test shielding efficiency, MRI images of a water phantom were acquired using a FLASH sequence while the camera was in operation (Fig. 2.17). An SNR value of SNR=25 was measured, which corresponded to a twofold reduction to the values measured when the camera was switched off (Fig.

2.17c) demonstrating that effective shielding as in the absence of any shielding the SNR was reduced more than 18-times. Of course, it would be desirable to further reduce the crosstalk between the two imaging modalities. As described before, limiting factors in shielding are seams and holes. The seam has been closed with shielding gaskets, the effectiveness of which depends on the pressure exerted on the seam. According to [23] an optimal pressure is 20 psi i.e. 1.4 bar. In our case, we roughly estimate a pressure of <4 psi or <0.3 bar based on the assumption that we were exerting a force below

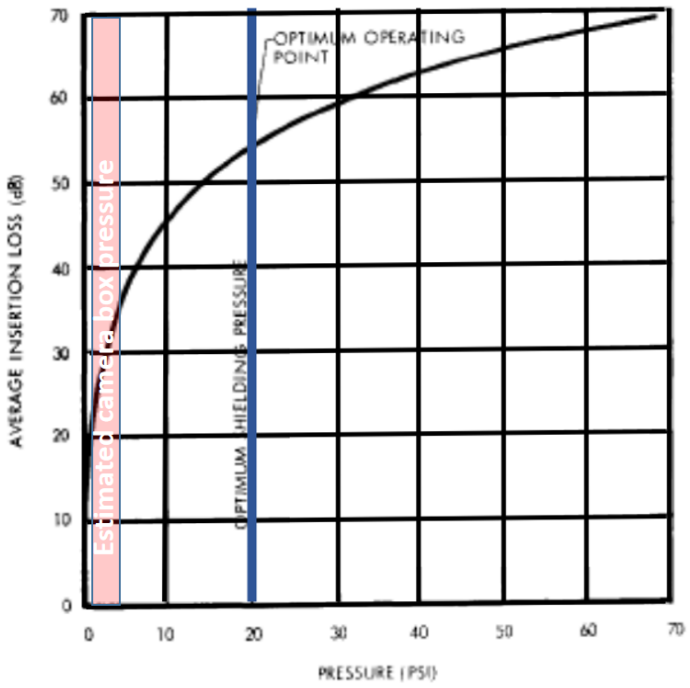

Fig. 2.18 Typical shielding effectiveness of a shielding gasket as a function of gasket pressure and estimation of the camera box pressure. Adapted from [23].

50N to close the camera box for insertion of the plastic screws at the side and an area of the shielding gasket of 0.6x30 cm^2. Therefore the shielding effectiveness results to 20-35dB (Fig. 2.18).

The aluminum layer on the camera box is expected to have a shielding effectiveness of S>74dB, the objective thread reduces it to S=31dB according to formula (2.6) and the seam has 20dB<S<35dB. Therefore, as expected, leakage occurs mainly at the hole and the seam. Strategies to reduced leakage involve increasing the pressure on the gasket, e.g. by fixing bottom and cover with brass screws. Leakage at the objective port could be reduced by using an RF chimney, i.e. a conducting cylinder that acts as a waveguide that does not conduct the electromagnetic wave below the cut-off frequency. The cut-off frequency f_c represents the minimal frequency that is conducting inside the waveguide without any losses. The intensity of a wave with frequency $f < f_c$ decreases exponentially depending on the

wavelength. The attenuation of a wave in a basic TE_{11}-mode inside a cylindrical waveguide with diameter d and length L can be approximated by:

$$A(dB) \approx 32 \cdot \frac{L}{d} \cdot \sqrt{1 - \left(\frac{f}{f_c}\right)^2} \qquad (2.7)$$

Therefore, the attenuation depends on geometry of the waveguide and frequency of the wave. The cut-off frequency for an opening of 10mm is 17.5 GHz. The frequency dependence of the attenuation is only marginal at a frequency of <400 MHz and we can approximate equation (2.7) to:

$$\mathrm{A(dB)} \approx 32 \cdot \frac{\mathrm{L}}{\mathrm{d}} \qquad (2.8)$$

The attenuation in function of the length for a waveguide with 10mm diameter is given in Fig. 2.19. An attenuation of 77dB (corresponding to the attenuation of the camera box) is reached with a cylindrical length of 24mm, which is too long for the compact system design. 10-12mm is better fitting into the design, which would attenuate 32-38 dB (Fig. 2.19).

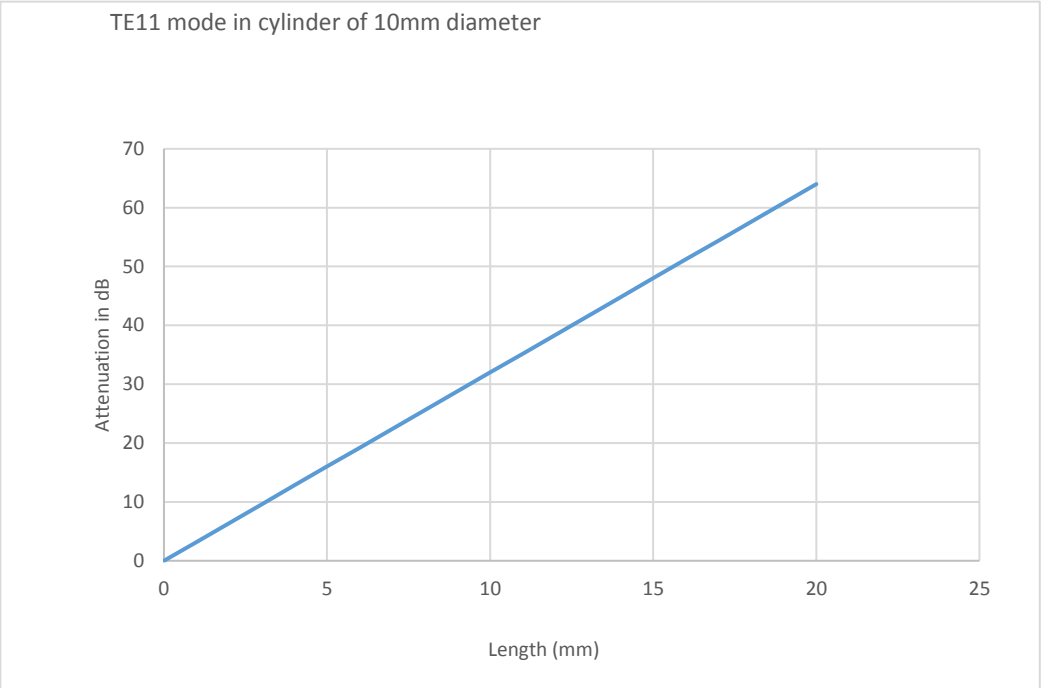

Fig. 2.19 Attenuation of the shield with a circular wave guide opening in dependence of its length.

2.3.1.4 Objective Lens and Distortion Correction

The objective lens used is a fisheye lens (V-4301, Marshall Electronics, Torrance, California, USA) in order to achieve a wide angular field of view (131° in our case) and thereby to increase the FOV of the

image sensor. Yet, it comes at the cost of image distortion, so-called barrel distortion (Fig. 2.20a). For proper FMT reconstruction it is important to correct for this geometrical distortion. This was achieved using the Computer Vision System Toolbox of MATLAB ((MathWorks, Natick, USA), which provides functions for distortion corrections. The camera calibrator app of MATLAB estimates the distortion parameters of a lens, which are computed based on a set of images taken with the camera. A plate with a checkerboard pattern was used for the purpose and imaged 50 times at various distances and angles. This basis imaging set was used as input for the camera calibrator app. The MATLAB function corrects the distorted image and the parameters are used for preprocessing of any further images recorded with this configuration.

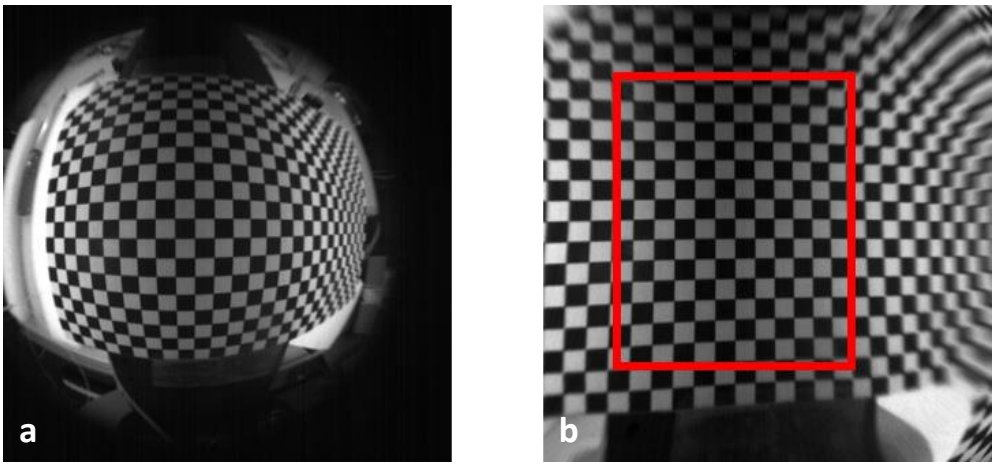

Fig. 2.20 (a) Image recorded with sCMOS imager and fisheye lens showing barrel distortion. (b) Same image as in (a), after distortion correction. The FMT data is recorded only inside the red rectangle, which shows good distortion correction. The checkerboard pattern was printed on a paper, which is placed on the FMT probe sample platform, which explains the bending on the right side due to gravity.

2.3.1.5 Filter Module

Two single-band bandpass filters (Semrock, Rochester, New York, USA) are used for selective detection at the excitation and emission wavelength. The filters used are characterized by central wavelengths of 660nm and 720nm for excitation and emission light, respectively, with corresponding bandwidth of 20.2nm and 19.2nm FWHM, respectively. The filters are interference filters and their behavior is dependent on the angle of incidence. The recommended angle of incidence of the light is 0° +/-5°, which is not compatible with the use of a fisheye objective lens with an angular field of view of 131°. For larger angles the transmission window of the filter is shifted towards the shorter wavelengths, and as a consequence a light beam at a wavelength of 660nm does not anymore pass the filter at an incidence angle of 60°. The cone of the light beam leaving the objective lens has an apex angle of

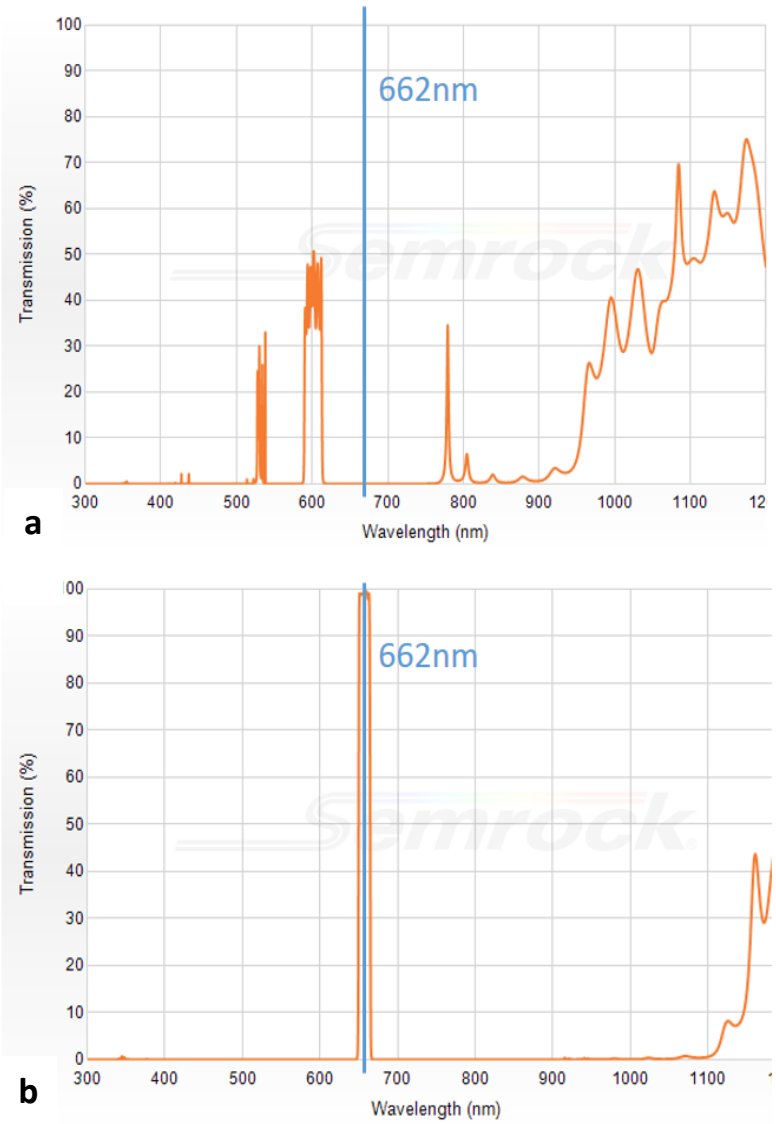

Fig. 2.21 Filter spectrum of an interference filter with nominal value 660nm at an angle of incidence of (a) 60° and (b) 15°. Adapted from [1].

approximately 30°. Assuming an angle of incidence of 15°, the wavelength shift of the filter is minimal and hence light at a wavelength of 660nm would pass (Fig. 2.21b.). Therefore, it is essential to position the interference filters between the objective lens and the image sensor, which is a challenge as the gap between lens and sensor is only 5mm. In the current design, a drawer-mechanism was implemented for changing/selecting the filter, which was preferred in comparison to a filter-wheel due to its simplicity (Fig. 2.22). The appropriate filter can be selected from outside the MRI, when the hybrid system is in operation.

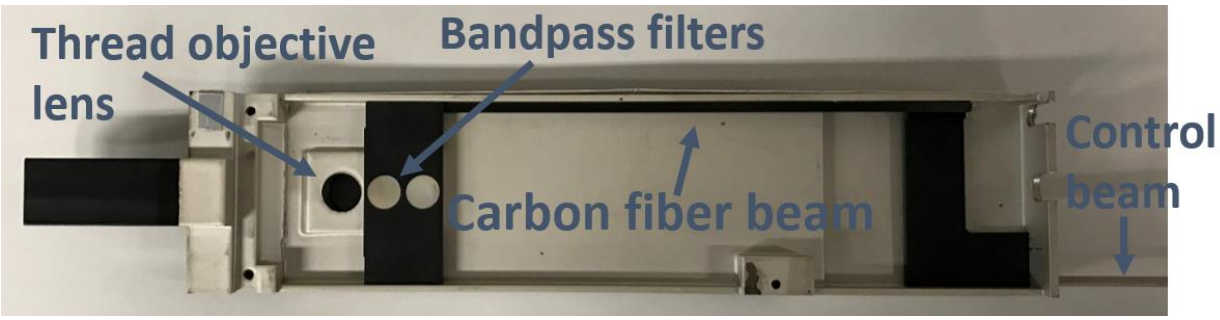

Fig. 2.22 Drawer-mechanism design of the filter module. The filter module has 3 positions: 1. No filter 2. Excitation filter 3. Emission filter.

2.3.2. Illumination Module

A diode laser (Coherent, Santa Clara, USA) emitting at 662nm was used as light source. The laser beam hits first a beam splitter (Fig. 2.23a), where the deflected beam is used to measure the laser power (power meter, Thorlabs, Newton, USA). The laser is then coupled into a single mode fiber (Thorlabs, Newton, USA) using two mirrors (Thorlabs, Newton, USA) and a fiber collimator (Thorlabs, Newton, USA) with a focal length of f=4.6mm. The fiber has a mode field diameter between 3.6 and 5.3 µm and NA=0.12. At the FMT probe the fiber end is connected with a mating sleeve to a second single-mode fiber inside the FMT probe, a pigtail fiber with a ferrule that is designed for combination with a GRIN lens (0.23 pitch, effective focal length f=1.85mm, working distance 0.234mm, Thorlabs, Newton, USA). The fiber is connected to a GRIN lens protected using a home-made holder (Fig. 2.23b). The surface of both the ferrule and GRIN lens are inclined by an angle of 8° to avoid back-reflections to the laser. It is a challenge and time-consuming task to couple the laser into the 4.3 µm single-mode fiber core. A single-mode fiber is preferred compared to a multi-mode fiber, which would have much larger core diameters and therefore would make coupling much easier. Yet, collimation of the beam leaving the fiber would be problematic: the collimated beam of a multi-mode fiber would be much more divergent than that of a single mode fiber. Using ray optics as approximate model, the divergence angle can be calculated for small angles according to:

$$\tan\theta \approx \theta = \frac{a}{F} \qquad (2.9)$$

with a being half of the fiber core diameter and F the focal length. In the single core fiber the divergence angle is approximatively 0.1°. The multimode fiber has typically a diameter of 100 µm and a divergence angle of 1.5°. The beam diameter would increase by over 5mm after every 10cm, which

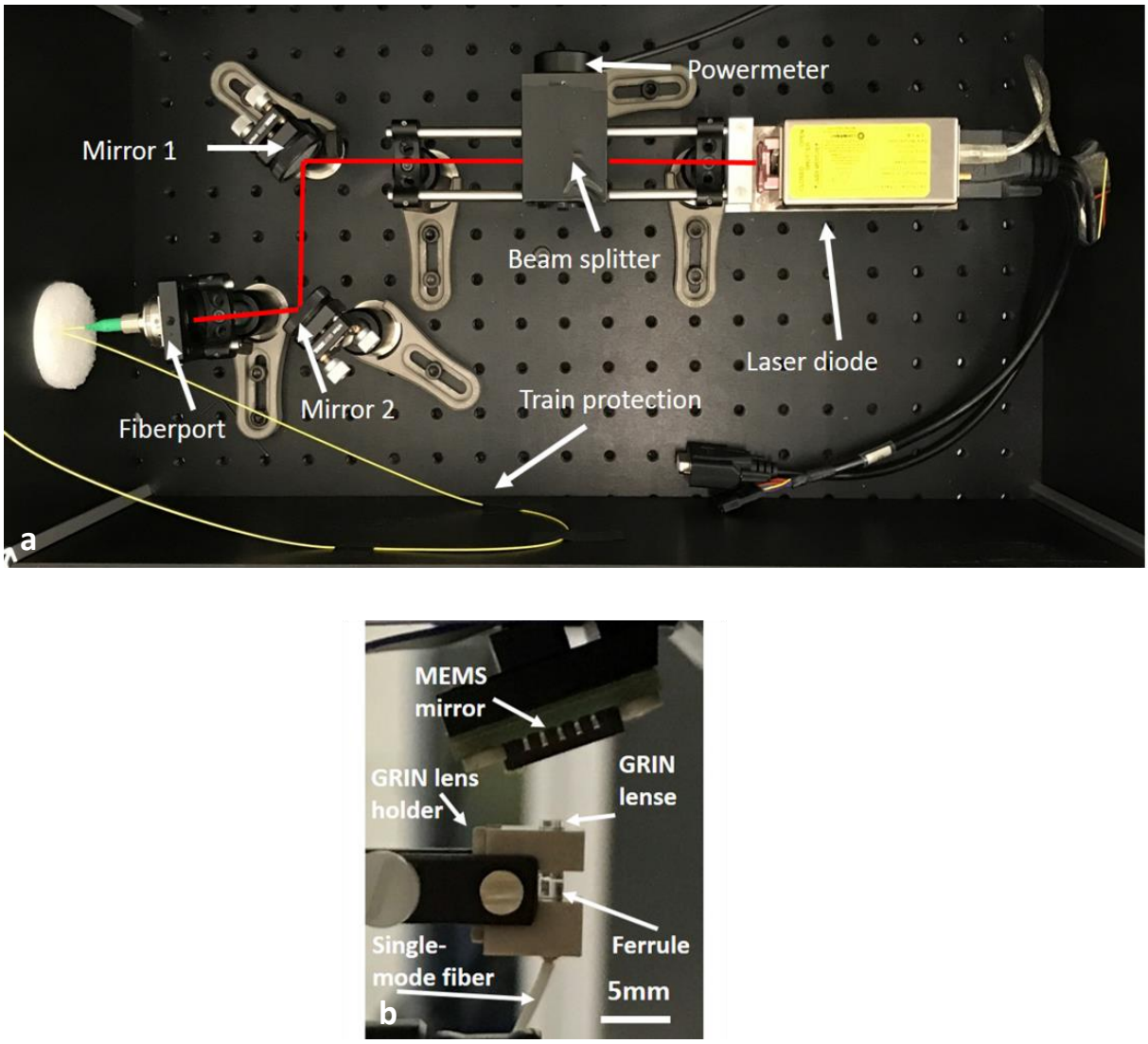

Fig. 2.23 Illumination module. (a) Laser coupling into the single mode fiber and power meter (b) Laser exit of the fiber. A GRIN lens collimates the laser.

would cause problems in an FMT experiment. The beam diameter would vary strongly in function of the distance from fiber end to the sample. Additionally, the single-mode fiber has the advantage that it guides only one single mode and therefore, the beam is approximatively of Gaussian shape [25]. As fiber alignment is critical, measures have been taken to prevent the coupling site from mechanical strain.

The GRIN lens is compact (Ø1.8mm) and straightforward to mount and yields a highly focused light source. The intensity profile was characterized using the sCMOS camera. For this purpose the objective lens was removed and a low power laser beam was directed onto the sensor. The images recorded

were then analyzed with ImageJ [26] (Fig 2.24). The FWHM of the laser was found to be 0.22mm and the shape looks of Gaussian type as expected. This information is important for the FMT reconstruction to model the forward propagation of the light inside the tissue.

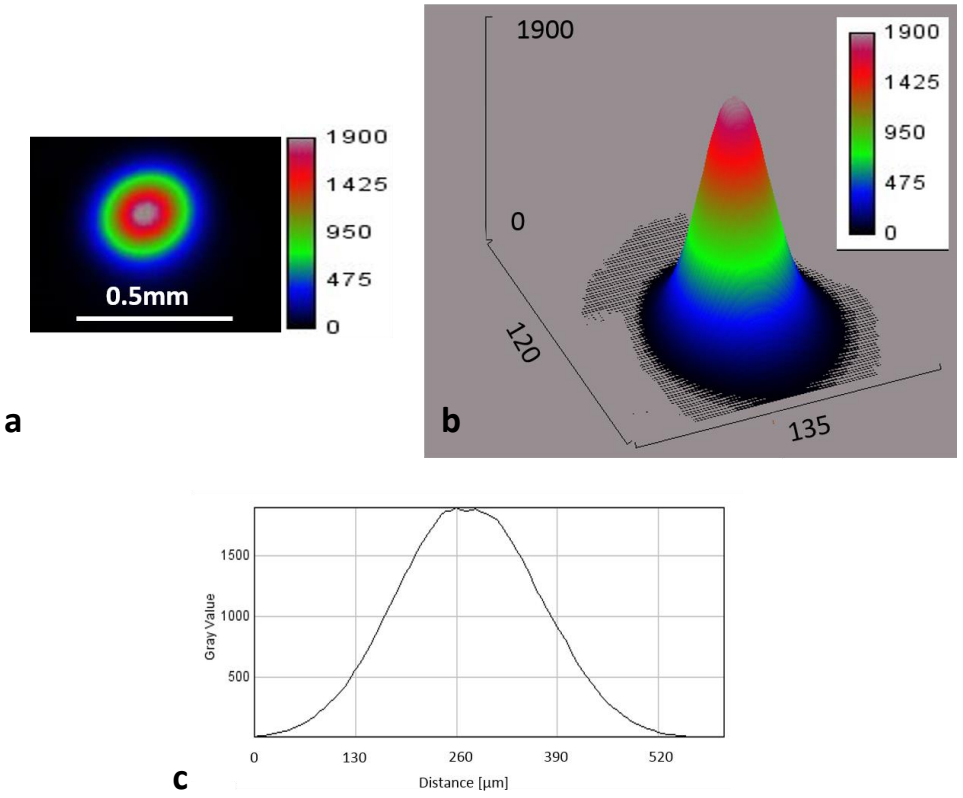

Fig. 2.24 Laser beam characterization (a) section (b) 3D view (c) profile with Gaussian-type shape as expected.

2.3.3 MEMS Mirror

A major change in the design of the hybrid FMT-MRI 3.0 was the incorporation of scanning devices into the FMT probe requiring scanners that were both compact and compatible with the MRI environment (static and dynamic magnetic fields and radiofrequency field). MEMS are miniaturized micro-electro-mechanical systems and use lithographic technologies originating from manufacturing of integrated circuits. MEMS laser scanners constitute a subgroup of MEMS and there are four common types of actuations used for them: Thermal, magnetic, piezoelectric and electrostatic [27]. Magnetic MEMS have a magnet inside and use the Lorentz force (equation 2.4) as actuation, yet are not compatible for use in an MRI system. While the other three subtypes fulfill the criteria we have decided to use electrostatic actuation, which has the advantage that there is no current flowing for operation of the MEMS, thereby avoiding effects due to Lorentz forces. Furthermore, no electric circuit loops are

required and thereby avoiding effects due to induction of electric currents caused by dynamically changing magnetic fields.

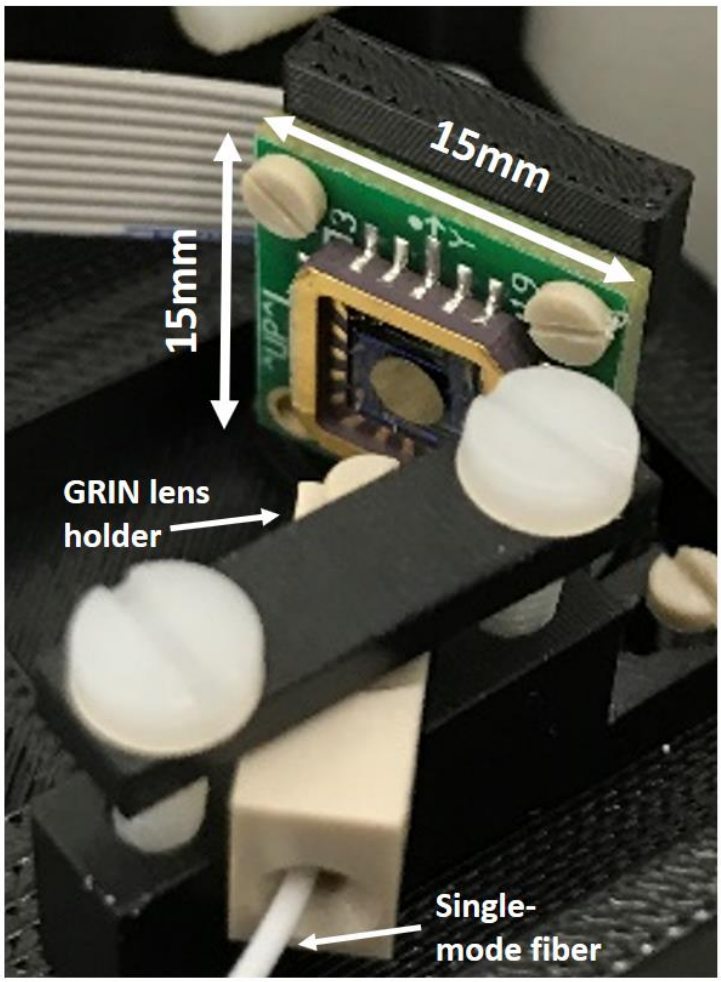

Fig. 2.25 MEMS mirror in position with single mode fiber and GRIN lens. The angle of incidence of the laser on the mirror is recommended as 22.5°.

Our choice is a linearized MEMS mirror (Fig. 2.25) with two axes that are "gimbal-less" using the electrostatic force as actuation principle (Mirrorcle Technologies, Richmond, USA) [3, 28]. The mirror is 3mm diameter and gold coated and enables scanning of a mechanical angle of ±7° resulting in a total optical angle of ±14°. It has a power consumption of less than 1mW and a precision higher than 0.0005° (or 1.8''). The MEMS is delivered with an antireflection-coated cover window. This glass led to multiple reflections of the laser beam and was therefore removed. The MEMS mirror uses a comb drive-based actuation. The fingers of the comb attract/repulse each other due to electrostatic force (Fig. 2.26).

The settling time from point-to-point for a MEMS mirror with 3.6mm and 2.4mm was below 1.8ms and 0.68ms in 99% of the cases, respectively [3].

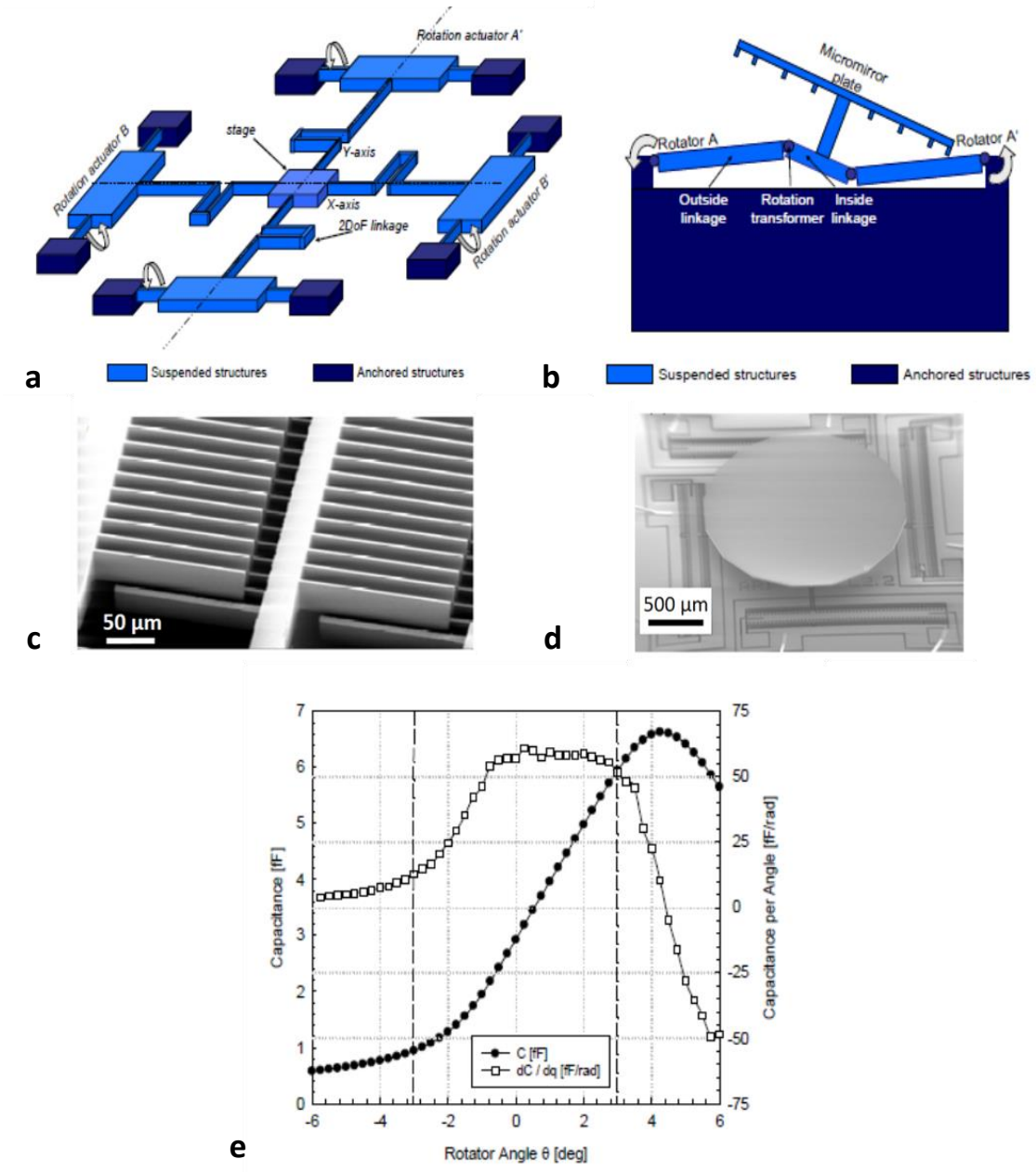

Fig. 2.26 Working principle of the MEMS mirror. (a)Two rotation actuators are used per degree of freedom. (b) shows principle of rotation of the mirror upon rotation of the rotation actuators. (c) SEM of a rotation actuator (d) mirror bonded onto the actuator (e) capacitance forming between the combdrive fingers. Figures adapted from [3].

2.3.4 RF Coil

The RF coil consists of a copper foil of 0.3mm thickness and has a rectangular shape with 24mmx22mm outer and 20mmx18mm inner diameter, respectively (Fig 2.27a). The foil was glued, using epoxy glue, on a slightly curved plastic former, which increases the filling factor of the coil and therefore increases signal-to-noise ratio during readout. The coil can be moved in foot-head direction to center the coil at the region of interest (ROI). The coil was covered with black paint to avoid the laser reflecting from the coil. Capactitor C1 and C2 (Voltronics, Cazenovia, USA) are adjustable capacitors with a capacitance range between 1 to 10 pF. C1 has the task to tune the resonance frequency to 400 MHz (Larmor frequency of the 9.4T MRI) and C2 is for impedance matching of the 50 Ohm BNC line, which minimizes reflections of the electromagnetic wave. C3 and C4 are MR compatible capacitors (Amercian Technical Ceramics, Huntington Station, USA) of fixed value 5.6pF and serve to balance the circuit towards the ground. C5 is a capacitor (Amercian Technical Ceramics, Huntington Station, USA) that divides the coil loop into two parts for voltage drop reduction during RF transmit operation (Fig. 2.27b). The coil has a quality factor of Q=126 in air, which was calculated as the ratio of the resonance frequency (400 MHz) divided by the difference of the two frequency values above and below the resonant frequency where the resonance curve has dropped by -3dB.

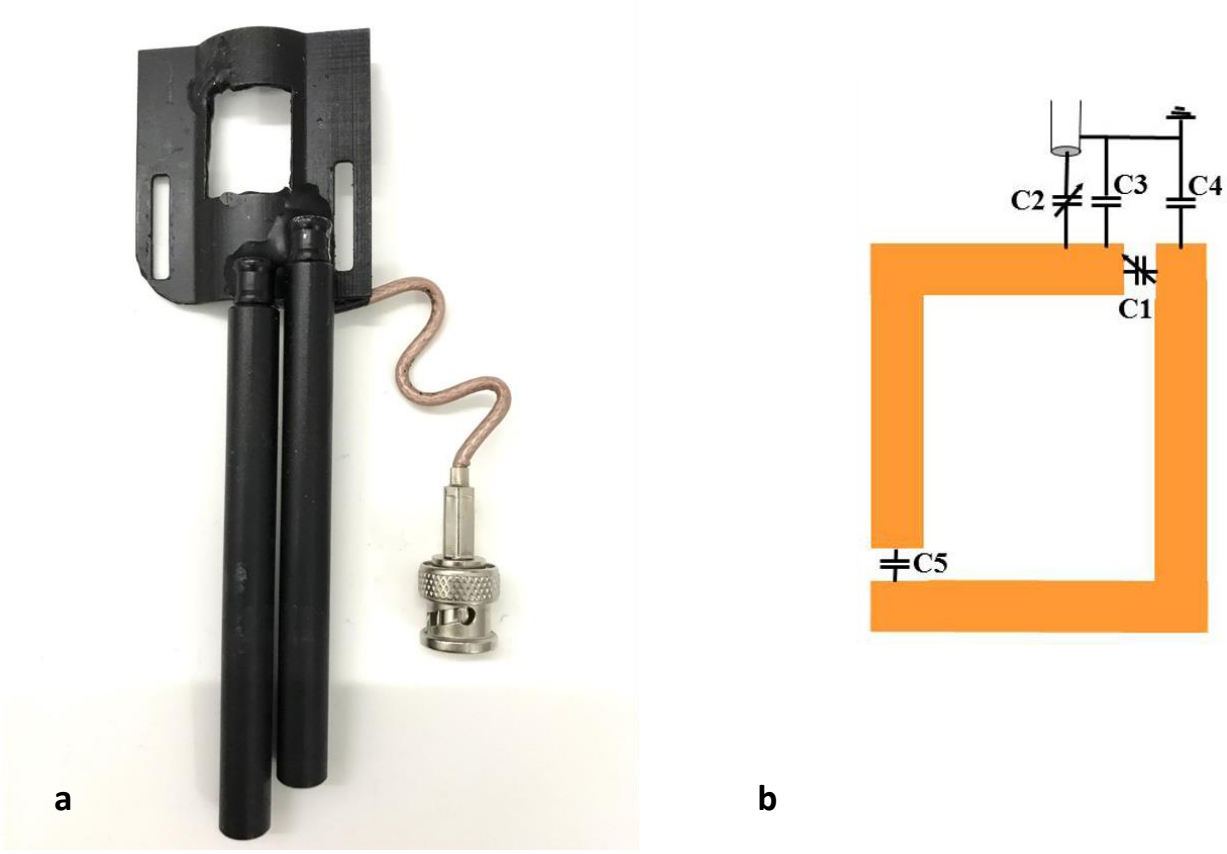

Fig. 2.27 (a) Coil with flexible cable and window of 20mm x 16mm. The plastic former is curved to maximize the fill factor for a mouse with average size. It is placed as close as possible on the mouse. The two rods are the two adjustable capacitors. They can be adjusted from outside the MRI scanner with two long sticks with a screwdriver-tip. (b) Coil circuit map depicted by courtesy of Dr. Mark Augath. It shows adjustable capacitors C1 for tuning and C2 for impedance matching. C3 and C4 are capacitors with a fixed value and balance the circuit towards the ground. C5 reduces voltages drops.

2.3.5 Control Software

Operation of the FMT module (scanning, data acquisition) was controlled by a MATLAB program. In order to enhance user friendliness, the number of input parameters required from the user was kept minimal. Two parameters are controlled by the user: The number of FMT source points in x- and y-direction and the integration time of the camera (ms). The grid covered by the FMT sources has a constant dimension of 16mmx20mm, which corresponds to the window of the MR surface coil. Default values for the source grid are 12×15 points. The range for the integration time is $1 \leq t_{int} \leq 4000\ [\mathrm{ms}]$, the actual value to be chosen depends on the intensity of the fluorescence signal: for strong signals 1ms is recommended (minimal value), for a very weak signal it may go up to 4s.

The code is based on software development kit (SDK) provided by both the camera (PCO, Kehlheim, Germany) and MEMS mirror manufacturer. In the beginning of the code the camera and MEMS mirror devices are opened using API-functions and basic settings are defined such as the trigger mode for switching-off the camera and the definition of output pin function of MEMS controller. Thereafter, the coordinates characterizing the coil window required for MEMS mirror operation are determined. Using the number of FMT source points entered by the user, the program calculates the increment in (x,y) values from source point to source point. The core of the program

1. calculates the MEMS mirror coordinates of each FMT source point in an incremental manner
2. calls a function of the MEMS mirror-API to position it to the new coordinates
3. calls the camera-API function for taking an image with the predefined exposure time and crops the image size to a predefined size adapted to the hybrid system.
4. stores the image to a stack.

The point raster is scanned in a bidirectional manner, line by line.

A second program exports the data produced. The information is initially stored as 3D-matrix of intensity values in MATLAB. It also includes data preprocessing. Data are

1. corrected for the distortion caused by the fisheye objective lens;
2. converted to a stack of tiff-images;
3. exported to a preset folder for subsequent reconstruction.

2.3.6 Assembly

The FMT probe comprising the various components described was designed using Autodesk Inventor (Autodesk, San Rafael, USA), a CAD program (Fig. 2.28). The various parts were first drawn in 3D with Autodesk, from which 2D blueprints were prepared for the mechanical workshop. The FMT probe consists of a closable box, a lightweight arm and a linear guiding system (Fig. 2.29). The base of the probe comprised the optical components for scanning in transmission mode. It includes a pigtailed single-mode fiber linking the fiber from the illumination module to the GRIN lens used for collimation, a MEMS mirror for source scanning and a second mirror (Edmund optics, Barrington, USA) that deflects the beam vertically such that it hits the sample from below. The second mirror increases the distance between the sample and MEMS mirror, and therefore increases the scanning field of the latter, which has a limited scanning angle of 28°. For a FOV of 25mm the distance between MEMS mirror and sample plane should be approximately 50mm. The sample (mouse) is positioned on the sample platform,

which can be removed sideways in a drawer like fashion for easy sample preparation. It contains the radiofrequency surface coil including the tuning/matching network, a water heating for maintaining the body temperature, anesthesia supply as well as earbars for head fixation. Earbars and the anesthesia supply can be mounted at various positions on the sample platform to allow for optimal positioning. The light distribution at the surface of the sample is registered with the imaging module, comprising the image sensor and the printed circuit board for camera operation. The light-tight cylindrical FMT probe can be opened with two side doors (made with the 3D-printer) to maximize access for mouse handling to the user. The optical components used for reflection mode operation (GRIN lens, MEMS mirror) are mounted to the rear flange of the FMT probe and connected to a fiber-mating sleeve at the front flange using a pigtail single mode fiber. Care has been taken to avoid mechanical contact while maneuvering the sample platform. The front flange carries two fiber-mating sleeves (reflection and transmission mode operation) for connection to the fiber from the illumination module, the connector for the camera cable, the rod for filter switching as well as the entry ports for power cables and the water tubings for the thermoelectric cooling device. All tubings, fibers, and cables were mounted such that no stray light could enter the closed FMT probe.

The lightweight arm consists of Vetronite (Von Roll, Breitenbach, Switzerland), a glass-fiber reinforced epoxy composite, and has high mechanical strength, which is necessary due to a considerable torque acting on the long distance. The height of the arm is adjustable such that the probe fits into the MRI bore. The length of the FMT probe is also adjustable, which allows for precalibration of the coil into the isocenter of the MRI, which is necessary for a proper MRI signal.

The whole FMT probe is mounted using a linear guiding system (IGUS, Cologne, Germany) consisting of an aluminum carriage positioned on the mounted aluminum rail of the MRI scanner. In general, various MRI compatible plastic materials were used for the assembly and metallic parts are avoided, because of Eddy currents or, in the case of e.g. Nickel, iron and Cobalt, magnetic parts. Most of the screws used for the FMT insert are made of polyamide 6.6, some are made of brass (e.g. for fixation of the probe to the lightweight arm).

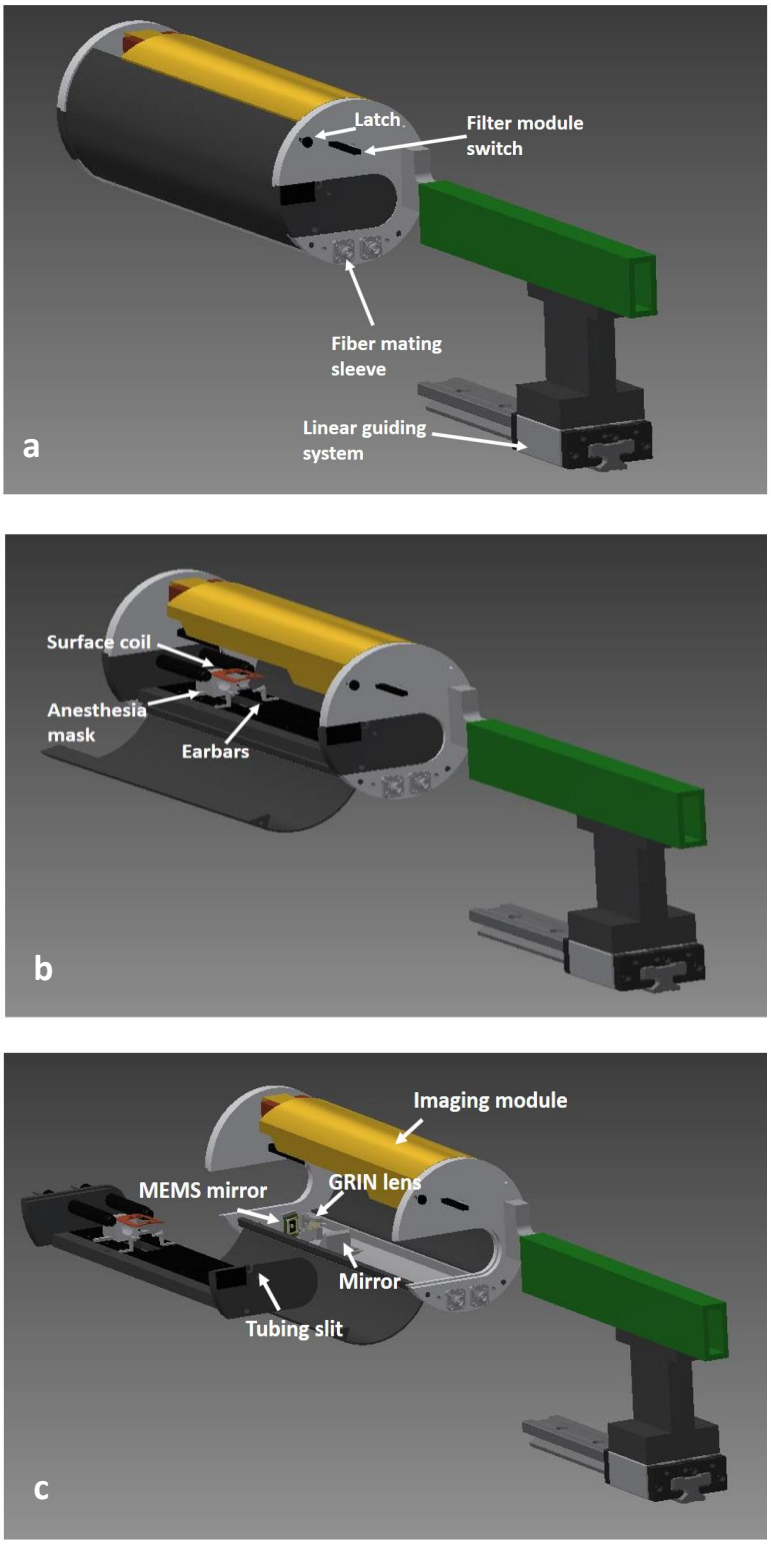

Fig. 2.28 FMT probe designed with Autodesk Inventor (CAD). (a) The closed FMT probe is fixed on the linear guiding system via the lightweight arm (green). Pulling the latch opens the box. The filter module switch serves for selection of the proper filter. The two fiber-mating sleeves are for connection of the illumination module in either reflection or transmission mode. (b) The side door is opened and gives access to the sample platform with the anesthesia mask, ear bars and the surface coil. (c) The sample platform can be removed for improved animal preparation. It contains a tubing slit for e.g. injection tubings required during experiments. The transmission chamber is visible on the image consisting of a single mode fiber (not visible), the GRIN lens, a MEMS mirror and a second mirror for vertical deflection of the laser beam.

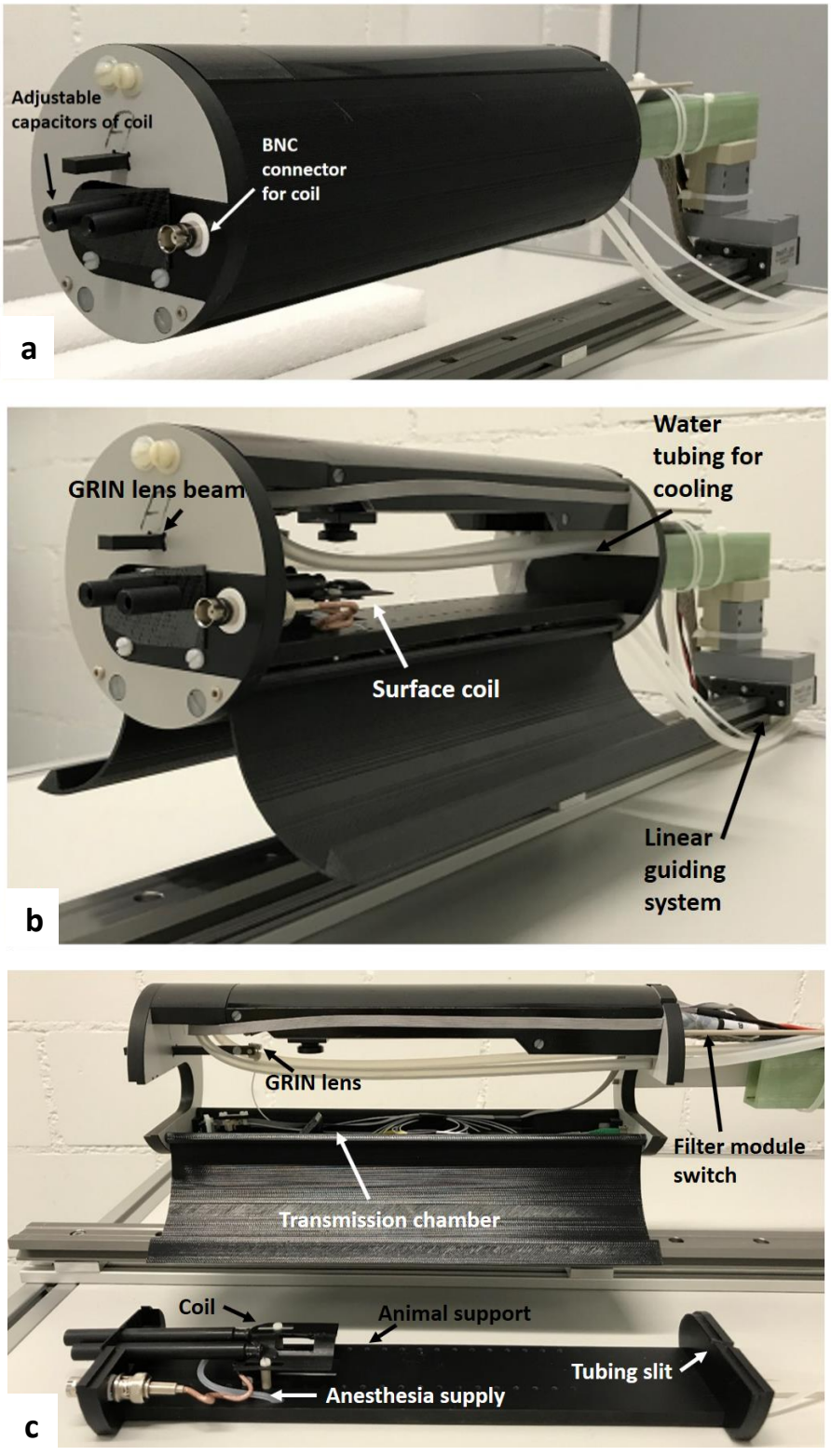

Fig. 2.29 FMT probe (a) closed box for safety and ambient light stop. The adjustable capacitors are adjusted with two long screwdriver-sticks from outside the MRI for tuning and matching. The surface coil is connected via the BNC connector to the MRI scanner. (b) Two side-doors opened giving access to the sample platform with surface coil. The water tubing serves for cooling of the thermoelectric cooler, which cools the sCMOS image sensor.The FMT probe is placed on the linear guiding system. The position of the reflection mode fiber output can be controlled at the GRIN lens beam. (c) Animal support removed for improved animal preparation. Also visible on the image are e.g. the fiber module switch, the transmission chamber and part of the anesthesia supply.

2.4 Conclusion

This chapter presents the development of the hybrid FMT-MRI system with a focus on the hybrid FMT-MRI 3.0 system. The FMT-MRI 1.0 system was a proof-of-principle showing the feasibility of doing FMT inside a MRI. This system was yet difficult to handle and showed poor overall-performance. The FMT-MRI 2.0 was designed to develop a hybrid FMT-MRI system for routine use. While this system showed clear improvements in both handling and performance, the calibration step required was still impractical. Based on the experience gained with the FMT-MRI 2.0 system, the FMT-MRI 3.0 is a remodeled version with the imaging and scanning module combined in a fixed frame, which considerably simplifies the handling procedure of the system. The FMT-MRI 3.0 system achieves another higher level at all points. The camera embracing a cutting-edge sCMOS sensor had to be adapted for optimal performance as part of the FMT-MRI 3.0. Modification are required to make the camera MRI compatible. A shielding box significantly reduces cross-talk with the MRI. As was found, reduction of electromagnetic interference requires a considerable effort in shielding due to the both very sensitive camera and MRI scanner involved. A cooling module significantly reduces the dark current and hereby increases the sensitivity. Cooling to a moderate temperature of 10° C shows a considerable increase in sensitivity. As was found with the FMT-MRI 2.0 cooling to even lower temperatures results in only minor improvement in sensitivity, yet is technically intricate due to required prevention of water condensation.

Replacement of the galvanometrically driven laser scanner by a MEMS mirror fitting inside the MRI scanner clearly improves handling. It involved a complete redesign of the illumination module. A compact design of the illumination module requires single-mode rather than multi-mode fiber for guiding the laser beam, which renders it more laborious to efficiently couple the laser into the fiber. However, single-mode fibers proved beneficial enabling a smaller and clean monomode laser spot.

1. SEMROCK. *660/13 nm BrightLine single-band bandpass filter*. [cited 2017 June 19th]; Available from: https://www.semrock.com/filterdetails.aspx?id=ff01-660/13-25.
2. Stuker, F., *Hybrid imaging: combining fluorescence molecular tomography with magnetic resonance imaging.* Diss. ETH No. 19664, 2011.
3. Milanovic, V. *Linearized gimbal-less two-axis MEMS mirrors*. Optical Fiber Communication Conference 2009; JThA19].
4. Holst, G., *sCMOS—Die eierlegende Wollmilchsau der Bildsensorik?* Optik & Photonik, 2009. **4**(3): p. 37-39.
5. Stuker, F., C. Baltes, K. Dikaiou, D. Vats, L. Carrara, E. Charbon, J. Ripoll, and M. Rudin, *Hybrid small animal imaging system combining magnetic resonance imaging with fluorescence tomography using single photon avalanche diode detectors.* IEEE transactions on medical imaging, 2011. **30**(6): p. 1265-1273.
6. Rose, A., *The sensitivity performance of the human eye on an absolute scale.* JOSA, 1948. **38**(2): p. 196-208.
7. Edelstein, W., G. Glover, C. Hardy, and R. Redington, *The intrinsic signal-to-noise ratio in NMR imaging.* Magnetic Resonance in medicine, 1986. **3**(4): p. 604-618.
8. Rudin, M., *Molecular imaging: basic principles and applications in biomedical research*. 2013: World Scientific.
9. Einstein, A., *Über einen die Erzeugung und Verwandlung des Lichtes betreffenden heuristischen Gesichtspunkt.* Annalen der physik, 1905. **322**(6): p. 132-148.
10. Peter, S. *Single Photon Imaging*. [cited 2017 June 3rd]; Available from: http://www.imagesensors.org/Past%20Workshops/2011%20Workshop/2011%20Papers/I04_Seitz_Singlephoton.pdf
11. ANDOR. *Scientific Digital Cameras*. [cited 2017 June 3rd]; Available from: http://www.andor.com/learning-academy/scientific-digital-cameras-fundamental-properties-of-a-digital-camera.
12. Holst, G., *Scientific CMOS camera technology: A breeding ground for new microscopy techniques.*
13. Association, E.M.V., *EMVA Standard 1288, standard for characterization of image sensors and cameras.* Release, 2010. **3**: p. 29.
14. Becker, H.N., M.D. Dolphic, D.O. Thorbourn, J.W. Alexander, and P.M. Salomon, *Commercial sensory survey radiation testing progress report*. 2008, Pasadena, CA: Jet Propulsion Laboratory, National Aeronautics and Space Administration, 2008.
15. Seitz, P. and A.J. Theuwissen, *Single-photon imaging*. Vol. 160. 2011: Springer Science & Business Media.
16. ANDOR. *CCD Signal to Noise Ratio*. [cited 2017 June 5th]; Available from: http://www.andor.com/learning-academy/ccd-signal-to-noise-ratio-calculating-the-snr-of-a-ccd
17. York, T., *Fundamentals of Image Sensor Performance.* jain/cse567-11/ftp/imgsens/index.html, 2011.
18. Alexander, H. *Noise in Image Sensors*. [cited 2017 July 7th]; Available from: https://www.eecs.tu-berlin.de/fileadmin/fg144/Courses/10WS/pdci/talks/noise_sensors.pdf.
19. FairchildImaging. *4.2 Megapixel Ultra Low Noise sCMOS Image Sensor*. 2014 [cited 2017 June 12th]; Available from: http://fairchildimaging.com/.
20. Oxywise. *What is the dew point and how do you calculate it?* [cited 2017 June 8th]; Available from: http://www.oxywise.com/en/tools/tool/what-is-the-dew-point-and-how-do-you-calculate-it
21. Gerhard, H. *Camera Tutorial - How to choose and use the right camera for a microscopy aplication - part I*. 2014 [cited 2017 June 8th]; Available from: https://www.pco-

tech.com/fileadmin/user_upload/pco-knowledge_base/20140412_FOM_CameraTutorial_PCO_fin_pdf.pdf
22. PCO. *pco.edge 4.2 - scientific CMOS camera*. [cited 2017 June 12th, 2017]; Available from: https://www.psi.ch/sls/tomcat/Station1_DetectorsEN/BR_pco_edge42_108_online.pdf
23. Schulz, R.B., V. Plantz, and D. Brush, *Shielding theory and practice.* IEEE Transactions on Electromagnetic Compatibility, 1988. **30**(3): p. 187-201.
24. Awareness, R.A.E. *Shielding of products*. Available from: http://www.emcia.org/awareness/Pages/MitigationTechniques/Design/ShieldingAreaVol.htm (Access date: June 12th, 2017).
25. Ankiewicz, A. and G.-D. Peng, *Generalized Gaussian approximation for single-mode fibers.* Journal of lightwave technology, 1992. **10**(1): p. 22-27.
26. Schneider, C.A., W.S. Rasband, and K.W. Eliceiri, *NIH Image to ImageJ: 25 years of image analysis.* Nature methods, 2012. **9**(7): p. 671.
27. Lammel, G., S. Schweizer, and P. Renaud, *Optical microscanners and microspectrometers using thermal bimorph actuators*. Vol. 14. 2013: Springer Science & Business Media.
28. Milanovic, V., G.A. Matus, and D.T. McCormick, *Gimbal-less monolithic silicon actuators for tip-tilt-piston micromirror applications.* IEEE journal of selected topics in quantum electronics, 2004. **10**(3): p. 462-471.

Chapter 3

Characterization of Hybrid FMT-MRI 3.0

Andreas Elmer, Mark Augath, Ramanil Keshini Sooriyaarachch Perera, Ruiqing Ni and Markus Rudin have contributed to this section.

3.1 Aims and Objectives

The focus in the development of the FMT-MRI 3.0 system was to improve handling, robustness and power of the system. A considerable achievement in these aspects was arranging scanning and imaging modules in a fixed frame eliminating tedious system calibration prior to each experiment. This involved many design changes such as the use of a MEMS laser scanner and optical fibers for transmittance of the laser beam. Another major change was the new imaging module featuring a novel low read noise sCMOS image sensor with the associated cooling module and the shielding camera box. The main focus of this chapter will be the characterization of these new devices, their interaction with the MRI scanner and the behavior of the system in its entirety.

The characterization comprised aspects such as the assessment of

- the beam profile on the sample surface both in reflection and transmission mode
- the accuracy and reproducibility of laser scanning on the sample surface both in reflection and transmission mode outside and inside of the MRI magnet
- the impact of MRI scanning on MEMS function
- the accuracy of image reconstruction using tissue mimicking phantoms with fluorescent inclusions.

Finally, the performance of the system was evaluated under in vivo conditions by imaging protease activity in a subcutaneous tumor model in mice using the protease activatable fluorescent reporter.

3.2 Material and Methods

3.2.1 Instrumentation

Experiments have been carried out using the homebuilt FMT system consisting of an illumination module and the FMT probe in combination with a 9.4/30 BioSpec MRI-scanner with a 9.4 T magnet with 30 cm clear bore (Bruker BioSpin GmbH, Ettlingen, Germany) (Fig. 3.1). The MRI system is equipped with a high performance gradient system of 114 mm inner bore diameter, capable of switching gradients up to 400 mT/m. The illumination module containing the laser source is located outside the scanner, while the FMT probe comprising imaging and two scanning modules as well as the radiofrequency surface coil is positioned at the magnet center.

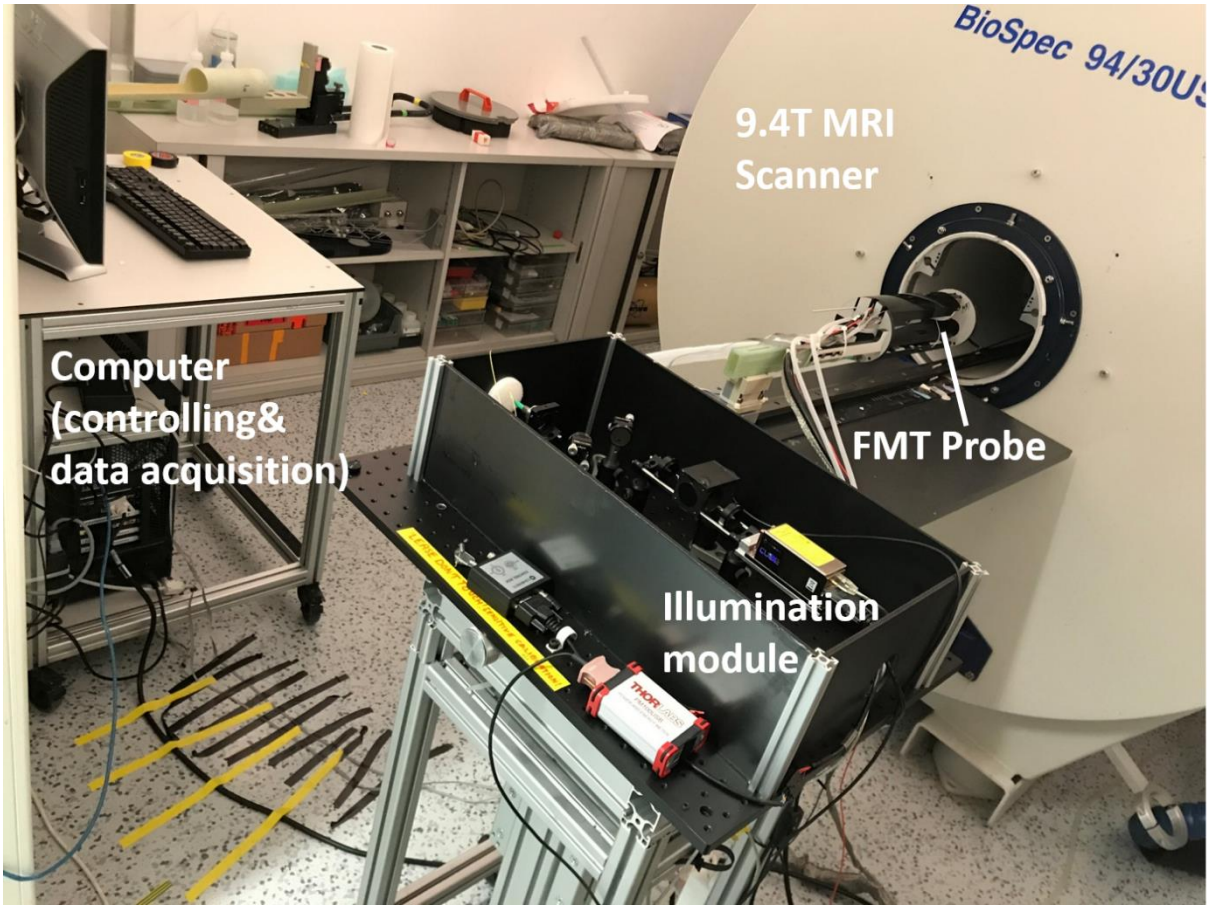

Fig. 3.1 Setup of the hybrid FMT-MRI system. The illumination module consists of a laser that is coupled into a single-mode fiber. The fiber guides the laser to the FMT probe. The FMT probe consists of an imaging module for fluorescence detection, two MEMS mirrors for scanning of the FMT source pattern (for both reflection and transmission mode), an MRI surface coil and a sample platform. A computer unit controls the FMT acquisition and reads the FMT data out.

3.2.1.1 Illumination Module

The illumination module comprises a diode laser (Coherent, Santa Clara, USA) emitting at 662nm. Two flat mirrors (Thorlabs, Newton, USA) and a fiber collimator (f=4-6 mm, Thorlabs, Newton, USA) couple the laser beam into a single-mode fiber (Thorlabs, Newton, USA) with a mode field diameter between 3.6 and 5.3 µm and NA=0.12. The fiber is connected to the FMT probe.

3.2.1.2 FMT Probe

The FMT probe comprises the on-board camera and the MEMS scanning devices as well as the radiofrequency surface coil in a fixed geometry. It is produced from non-magnetic materials to ascertain MRI-compatibility. The use of non-magnetic metallic parts was reduced to a minimum to avoid Eddy currents associated with the switching of magnetic field gradients. The FMT probe was connected via a lightweight arm with high mechanical strength to the carriage of a linear guide system. The arm consists of Vetronite (Von Roll AG, Breitenbach, Switzerland), a glass-fiber reinforced epoxy composite. The linear guide system (IGUS, Cologne, Germany) consists of an aluminum carriage and allows for reproducible and smooth positioning of the FMT probe. All screws used for the FMT insert were from either polyamide or brass.

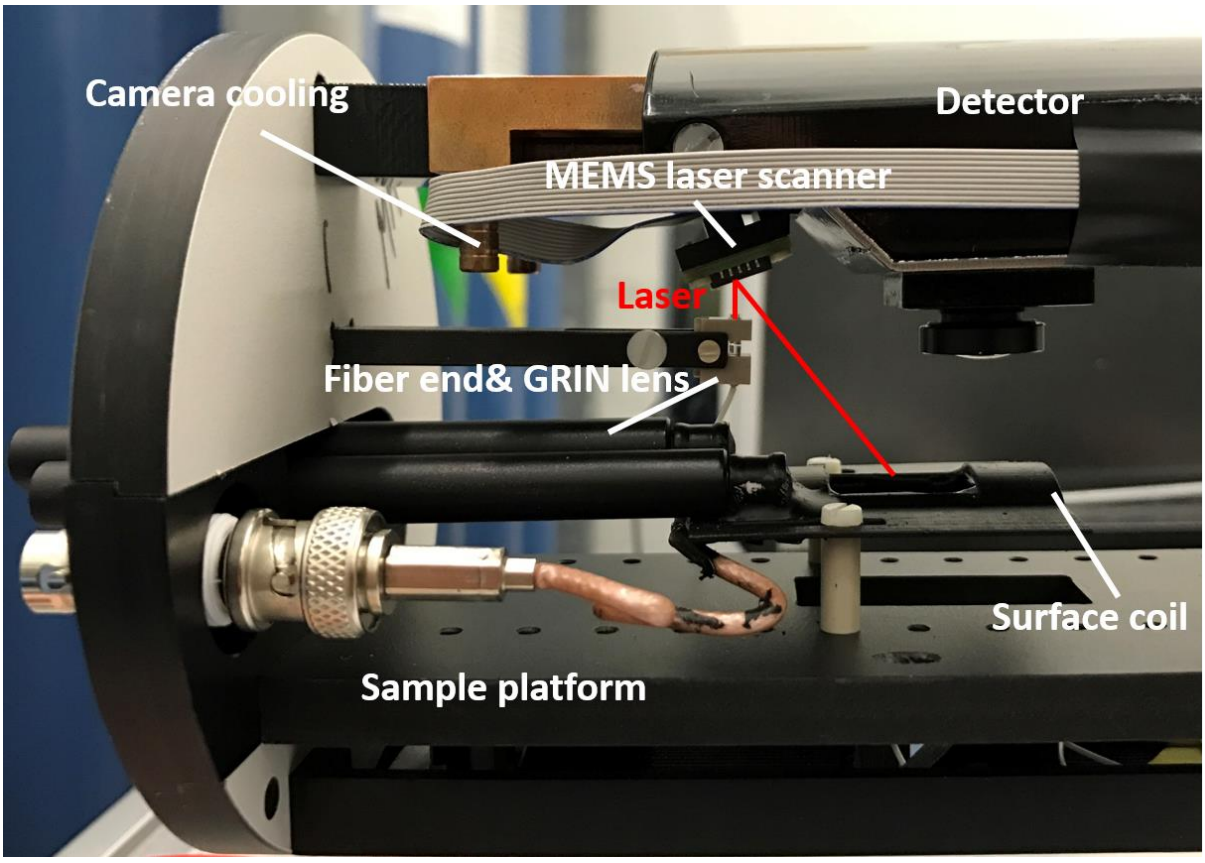

Fig. 3.2 Close up of the FMT probe. The MEMS laser scanner guides the laser through the hole of the surface coil and creates the source scanning pattern on the sample.

The laser light enters the FMT probe via FC/APC-connectors (reflection mode or transmission mode port), is then collimated using graded-index (GRIN) lenses (f= 1.85 mm and 0.23 pitch, Thorlabs, Newton, USA) and is then directed either to the reflection mode or the transmission mode MEMS mirror (Mirrocle Technologies, Richmond, USA) (Fig. 3.2).

A) Camera System

The light distribution at the sample surface is recorded using a board-level camera module (PCO AG, Kelheim, Germany) that comes with a sensitive sCMOS image sensor with a pixel resolution of 2560 x 2160 pixels, a readout noise level of 1 electron RMS and a peak quantum efficiency higher than 70 %. The image sensor was cooled to 10°C with a thermoelectric cooling device (Deltron AG, Kirchberg, Switzerland) to reduce dark current noise. A homebuilt copper block flushed with cold water (temperature 6 °C) removes heat from the thermoelectric cooling device. The camera was adapted to render it MRI compatible: magnetic parts were removed of the connector of the camera board, while magnetic screws were replaced by non-magnetic ones.

The camera printed circuit board was encased by a shielding box made from acrylonitrile butadiene styrene (ABS), and was produced with a 3D-printer. Shielding is achieved with a thin layer of aluminum (thickness 2.5 µm) produced by physical vapor deposition (Kaltbrunner AG, Grenchen, Schweiz). Additionally, amucor shielding gaskets (Holland Shielding Systems, Dordrecht, Netherlands) were used for shielding the gap of the top and bottom part of the box, while the power cable of the camera is shielded with cable shielding (Holland Shielding Systems, Dordrecht, Netherlands).

The camera was equipped with an anti-reflection coated fisheye objective lens (Marshall Electronics Inc, Torrance, California, USA) that collects light at a wide-angle of 155° to maximize the field-of-view. Distortion due to the lens were corrected using a distortion correction algorithm written in MATLAB (MathWorks, Natick, USA) using the Computer Vision System Toolbox. A filter module is positioned in-between the image sensor and the objective lens. It contains two single-band bandpass filters to image at both excitation (excitation filter with central wavelength: 660 nm, bandwidth: 20.2 nm) and fluorescence wavelength (fluorescence filter with central wavelength: 720 nm, bandwidth: 19.2 nm FWHM). Filters could be mechanically switched from outside the MRI magnet.

B) MEMS Devices

The MEMS mirror has a diameter of 3 mm and uses electrostatic actuation to scan an optical angle of +/-14° and a power consumption below 1 mW. The MEMS switching time to move the laser beam for grid point to grid point is fast and negligible compared to the integration time of the camera.

C) Radiofrequency Surface Coil

The curved coil has a rectangular window of 20 x16 mm^2 for collecting the fluorescent signals. It is made from a 0.3mm thick Cu foil and mounted on a slightly curved plastic former. It has two adjustable capacitors with capacitance between 1 and 10 pF for tuning and matching. Balanced coupling is done with two capacitors (Amercian Technical Ceramics, Huntington Station, USA) of 5.6 pF. And an additional capacitor (Amercian Technical Ceramics, Huntington Station, USA) is used to reduce voltage drops during RF transmit operation. More details are given in chapter 2.

3.2.2 Materials

3.2.2.1 Phantoms for Combined FMT-MRI Measurements

The tissue-mimicking phantom was of cuboid shape with dimensions 60 x 80 x 13 mm^3 and was made of a silicone polymer (Wacker, Munich, Germany). The scattering and absorption coefficient were adjusted by adding titanium oxide TiO_2 (Alfa Aesar, Karlsruhe, Germany) and carbon black (Alfa Aesar, Karlsruhe, Germany), respectively, to obtain similar values as in biological tissues. For the phantom production two silicone components (Elastosil RT 601 A+B, Wacker Chemie, Munich, Germany) were mixed, which initiates the solidification process. The mixture is poured into a mould and put under a

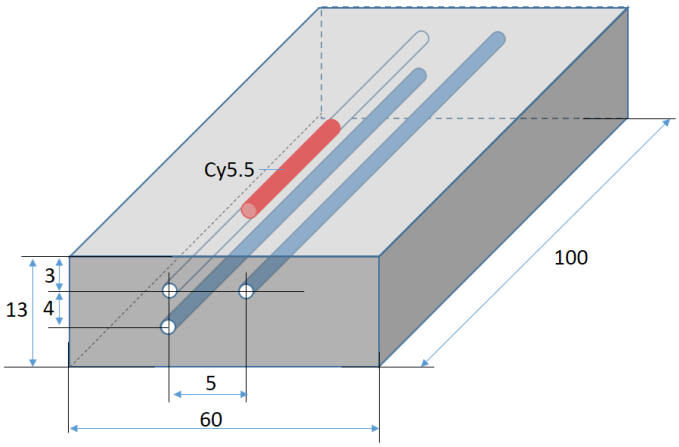

Fig. 3.3 Geometry of phantom and capillary tubes containing Cy5.5 and water for imaging with both MRI and FMT.

vacuum for bubble removal. The phantom solidified in 24 hours at room temperature. Two glass capillaries of 1 mm inner diameter filled with water were positioned parallel to the long axis of the cuboid at 3 mm and 7 mm depth inside the phantom. A third capillary was filled with the fluorescent indocyanine dye Cy5.5 to 45 % of its length positioned at a depth of 3mm (Fig. 3.3).

3.2.2.2 Animal Model

A C57Bl/6N mouse was injected with 10^5 B16-Venus-pH3SVT tumor cells (melanoma) in 30 µl of fetal bovine serum intradermally in the flank. The B16-Venus-pH3SVT cells stably express the fluorescent protein venus (excitation maximum: 515 nm, fluorescence maximum: 528 nm) in the nucleus constitutively while expression of Turbo-FP635 (excitation maximum: 588 nm, fluorescence maximum: 635 nm) is regulated by tissue oxygen levels. The mouse was measured 35 days following tumor inoculation. At this time point, the subcutaneous tumor has reached a diameter of 10 mm.

For FMT-MRI measurements the mouse was anesthetized with isoflurane and the support was heated with warm water to support the mouse in keeping its body temperature.

3.2.2.3 Fluorescent Agent

The Near-Infrared fluorescent cyanine dye Cy5.5 has its absorption and emission peak at 675 nm and 694 nm, respectively [1] and was used with a concentration of 1mM. An amount of 40 µl was inserted into a glass capillary tube and placed inside the phantom. The protease activity probe ProSense680 (Perkin Elmer, Waltham, Massachusetts, USA) was prepared as suggested by the manufacturer: a single dose of 20 nmoles was diluted in saline to yield a total amount of 150 µl [2] for intravenous injection into the tail vein of the mouse. The FMT measurement was carried out 24 hours after the injection.

3.2.2.4 FMT Reconstruction

Using the diffusion equation and considering the FMT sources as point sources on the phantom surface, the forward model consisted in calculating the distribution of the excitation light throughout the phantom. The inverse model, an ill-posed problem, was used to calculate the fluorescence dye distribution using the normalized Born approximation involving the ratio of emission and excitation FMT data [3]. The inversion of the matrix was done using the conjugate gradient method [4]. Since the diffusion equation can only be analytically solved for few geometries (cylinder and slab), small meshes were formed using finite element method to iteratively solve the diffusion equation numerically and therefore calculate the diffusive propagation of light inside the phantom.

The coregistration of the FMT and MRI image were done using the following information:

1. The middle sagittal plane of both the MR data and the FMT data coincide. This was assumed, because the FMT sources were symmetrically scanned around the middle axis of the MR surface coil through its window.
2. The phantom surface can be detected on the MR image and can be matched with the phantom surface of the FMT reconstruction data.

3.2.3 Experimental Paradigm

3.2.3.1 Fluorescence Data Acquisition

The samples (mouse or phantom) were placed on the animal support under the surface coil. The phantom was imaged in both reflection (laser coming from top) and transmission mode (laser coming from bottom), whereas the mouse was imaged only in reflection mode. In reflection mode the source grid consisted of 7x12 points in all cases, and in the transmission mode of 5x9 points. The reduced number of points in transmission mode, resulting in a shorter readout time, was chosen to balance the longer integration time that had to be chosen due to the intrinsically weaker signal. The integration time for a single image was chosen to exploit the full dynamic range of the sensor yet to avoid saturation in any of the pixels. For integration time optimization the camera application software (PCO, Kelheim, Germany) had been used.

FMT experiments were controlled using a MATLAB program, which uses the values for the integration time and the number of irradiation points of the source grid as input parameters. The program controls the MEMS operation and the recording of an image of the surface light distribution for each source location (start and stop signal for sensor readout). The product of integration time and number of source points approximately gives the acquisition time for one image series. Image series are recorded both for the excitation mode and, after switching the filter, for the emission mode. In addition, a background and a white light image are recorded. Correction of image distortion, data export and conversion of image series into 'image stacks' are based on MATLAB programs.

3.2.3.2 Assessing the Reproducibility of Laser Scanning Across the Sample

The reproducibility of the excitation patterns on the sample surface was studied using the MEMS mirror for the FMT transmission mode configuration. The laser beam was projected on white paper to allow for an accurate assessment of the beam position following deflection by the MEMS mirror. 5x9 source points were scanned in each round and the procedure was repeated 8 times for each condition.

Experiments were carried out both outside and inside of the MRI magnet. With the FMT probe in the magnet we compared the performance both with and without running MRI acquisition sequences simultaneously.

Analysis: Images were processed using a MATLAB program. In a first step a maximum intensity projection was carried out transforming the 3D stack into a 2D image. In a second step, this image was converted into a binary image based on intensity thresholding. For each pixel cluster with value 1 and each repetition the centroid was calculated defining the coordinate point of the laser position. The standard deviations in x- and y-direction were calculated for each position for the 8 measurements.

3.2.3.3 MRI Data Acquisition

MRI experiments were conducted on a small animal 9.4T MRI-Scanner (Biospec 94/30, Bruker, Billerica, USA) equipped with a gradient system with 114 mm inner diameter capable of switching gradients of up to 400 mT/m in less than 100 µs. A homebuilt RF transceiver surface coil was used for excitation and receiving of the MR signal (see above). Various pulse sequences involving different duty cycles for the gradient system and different levels of radiofrequency power deposition have been evaluated. These comprise TurboRARE [5], FLASH [6] and EPI [7]. For phantom and mouse studies the FLASH sequence has been used. The sequence parameters for the individual experiments are summarized in Table 3.1.

SEQUENCE	TE/TR [ms]	Matrix	FOV [mm^2]	nslices	Additional comment
	MEMS mirror repeatability				
TurboRARE	11/2000	256x256	40x40	9	RARE-Factor=8
FLASH	2.51/12.5	110x110	22x22	1	Flip angle=7°
EPI	0.64/1500	192x192	40x40	1	
	Phantom				
FLASH	2.51/500	256x256	25.6x25.6	30	NAverage=1
	Mouse				
FLASH	2.51/500	256x256	25.6x25.6	40	NAverage=1

Table 3.1 MRI parameters for MEMS mirror repeatability, phantom and mouse readout.

3.3 Results

3.3.1 Laser Power Loss Along Optic Transmission and Laser Beam Quality

The laser beam was found to be of good quality as shown in chapter 2 and showed a FWHM of 0.22 mm. The laser power was 100 mW at the laser output. It was reduced to 20 mW after passing the first fiber. The first fiber is connected to the second one using a FC/APC mating sleeve connector. At the end of the second fiber there is a GRIN lens, where the collimated laser beam exits. The laser was reduced to 3.1 mW in transmission mode and 1.4mW in reflection mode.

3.3.2 Reproducibility of Source Grid Scanning, Effect of Static and Time-Variant Magnetic Fields

The accuracy of the source point grid on the sample surface, i.e. the performance of the MEMS mirror based scanning, was tested both outside and inside the MRI magnet and with and without simultaneous MRI sequences running. A flat sheet of paper was positioned in the focal plane of the camera.

Different sizes of source pattern raster have been used for excitation and transmission mode due to physical constraints imposed by the FMT probe. The maximum field-of-view accessible in transmission mode was 15 x 26 mm^2 and limited by the window in the animal support, while the corresponding value in reflection mode was 20 x 16 mm^2 limited by the window of the radiofrequency coil. As described in the method section, reproducibility experiments have been carried out using the transmission-mode MEMS and 9 x 5 grid points nominally separated by 2.5 mm in the y- and by 2 mm in the x-direction. The scanning of the sources was highly reproducible both inside and outside the MRI when no MRI sequence was running (Fig. 3.5). Outside the MRI magnet the average standard deviation of the position was found to be 0.011 mm in x- and 0.026 mm in y-direction. These values remained essentially unchanged when positioning the FMT probe in the static magnetic field of 9.4 T: standard deviation along the x-direction was measured as 0.011 mm and along the y-direction as 0.023 mm. Interestingly, there was an average shift of 0.6mm between corresponding points scanned inside and the corresponding points scanned outside the MRI. This is probably due to a small mechanical deformation of the FMT probe, when inserted into the MR scanner. However, this shift is relatively small and is not expected to cause any consequences.

When the MEMS mirrors were operated during MRI scanning, the source grid became massively distorted as illustrated for a TurboRARE and an EPI sequence (Fig. 3.5). While occasional distortions were relatively small, as observed in some of the TurboRARE data acquisition (for the first four acquisitions, Fig. 3.5d), massive distortions with some points completely dislocated were observed at other incidences (last four acquisitions; Fig. 3.5e), with no clearly recognizable grid. There appears to be a strong interference between the transient magnetic fields associated with gradient-switching and MEMS operation. This became even more obvious when running EPI or FLASH sequences, which both are characterized by heavy gradient duty cycles. In these cases, points were severely dislocated and there was no association with the designed grid whatsoever.

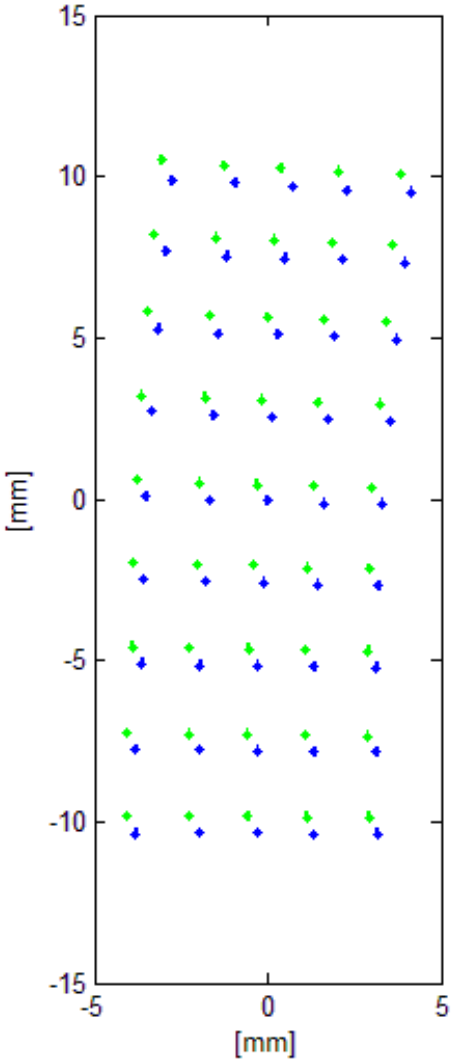

Fig. 3.4 Assessment of reproducibility of MEMS operation: Overlay of average point positions during source raster scan inside idle MRI (blue) and outside MRI (green). Standard deviation in x and y direction is shown as well, but is too small to be visible on graph. Interestingly, grid points measured inside and outside of the magnet were slightly shifted by o.2mm in the x- and 0.4mm in the y-direction.

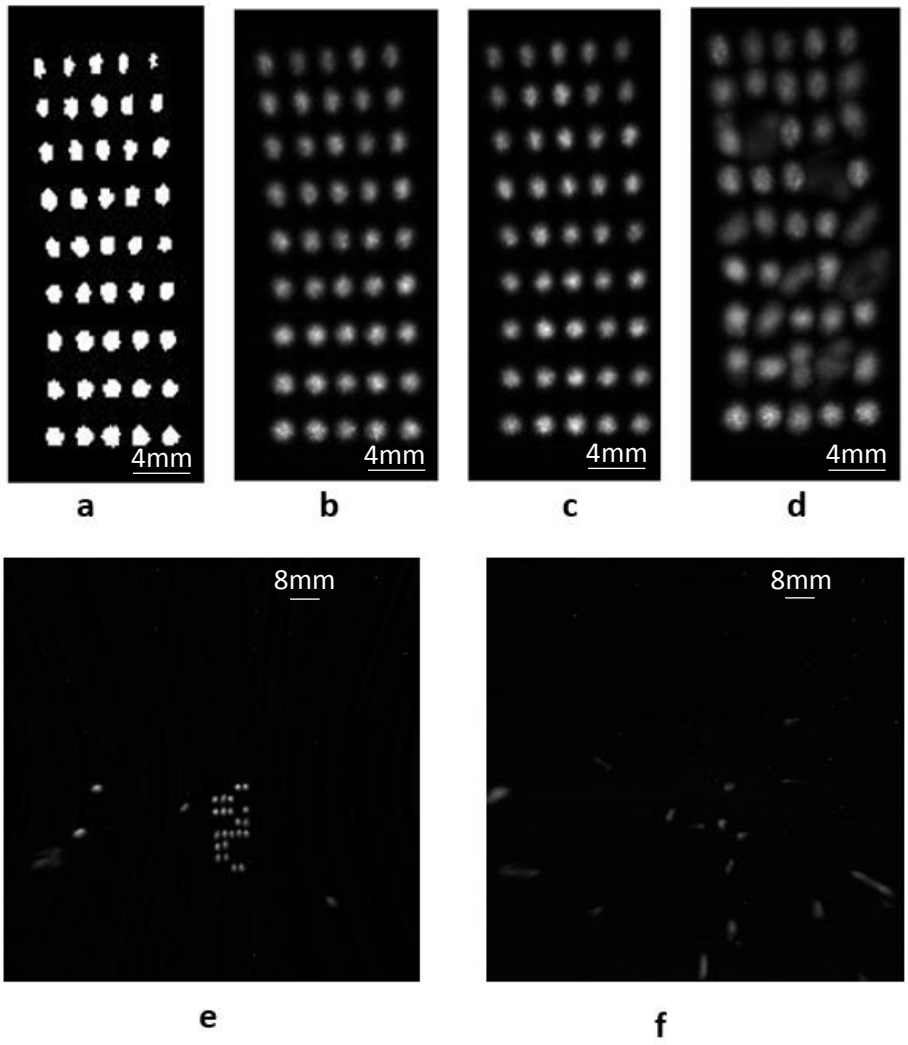

Fig. 3.5 Assessment of reproducibility of MEMS operation by analyzing source scanning patterns. (a) For quantitative analysis source grid patterns were transformed to binary images using intensity thresholding. In a second step the centroid of each binary cluster was determined. Source scanning pattern obtained from transmission mode MEMS mirror recorded outside (b) and inside the idle MRI (c), at the beginning (d) and end of a TurboRARE sequence (e) and an EPI sequence (f).

3.3.3 Characterization of FMT-MRI 3.0 Using Tissue Mimicking Phantom

The phantom made from silicon with absorption and scattering properties mimicking biological tissue and containing two glass capillary tubes filled with water (at 3mm and 7mm depth) and one filled with the fluorescent dye Cy5.5 (at 3mm depth) was imaged with the FMT-MRI 3.0 system generating MRI and FMT data with FMT both in reflection and transmission mode.

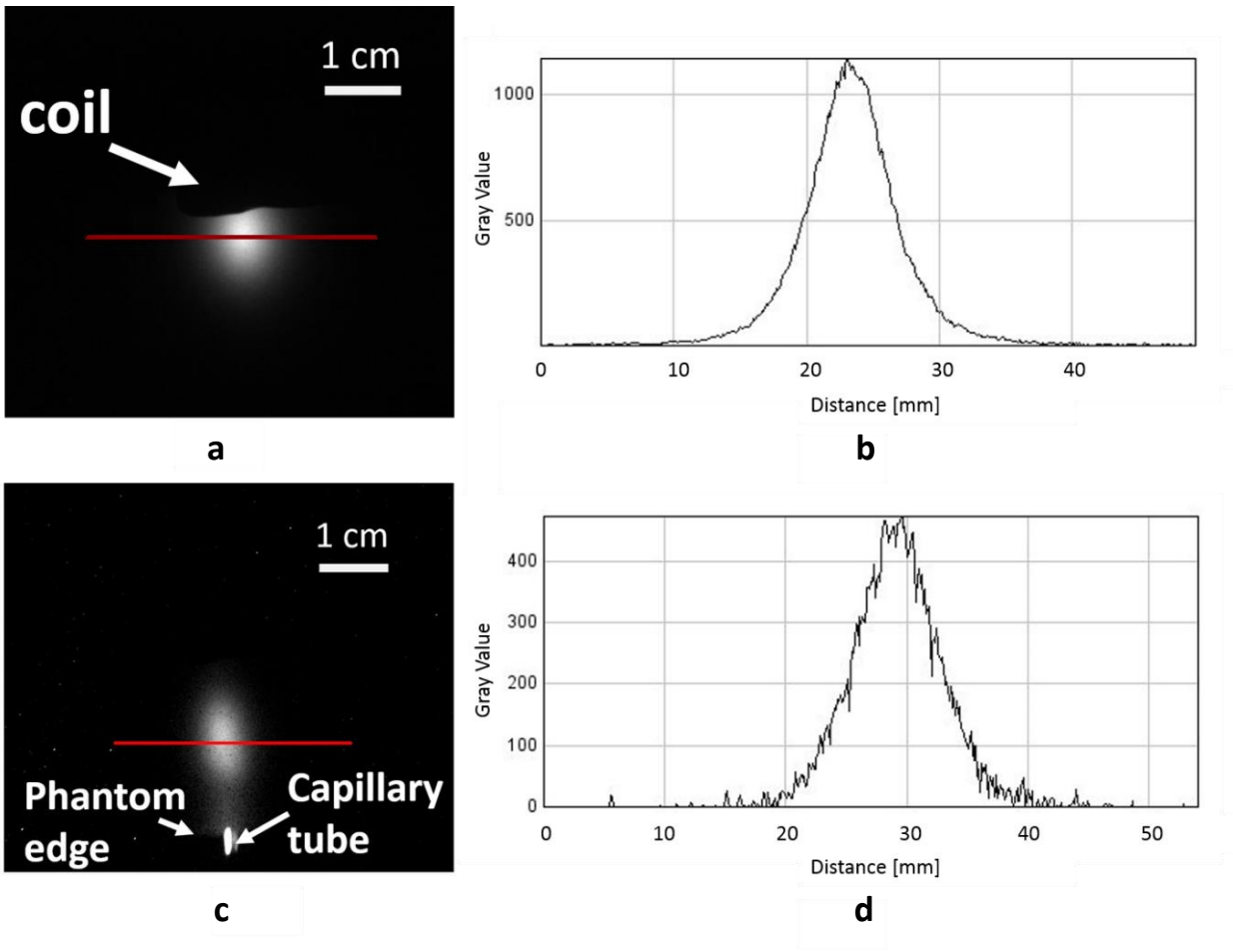

Fig. 3.6 Fluorescence intensity distribution at surface of tissue mimicking phantom imaged in reflection mode (a) and in transmission mode (c) with the coil edge producing a shadow of the signal on the former and a bright spot from the bare end of the glass capillary tube at the edge of the phantom on the latter. (b) and (d) Profile showing the signal distribution on the red line on a FMT raw data picture with strong fluorescence for reflection mode and transmission mode, respectively. The coil edge produces a shadow of the signal.

The FMT sensitivity was evaluated by calculating the SNR for an intensity profile of the fluorescence signal at the sample surface for the irradiation point yielding the strongest fluorescence intensity. The SNR was obtained by dividing the peak value of this curve by the standard-deviation of the noise recorded towards the edge of the image (red line, Fig. 3.6). The laser power and exposure time are given in Table 3.2. In reflection mode the laser power had to be considerably attenuated with neutral

density filters and the exposure time was chosen to be minimal with 1 ms to avoid saturation of the signal. In transmission mode, the laser power was maximal with 3 mW and the exposure time is half of the maximum value (4 s). In reflection mode the SNR was found to be SNR=303 while, not surprisingly, the transmission mode SNR value was significantly smaller, i.e. SNR=33 (Fig. 3.6). Nevertheless, we concluded that SNR and hence sensitivity for imaging a phantom of 13 mm thickness with a glass capillary tube at 3mm depth in transmission mode is sufficient to allow for FMT reconstruction.

	Laser power	Exposure time
	Reflection mode	
Excitation scheme	49 nW	1 ms
Emission scheme	390 nW	15 ms
	Transmission mode	
Excitation scheme	3 mW	4 ms
Emission scheme	3 mW	2000 ms

Table 3.2 Laser power and detector exposure time for the FMT phantom readout.

Figure 3.7 a,b shows MRI images of the tissue mimicking phantom as a transverse cross-section (left) and as a 3D rendered image (right). The three capillaries filled with either water or aqueous Cy5.5 solution are clearly discernible in the transverse cross-sectional image. The signal intensity of the structure most distant from the surface displays weaker intensity due to the B1-field distribution of the surface coil. In the 3D-rendered image, the Cy5.5 filled capillary is readily recognized due to the reduced length taken by the aqueous solution.

An overlay of a white light image (taken without filter) and the z-projection of the fluorescence data obtained as the maximum intensity values of all images of FMT fluorescence raw data stack (one image for each laser illumination point) is shown in Fig. 3.7c and Fig. 3.7d for reflection and transmission mode, respectively, again demonstrating the superior sensitivity of reflection mode imaging. The information obtained of the image in reflection mode corresponds closely to what is obtained in fluorescence reflectance imaging (FRI). Figures 3.7e,f finally show the superposition of z-projection

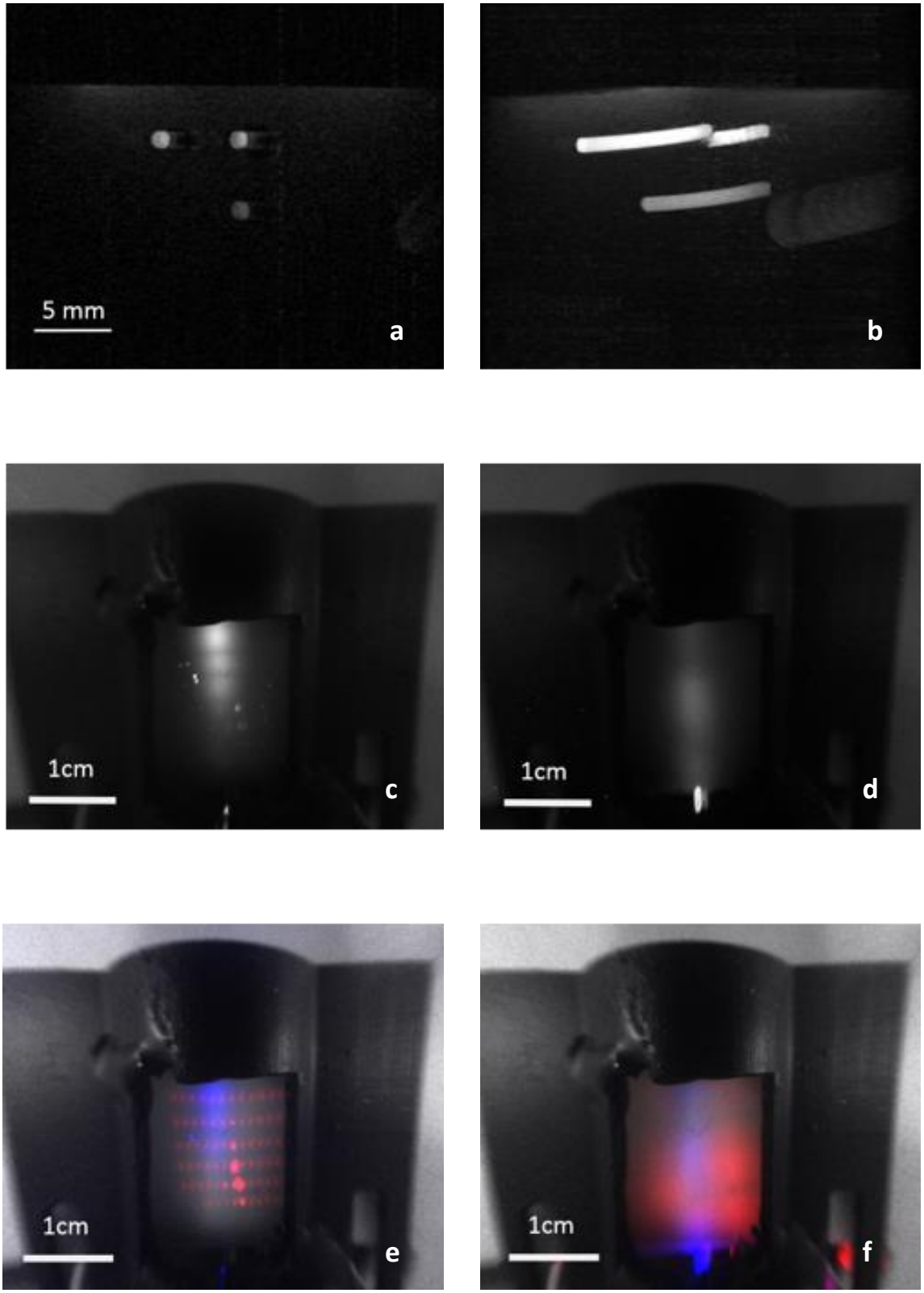

Fig. 3.7 Phantom (a) single slice MR readout (b) 3D rendering using maximum intensity projection and interpolation. Overlay of white light image and z-projection of only emission scheme (Fluorescence Molecular Tomography raw data) in both reflection (c) and emission mode (d). Overlay of whitelight image with z-projection of both excitation (red) and emission (blue) scheme in both reflection (e) and transmission mode (f).

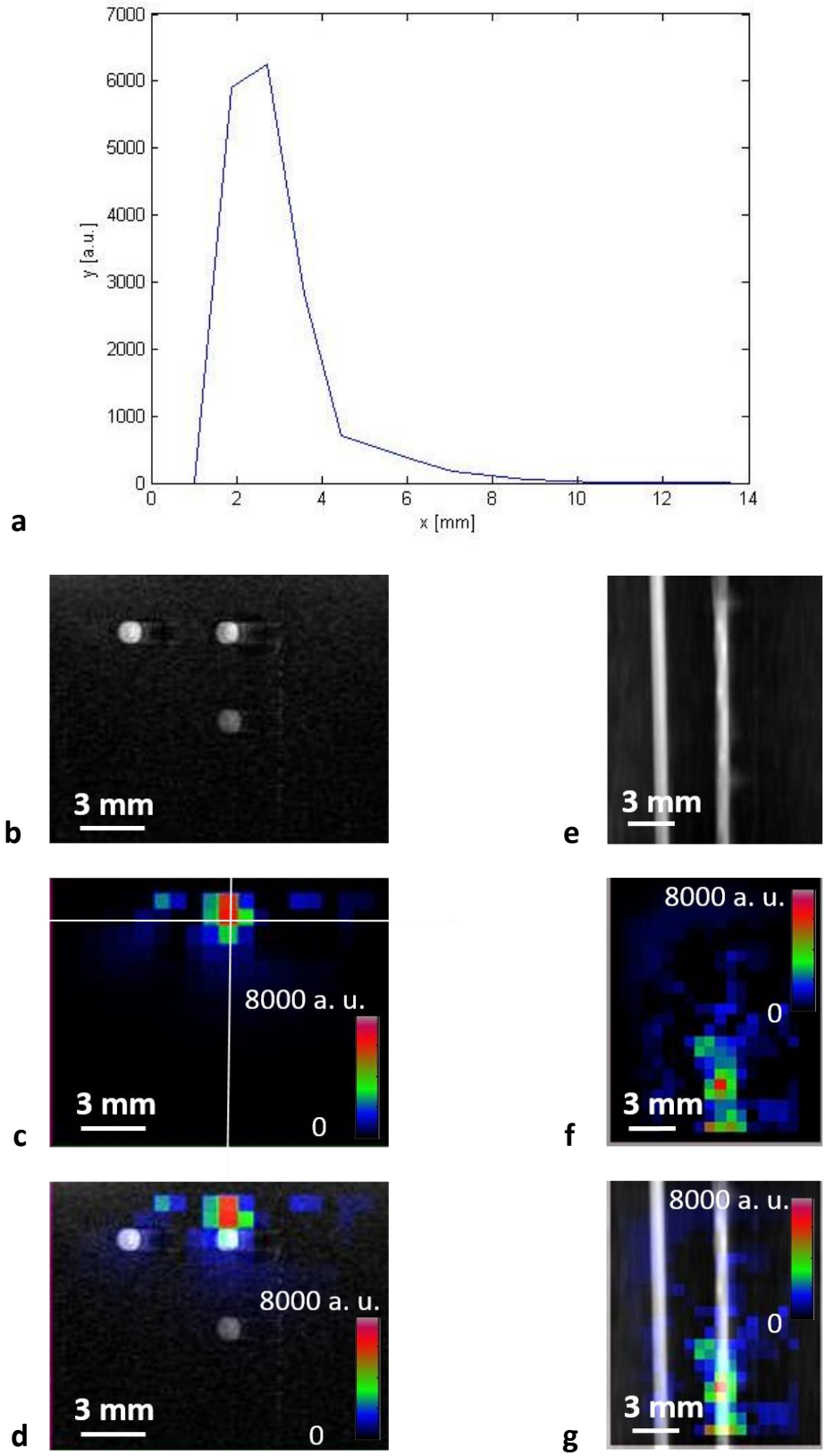

Fig. 3.8 FMT reconstruction in reflection mode of phantom (a) fluorescence signal [a. u.] in function of depth from the phatom surface obtained with FMT reconstruction located at the middle of the phantom (vertical line in (c)). MR image of the phantom in (b) axial and (e) coronal view. FMT image in axial (c) and (f) and coronal view. The horizontal lines indicate the positon of the cut for the corresponding perpendicular view. (d) and (g) Overlay of the MR and FMT image in both views. The FMT reconstruction was kindly provided by Wuwei Ren.

images for both reflection (e) and transmission (f) mode displaying both the excitation (red) and emission (fluorescence, blue) signals.

The fluorescence raw data imaged in reflection mode was used for FMT reconstruction and the FMT images were overlayed with corresponding MR images (Fig. 3.8).

3.3.4 Hybrid FMT-MRI Imaging of Tumor Bearing Mouse

To demonstrate proof-of principle of hybrid imaging under in vivo conditions a mouse with a B16 melanoma xenograft implanted in the left flank was imaged.

Tumors in general exhibit high levels of proteolytic activity, which can be exploited for using protease activatable probes [8]. ProSense680 is a representative of this class of fluorescent dyes that non-specifically indicates protease activity, and thus constitutes an attractive probe to assess the performance of the FMT-MRI 3.0 system. ProSense680 was injected into the tail vein of a mouse prior to the measurement. MR and reflection mode FMT data of the tumor were recorded before and after injection of ProSense680.

At the time point of imaging the tumor had a dimension of 10 x 8 x 7 mm^3 (Fig. 3.9a,b) as derived from MR images obtained using a multi-slice gradient echo sequence (FLASH). The tumor displayed a high degree of heterogeneity and vascularization. The vascular system displayed increased signal intensity as compared to the surrounding tissue due to inflow enhancement. A Cy5.5 filled glass-capillary was used as a signal reference on the one hand and for image registration on the other hand.

Fluorescence z-projection image stacks were also recorded prior and after dye administration. The SNR was estimated by taking the mean of the fluorescence signal in the tumor region and divided by the standard deviation outside the ROI. The tumor region was defined on the whitelight image, where the tumor contour was clearly detectable. This ROI was exported to the image containing the fluorescence data. ImageJ was used to calculate the total signal in this ROI. A signal-to-noise-ratio of SNR=7.6 was obtained for the fluorescence signal before ProSense680 injection and SNR=30 afterwards (Fig. 3.10). The exposure time was doubled for the post injection image and a third of the laser power had been used to avoid photo bleaching. If we assume SNR approximatively proportional to the laser power and to the square root of the exposure time, we estimate a 9-fold increase in fluorescence intensity following ProSense680 administration.

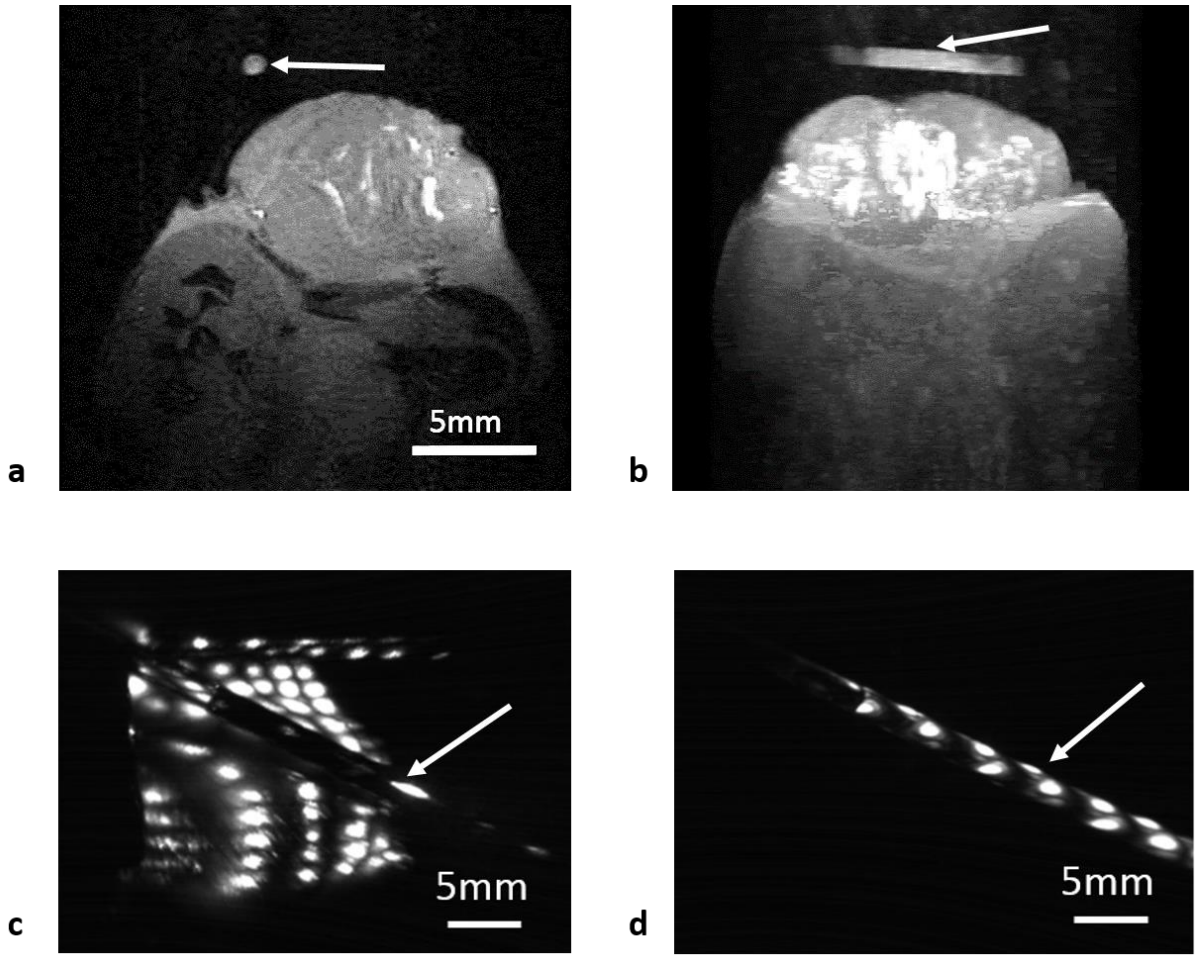

Fig. 3.9 Hybrid imaging of the melanoma xenograft together with a Cy5.5 filled glass capillary tube. (a) MRI section of tumor and glass capillary tube (b) 3D rendering using maximum intensity projection and interpolation. Z-projection of FMT excitation (c) and emission (d) scheme. White arrow indicates position of glass capillary tube.

	Laser power	Exposure time
Before ProSense680 injection		
Excitation scheme	140 nW	2 ms
Emission scheme	1 mW	2 ms
After ProSense680 injection		
Excitation scheme	140 nW	5 ms
Emission scheme	0.3 mW	4ms

Table 3.3 Laser power and detector exposure time for FMT readout with melanoma xenograft before and after ProSense680 injection.

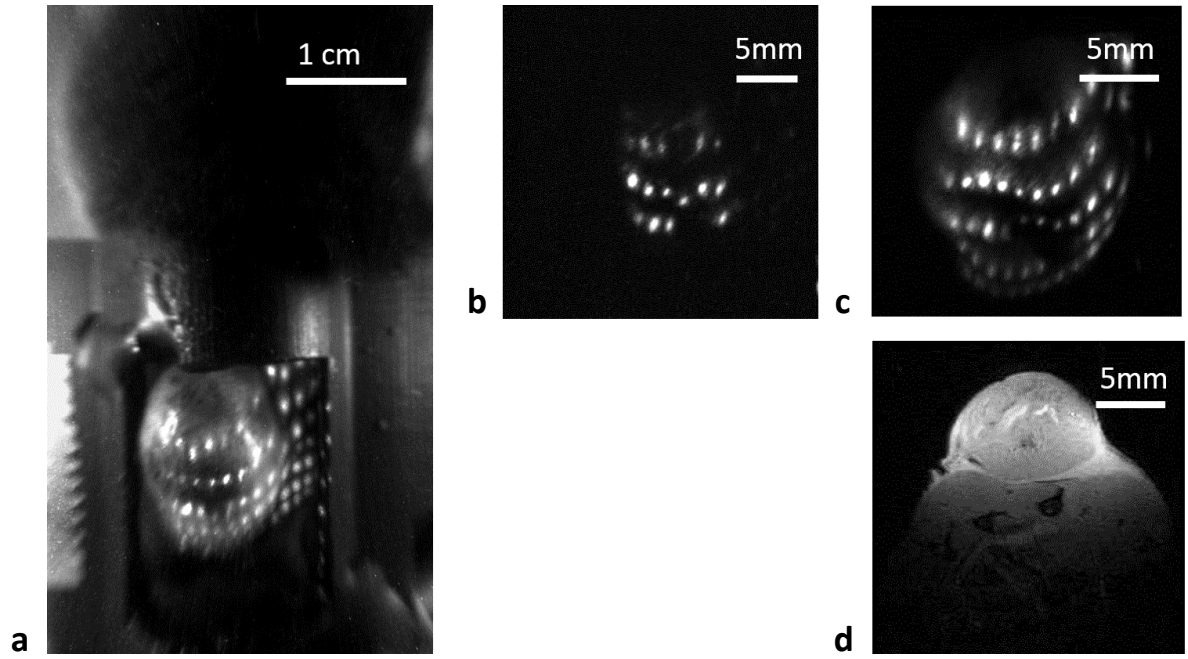

Fig. 3.10 Hybrid imaging with melanoma xenograft. (a) Overlay of excitation scheme and the white light image showing the source scanning pattern. Z-projection of FMT raw data (b) before and (c) after ProSense680 injection. (d) MRI slice of melanoma xenograft in the flank.

3.4 Discussion

The compact design of the FMT-MRI 3.0 hybrid imaging system, and in particular the fact that all optical components are intrinsically aligned as they are mounted in a fixed frame significantly facilitates operations. Once the mouse is anaesthetized and positioned on the support, the system is ready for measurement. The new design involved the use of novel components, notably the GRIN lenses for collimating the laser beam as it exits the optic fiber, the MEMS mirrors for scanning the laser beam across the sample, and a novel imaging device comprising a sCMOS sensor. Characterizing the performance of these components when exposed to static and dynamic magnetic fields as well as radiofrequency field is of critical importance. Aspects that had to be assessed are power losses due to the transmission via the single mode fiber and coupling to the GRIN lens, the quality of the beam profile at the focal plane, the accuracy and reproducibility of the MEMS mirror scanning, as well as the sensitivity of the detection system.

3.4.1 Beam Quality and Power Transmission

In chapter 2, the laser beam quality was characterized and an FWHM of 220 µm was found for the laser profile. Such a small diameter is preferred [9], since the FMT source is modelled as a point source in the FMT reconstruction.

In Fig. 3.5a-c a variance of beam shapes can be observed in the source scanning pattern. This variance can be explained by the inhomogeneous structure of the paper used to visualize the laser beam in the MEMS mirror repeatability experiment. The intensity change throughout the source scanning pattern is likely due to the change in the angle of incidence of the laser beam as well as the angular dependence of light scattering at the paper surface. In Fig. 3.7d, a different intensity change pattern of the source scanning pattern can be observed, which can be explained by the slightly specular surface of the phantom surface. The laser hits the surface at +/- 14°. Effects of angulation on the intensity or the beam profile can be neglected for the FMT system for such a small angle.

The laser at the input of the fiber had a power of 100 mW. At the output of the GRIN lens it was reduced to 3.1 mW in transmission mode and 1.4 mW in reflection mode. This is quite a severe loss of power, but for the experiments carried out within the scope of this thesis the power was clearly sufficient. However, for future experiments, where sensitivity is critical, much stronger laser power would be desirable. This can be readily corrected for by replacing the currently installed laser with a much stronger device.

3.4.2 Accuracy and Reproducibility of MEMS Mirror Scanning

In a standard FMT protocol the source scanning pattern is scanned twice, both during recording of the excitation scheme and the emission scheme. The fluorescence signal during the emission scheme is recorded in function of the source position determined previously with the excitation scheme. For accurate FMT reconstruction it is therefore crucial that the position of the sources coincide in both scanning sessions (excitation and emission) [3]. In order to achieve this the laser scanners i.e. the MEMS mirrors require good accuracy and reproducibility. Of course, under in vivo condition when using freely breathing mice there is some uncertainty concerning the laser position on the body surface due to respiratory motion. This might be accounted for by synchronizing data acquisition with respiration, but was not further considered in the current study.

The MEMS mirrors in our device performed in a highly reproducible manner both outside and inside the MRI magnet provided there was no actual MRI data acquisition ongoing. During repetitive scans the standard deviation between the centroids of intensity distribution was less than 0.03mm in both directions (x and y). This is much smaller than the half-width of the laser beam itself and the typical spatial resolution associated with FMT (1-2 mm). Hence, we may conclude that the presence of a strong static magnetic field (9.4 T) does not impair the proper functioning of the MEMS mirrors. Nevertheless, when comparing measures in and outside of the magnet we found a constant shift in grid points, by 0.2mm in x- and 0.4mm in y-direction. The reason might be a slight mechanic change of the setup upon positioning of the FMT insert in the magnet. This did, however not affect the reproducibility of the scanning.

MEMS scanning was severely compromised during MRI data acquisition. During an MRI sequence gradient coils are rapidly switched on and off and the RF-coil emits radio waves. The gradient coil switching may lead to three effects: The Lorentz force scaling with the current and magnetic field applied, electromagnetic interference due to induction caused by time-dependent magnetic field or oscillations of the FMT probe due to gradient-induced mechanical vibrations. Additionally, the radio wave emitted by the RF-coil may induce a current if structures of the MEMS mirror act as antenna.

The structures of the MEMS mirror are much smaller than the wavelength of the electromagnetic wave emitted by the RF-coil at 400 MHz, i.e. λ=75cm, therefore it is unlikely that they act as antenna. Additionally, it appears that degradation scales with the gradient duty cycle as sequence characterized by high duty cycles such as EPI and FLASH display stronger deviation from any regular grid. This clearly favors the gradient coils as cause for the oscillations.

The MEMS mirror has a comb-drive-based actuation. The fingers of the two combs form a capacitance and therefore get electrostatically charged [10]. This causes the opposing fingers to attract each other due to the Coulomb force, which creates the actuation of the mirror. Therefore, an alternating Lorentz force on the MEMS mirror originating from the synchronous switching of the gradient magnetic field is also an unlikely cause. Only a minimal current is flowing through the capacitive MEMS fingers occurring when they are electrically charged. Additionally, a Lorentz force at comparable amplitude would act in absence of gradient switching caused by both the current switching for MEMS mirror actuation and the much stronger static magnetic field of the MRI. This was however not observed.

There are no closed circuit loops in the MEMS mirror chip, which precludes electromagnetic induction in the MEMS circuit as the source of the artifacts. An ultra-thin metallic film ring is deposited on the frame of the MEMS and an influence on the oscillations cannot be 100% excluded, but seems also unlikely.

Hence, mechanical oscillations appear to be the most likely source for the mis-location of illumination points. The MRI gradient coils rapidly switch the magnetic field during an MRI sequence and the mutual forces exerted by the magnetic field cause the gradient coil to oscillate. This oscillation may be mechanically transferred to the rail of the MRI scanner and thereby to the FMT probe. Mechanical oscillation is also apparent in MR images, which show motion artefact (Fig. 3.11).

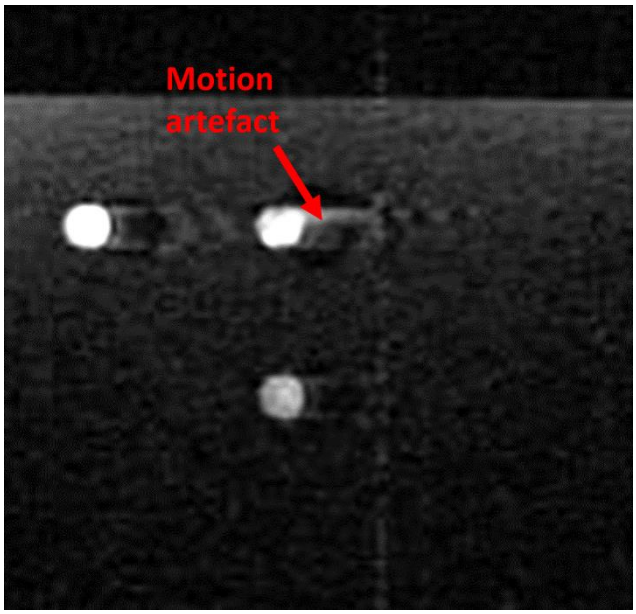

Fig. 3.11 Motion artefact on MR image of phantom.

MEMS mirrors are susceptible to vibrations. The MEMS mirrors used for the FMT-MRI 3.0 showed resonance peaks at around 430 Hz with a quality factor (Q-factor) of 30 and around 950 Hz with a Q-factor of 9 (Fig. 3.12). The Q-factor is defined as

$$Q = 2\pi * \frac{Energy\ stored}{Energy\ dissipated\ per\ cycle} \tag{3.1}$$

A MEMS mirror with a high Q-factor is more susceptible to mechanical vibration, shock and acoustic waves. Once excited, the MEMS mirror oscillates for several cycles according to equation (3.1). 21% of the total energy is consumed per cycle and therefore the energy is exponentially reduced or after 20 cycles the energy is reduced to 1% of the initial energy.

Several strategies might be envisaged to overcome this problem. Magnetic field gradient switching and vibrations associated to it are an intrinsic feature of MRI. Interference with vibration sensitive equipment such as MEMS mirrors might be reduced by reducing the strength of the source (i.e. the vibrational amplitude), by reducing the impact of the vibrations on the components, or by separating gradient switching and MEMS operation in the time domain. The effect of reducing the source strength is indicated by the fact that distortions are less severe when using sequences with lower gradient duty cycle such as TurboRARE. Vibration amplitudes might decrease by using so-called 'silent' gradients [11]. Alternatively, the susceptibility of the device towards vibrations could be reduced.

Several options might be considered to lower the susceptibility of the system:

a) The FMT probe could be damped with dampers or harmonic absorbers.

b) MEMS mirrors with lower Q-factors, which are more robust towards vibrations, could be used instead.

c) Selection of MEMS mirrors with resonance peak at higher frequencies that might not be excited by the MRI vibrations, e.g. MEMS mirrors with smaller mirrors.

The manufacturer of the devices used is currently working on the development of MEMS devices with reduced Q-factors. Damping may also be achieved by immersing MEMS devices in viscous dielectric liquids, which would lead to near critical damping. The challenge is to produce such devices without air bubbles, evaporation of the solvent or leaks. Therefore alternative strategies are pursued such as increasing pressure, filling the MEMS package with inert gases or modifying the MEMS package ([12], [13]). It can be expected that the oscillations of the MEMS mirrors during mechanical vibrations associated with MRI data acquisition can be strongly diminished to an acceptable level in future. In the meantime, the current system uses interleaved scanning, as MRI sequences typically involve relaxation delays, i.e. time intervals during which no gradients are switched. These time windows could be used for FMT readouts by synchronizing FMT data acquisition with MRI scanning. Similarly, when studying relatively slow kinetic processes using heavy duty MRI sequences such as EPI and short TR-FLASH, FMT data acquisition might be triggered to the gaps in between subsequent images.

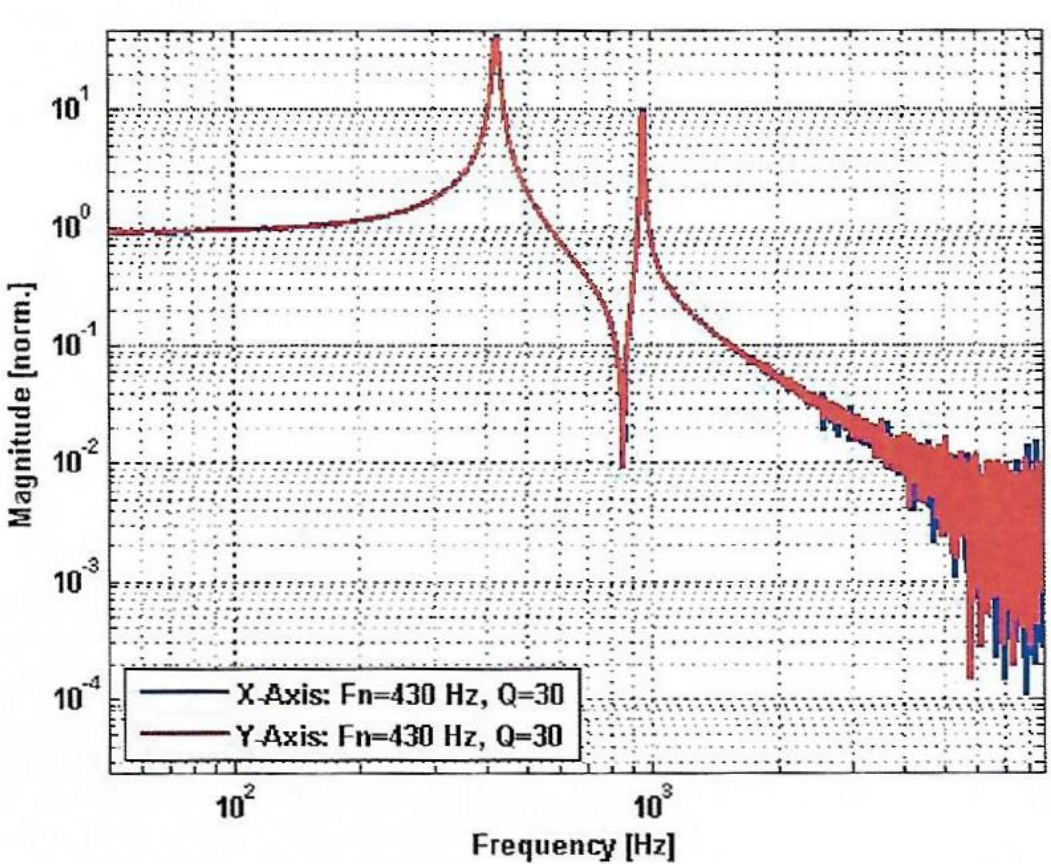

Fig. 3.12 Frequency response of MEMS mirror with mirror diameter of 3mm [14].

3.4.3 Sensitivity of the Detection System

Direct sensitivity comparison across systems is difficult, as different camera modules have been used. In analogous experiments using reflection-mode FMT in combination with comparable tissue mimicking phantoms, readouts of phantoms with the FMT-MRI 1.0 system using a SPAD detector yielded an average SNR value of 3.6 [6]. The FMT-MRI 2.0 using a cooled CMOS camera yielded SNR=263 [15], and the FMT-MRI 3.0 using an sCMOS sensor SNR=303 (in spite of reduced laser power and reduced exposure time and increased fluorescence depth). While these values cannot be compared directly, it is obvious that cooling of the sensor led to a significant improvement in sensitivity. The improvement from FMT-MRI 2.0 to 3.0 is due to better camera specifications such as higher quantum efficiency and lower readout noise. Although improvement in sensitivity is certainly a critical aspect in any FMT system, it was not the focus of the FMT-MRI 3.0 development. Given the modular design of the setup there is substantial room for sensitivity improvement. For example, laser sources with significantly higher output (up to 200 times higher) could be used – though care has to

be taken to avoid any artifacts due to excessive tissue heating. Also, novel improved camera designs could be easily implemented.

3.4.4 FMT Reconstruction

The FMT data correctly determined the glass capillary tube containing the Cy5.5, which cannot be seen from the MR image. The depth of the capillary tube with the fluorescent dye was underestimated. The depth was estimated to be between 2.2mm-2.8mm (Fig. 3.8a). Underestimation of depth in phantoms using FMT reflection mode has been found before with other FMT devices and seems to be intrinsic to FMT in reflection mode imaging structures at levels of around 3mm or deeper [15]. The horizontal position of the fluorescent dye coincides well with the MR data.

3.4.5 Handling

The principal objective designing a compact FMT-MRI hybrid imaging system easy to operate was achieved. As the optical components are intrinsically aligned, time-consuming calibrations steps can be avoided and general handling of the hybrid system could be clearly improved. The animal support comprising stereotactic head fixation and the MRI transceiver surface coil is designed as a drawer that can be easily unplugged from the FMT probe. The animal support is typically placed next to the anesthesia induction box where the mouse is prepared to be afterwards inserted into the FMT probe. Acquisition parameters to be set are selection of reflection or transmission mode, incident laser power, camera integration time, number of FMT sources (illumination points), and coordinates of illumination points in the x-y coordinate frame. The FMT probe is then fixed on the carriage of the linear guiding system and positioned at the isocenter of the MRI magnet. Neither a calibration step nor a precise positioning of the FMT probe is required and the FMT-MRI data acquisition can be initiated.

The current system is still a prototype version designed in a modular manner, i.e. most of the modules involved are connected individually via the connector flange of the FMT probe. Detector cooling requires connections to a water circulating system and a power supply. The animal support has to be connected with the anesthesia supply and another water pump for heating of the animal during anesthesia. The MEMS mirror, the laser and the camera module have to be connected to the computer, the power outlet or both. A future simplification could unify these connectors in a single cable assembly.

1. Umezawa, K., A. Matsui, Y. Nakamura, D. Citterio, and K. Suzuki, *Bright, color-tunable fluorescent dyes in the Vis/NIR region: establishment of new "tailor-made" multicolor fluorophores based on borondipyrromethene.* Chemistry–A European Journal, 2009. **15**(5): p. 1096-1106.
2. PerkinElmer. *ProSense 680 Fluorescent Imaging Agent*. [cited 2017 June 2nd]; Available from: https://www.perkinelmer.com/lab-solutions/resources/docs/TCH_NEV10003ProSense680TD.pdf
3. Ntziachristos, V. and R. Weissleder, *Experimental three-dimensional fluorescence reconstruction of diffuse media by use of a normalized Born approximation.* Optics letters, 2001. **26**(12): p. 893-895.
4. Schwarz, H., *The method of conjugate gradients in finite element applications.* Zeitschrift für Angewandte Mathematik und Physik (ZAMP), 1979. **30**(2): p. 342-354.
5. Hennig, J., A. Nauerth, and H. Friedburg, *RARE imaging: a fast imaging method for clinical MR.* Magnetic resonance in medicine, 1986. **3**(6): p. 823-833.
6. Frahm, J., A. Haase, and D. Matthaei, *Rapid NMR imaging of dynamic processes using the FLASII technique.* Magnetic resonance in medicine, 1986. **3**(2): p. 321-327.
7. Mansfield, P., D. Guilfoyle, R. Ordidge, and R. Coupland, *Measurement of T1 by echo-planar imaging and the construction of computer-generated images.* Physics in medicine and biology, 1986. **31**(2): p. 113.
8. Tung, C.-H., U. Mahmood, S. Bredow, and R. Weissleder, *In vivo imaging of proteolytic enzyme activity using a novel molecular reporter.* Cancer research, 2000. **60**(17): p. 4953-4958.
9. Ripoll, J., R.B. Schulz, and V. Ntziachristos, *Free-space propagation of diffuse light: theory and experiments.* Physical review letters, 2003. **91**(10): p. 103901.
10. Milanovic, V. *Linearized gimbal-less two-axis MEMS mirrors*. Optical Fiber Communication Conference 2009; JThA19].
11. Hennel, F., F. Girard, and T. Loenneker, *"Silent" MRI with soft gradient pulses.* Magnetic resonance in medicine, 1999. **42**(1): p. 6-10.
12. Milanovic, V., A. Kasturi, and J. Yang. *Novel fluidic packaging of gimbal-less MEMS mirrors for increased optical resolution and overall performance*. in *SPIE Defense+ Security*. 2016. International Society for Optics and Photonics.
13. Milanović, V., A. Kasturi, J. Yang, Y.R. Su, and F. Hu. *Novel packaging approaches for increased robustness and overall performance of gimbal-less MEMS mirrors*. in *SPIE OPTO*. 2017. International Society for Optics and Photonics.
14. MirrorcleTechnologies, *Gimbal-Less Two-Axis Scanning MEMS Micromirrors Device Datasheets S4395, S4396*. 2014.
15. Stuker, F., *Hybrid imaging: combining fluorescence molecular tomography with magnetic resonance imaging.* Diss. ETH No. 19664, 2011.

Chapter 4

Dynamic Measurement of Tumor Vascular Permeability and Perfusion using a Hybrid System for Simultaneous Magnetic Resonance and Fluorescence Imaging

The following chapter is adapted from:

Wuwei Ren, Andreas Elmer, David Buehlmann, Mark-Aurel Augath, Divya Vats, Jorge Ripoll, Markus Rudin; "Dynamic Measurement of Tumor Vascular Permeability and Perfusion using a Hybrid System for Simultaneous Magnetic Resonance and Fluorescence Imaging"; Molecular Imaging and Biology; 2015; in press. It has a shared first-authorship of Wuwei Ren and Andreas Elmer. Contributions of Andreas Elmer in this paper were:

- Development of the FMT-MRI 2.0
- Preparation of the FMT/dFRI experiment
- Execution of the FMT/dFRI experiment
- Data analysis (FMT reconstruction excluded)

This chapter illustrates a biomedical application of the hybrid FMT-MRI system.

4.1 Introduction

Combining FMT with a high-resolution (HR) imaging method offers two advantages: (1) information on the distribution of fluorescent sources can be matched to coregistered anatomical reference data and (2) anatomical data can be used as prior information in the reconstruction of FMT data, which leads to better confinement of the ill-posed problem. Yet registration of molecular information to anatomical data does not require a simultaneous imaging hybrid system: in most applications, data could be obtained sequentially using a suitable sample support compatible with both modalities. The true potential of hybrid systems is simultaneous measurements, which can be exploited e.g., in correlative functional studies, particularly under conditions when the investigated biological system fluctuates over time. This has been shown, e.g., for functional studies of rat brain comparing PET and MRI perfusion [1, 2].

Measurements of vascular function are also of relevance for the characterization of tumor neoangiogenesis, a critical step in tumor progression. To sustain growth, a tumor has to establish its

own vascular system, which is triggered by the secretion of proangiogenic factors in response to hypoxia [3]. Tumor neovasculature is chaotic and subject to physiological fluctuations. Newly formed tumor vessels are immature and show increased vascular permeability compared to mature vessels in healthy tissue. This feature has been extensively exploited for diagnostic purposes and for assessing therapy response to antiangiogenic treatment: increased leakage of contrast agents (paramagnetic gadolinium complexes) from the vasculature assessed by dynamic contrast-enhanced MRI (DCE-MRI) is considered an indicator of neoangiogenesis [4, 5]. Apart from changes in permeability, vessel formation is also reflected by an increase in the tumor blood volume, which can be assessed using macromolecular contrast agents [4-6].

Vascular permeability and perfusion information in tumors can be derived from imaging studies with non-targeted fluorescent probes [7]. Using FMT, Wall et al. [8] could evaluate the degree of tumor angiogenesis by monitoring the signal intensity at the tumor following the administration of the cyanine dye SIDAG. Similar measurements were reported by Montet et al.[9], who measured vascular volume fractions of tumors longitudinally and observed treatment response using fluorescence imaging. A clinical feasibility study was carried out by Ntziachristos et al. [10] comparing differences in uptake of indocyanine green and Gd-based agents in a sequential MRI-FMT protocol. Most recently, Davis et al. [11] used an MRI-guided multispectral FMT system to quantify the density of epithelial growth factor receptors (EGFRs) in gliomas in vivo by comparing the uptake kinetics of a fluorescently labeled anti-EGFR affibody with that of a labelled control affibody. The temporal resolution in this dynamic experiment was 2 min, which is relatively fast for FMT data. While this is fast enough compared to the time-scale of probe–receptor interactions, it may not be sufficient for capturing the dynamics of vascular inflow or passive extravasation of a fluorescent label. This is due to the intrinsic principle of FMT measurements, which require sequential recording of excitation and corresponding emission maps for various positions of a scanned light source [12]. To achieve temporal resolution in the order of seconds required for dynamical monitoring of tracer inflow, planar imaging has been shown as a practical solution, in particular when studying subcutaneous tumors [13].

In this study, we explored the potential of a homebuilt FMT/MRI setup [14] for acquiring simultaneous dynamic information characterizing the tumor neovasculature of subcutaneously implanted mammary tumors in mice. We have measured vascular permeability using a mixture of two extravascular imaging agents, GdDOTA and the fluorescent dye Cy5.5, and tumor perfusion using a mixture of two intravascular agents, iron oxide nanoparticles and a fluorescently labelled macromolecule. This was achieved by implementing a dynamic fluorescence reflectance imaging (dFRI) mode into the hybrid system. Prior to and following the dFRI measurements, MRI and FMT datasets have been acquired to estimate the tracer distribution in three dimensions. Analysis of dynamic imaging data yielded a good correspondence between the quantitative MRI and FMT/dFRI readouts for permeability, extracellular

volume, and tumor blood volume. The good correlation between physiological parameters derived from MRI and FMT/dFRI reveals that optical imaging is able to capture physiological processes in a (semi-)quantitative manner.

4.2 Materials and Methods

4.2.1 Animals and Tumor Model

All experiments were conducted in accordance with the regulations of the Cantonal Veterinary Office of Zurich, Switzerland. Female BALB/c-nu mice were obtained at 6–8 weeks of age and maintained at 22–24 °C on a 12/12-h light/dark cycle with access to food and water.

4T1 breast cancer cells (ATCC®-CRL-2539™) were cultured to 80 % confluence in RPMI medium containing 10 % fetal calf serum at 37 °C. Animals were injected subcutaneously in the left flank with 10^6 cells in 100 µl phosphate-buffered saline (PBS) using a 31G insulin syringe. Four mice each were used for permeability and perfusion measurements.

4.2.2 Imaging Agents

4.2.2.1 Fluorescent Probes

Two fluorescence probes, Cy5.5 and AngioSense 680EX (PerkinElmer, USA, called AngioSense below), were used. The spectrum of Cy5.5 shows an absorption maximum at the wavelength of 673 nm and emission maximum at 692 nm, respectively. AngioSense is a near-infrared labelled fluorescent macromolecule. Its spectrum shows an absorption maximum at 670 nm and an emission maximum at 690 nm, respectively.

4.2.2.2 MR Contrast Agents

Two MRI contrast agents have been used. GdDOTA (Guerbet, Paris) is an extravascular contrast agent, while Endorem (Guerbet, Paris) is dextran-coated iron oxide nanoparticles used as an intravascular contrast agent.

4.2.3 Imagers

The FMT/MRI hybrid system (Fig. 4.1) is a modification of a previously described system [14] designed as an insert to a Biospec 94/30 scanner (Bruker BioSpin GmbH, Germany). The FMT detector module comprises both a radiofrequency (RF) transmit-receive surface coil and a complementary metal-oxide-semiconductor (CMOS) detector (CSEM, Switzerland) with 256×256 pixels for photon detection. A lens system is used to image the animal's surface onto the sensitive area of the CMOS chip with proper wavelength selected by choosing a bandpass filter implemented in a filter wheel (660±13 nm for the

excitation, 700 nm±13 nm for the emission). Dark current noise was reduced by mounting the thermoelectric cooler on the CMOS chip (Custom Thermoelectric, USA). The printed circuit board (PCB) with the CMOS detector was placed inside a thermally insulated box made of polymethacrylimide and shielded with copper from electromagnetic interference at RF range (Fig. 2.5). The whole insert is mounted on an MRI-compatible support for efficient handling.

For dFRI studies, continuous focal illumination (diameter 1 mm) at the center of a tumor was used, and serial images were recorded in rapid succession. Laser power, exposure time, duration, and frame rate of dFRI could be adjusted. During dFRI mode, the 700±13-nm filter was selected to record the fluorescence signal. Frame rates of up to 60/min are feasible.

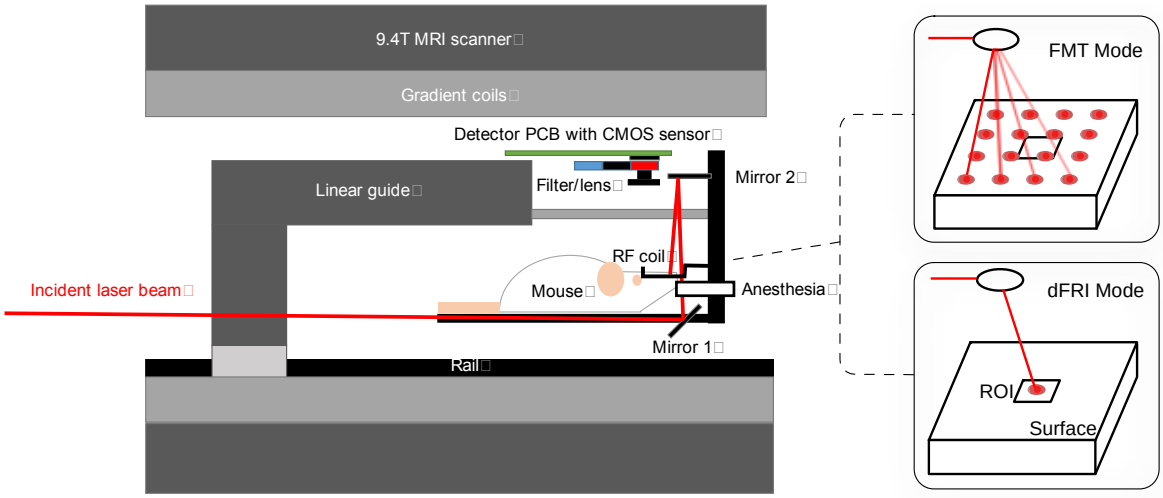

Fig. 4. 1 Schematics of FMT/MRI hybrid system: FMT mode and dFRI mode. The illumination module containing the scanning device was positioned outside MR scanner. An incident laser beam can be steered by the galvanometric driven mirrors of the scanning device and then directed via a mirror system built in the animal cradle to the region of interest (mirror 1 and 2). The animal cradle, designed as an insert to the 9.4T/30cm bore magnet, comprises the CMOS detector array with the corresponding printed circuit board (PCB), the filter wheel with up to 6 optical band-pass filters, the radiofrequency surface coil operating transmit/receive mode (RF coil) and the anesthesia supply. The two inserts reprent the two scanning modes used in the current study: sequential grid illumination for the FMT measurement and a single point irradiation for the fast dFRI measurement.

4.2.4 Characterization of Mixtures of Imaging Agents

Prior to in vivo experiments, we evaluated whether the fluorescence signal of Cy5.5 was influenced by the presence of GdDOTA when mixed in solution. Capillaries containing a fixed concentration of Cy5.5 (2 nmol/ml) in PBS were doped with varying amounts of GdDOTA (0, 6.25, 12.5, 25, 50, 100, and 200 µmol/ml). The fluorescence intensity was analyzed using a planar imaging system (Maestro, PerkinElmer, USA). Additionally, we analyzed the effect of dilution at a fixed concentration ratio of Cy5.5 and GdDOTA. Similarly, we investigated to what extent the presence of Cy5.5 at concentrations

of 0, 0.05, 0.1, 0.2, 0.4, 0.8, 0.16, 0.32, and 0.64 nmol/ml had an effect on the relaxivity of a GdDOTA solution in PBS (1.25 µmol/ml).

4.2.5 Measurement Protocols

The protocols for permeability and perfusion measurements comprised a preparation phase (10 min), recording of 3D HR baseline images (phase I, 30 min), dynamic measurements during the infusion of the imaging agents (phase II, 45 min), and the recording of post-infusion 3D HR images (phase III, 30 min) (Fig. 4.2).

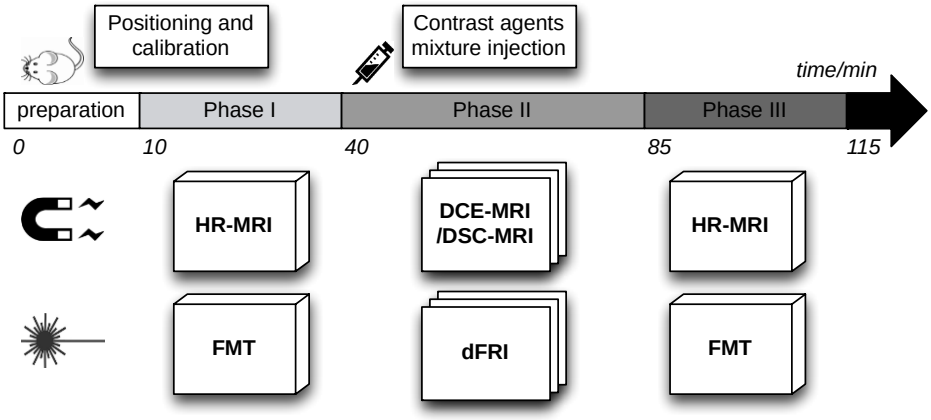

Fig. 4. 2 Experimental protocols for permeability and perfusion measurements. The general protocol is composed of preparation for animal positioning and system calibration, phase I for pre-contrast scanning, phase II for dynamic measuring and phase III post-contrast scanning. Numbers indicate time in minutes.

4.2.5.1 Preparation

Mice were anesthetized using 1.5 % isoflurane in oxygen/air (1:2) and positioned in a cradle with warm water supply to maintain the body temperature at 37±0.1 °C. An infusion line was placed in the tail vein, allowing administration of imaging agents while the mouse was positioned in the magnet. Thereafter, the cradle was inserted into the MR scanner, and optical system calibration was carried out.

4.2.5.2 Phase I

HR-MRI and FMT data sets were recorded simultaneously. For permeability measurements (GdDOTA), a T_1-weighted gradient-echo pulse sequence has been used with sequence parameters: field-of-view (FOV)=22 mm×22 mm, number of slices=16, dimension of reconstructed matrix=256×256×16, slice thickness=0.5 mm, repetition delay (TR)=200 ms, echo delay (TE)=2.51 ms, and pulse angle α=25°. For perfusion measurements (Endorem), a T_2*-weighted gradient echo sequence was applied with identical geometrical parameters and TR=2500 ms, TE=20 ms, and α=90°.

For concurrent FMT measurement, a white-light image was taken first. Thereafter, a matrix of 10×10 laser excitation point sources was defined according to the specific geometry of each subject surface,

typically covering an area of 20 mm×20 mm. For each excitation point, a pair of excitation and emission maps has been recorded.

4.2.5.3 Phase II

Dynamic fluorescence and MRI measurements were carried out simultaneously. For both permeability and perfusion measurements, baseline values were recorded for 5 min before administration of the mixture. For permeability and perfusion measurements, a mixture of 2 nmol Cy5.5/25 µmol GdDOTA and 2 nmol AngioSense/25 µmol Endorem in PBS were used, respectively. The injected volume in both cases was 100 µl, and infusion rate was set to 2000 µl/min.

For DCE-MRI, a single cross section in the middle of tumor was selected. A T_1-weighted gradient echo pulse sequence was applied with FOV=22 mm×22 mm, slice thickness 1 mm, matrix dimension=110×80, TR=12.5 ms, TE=2.51 ms, and α=7°. Acquisition of 2400 consecutive images took 40 min (1 s/image). For perfusion measurement, a T_2*-weighted gradient echo sequence with identical geometrical parameters and TR=25 ms, TE=2.51 ms, and α=15° was used with 1200 images recorded in 40 min (2 s/image).

For dFRI, the laser point source with a full-width half-maximum of about 1 mm was positioned above the center of the tumor, and the filter was set to 700±13 nm. Kinetics of tracer uptake during permeability measurement allowed imaging at six frames per minute using a laser power of 20 mW and integration time of 50 ms. To capture the fast tracer dynamics during the perfusion measurement, the frame rate was set to 60/min for the first 10 min and later to 2/min for the remaining 30 min with a laser power of 10 mW and an integration time of 50 ms.

4.2.5.4 Phase III

Static HR-MRI and FMT data sets were recorded to assess the final uptake of the imaging agents using the parameters described for phase I.

4.2.6 Data Analysis

4.2.6.1 FMT Reconstruction/MR Data Processing

Raw FMT image stacks from phase I and phase III were reconstructed using the normalized Born approximation and ART inversion method [15]. Details on the reconstruction have been published previously [14]. All MRI raw data were processed using ParaVision software (Bruker BioSpin, Germany).

4.2.6.2 Registration of MR and Optical Images

For accurate ROI analysis, image registration between MRI and optical images was carried out. First, the top surface of the mouse was reconstructed from a stack of HR-MRI images. An adaptive Wiener

filter has been used to process each MRI slice. The filtering preserved the surface structures displaying relatively high contrast-to-noise ratio ranging from 20 to 40, while structures displaying a CNR≤5 were removed (Fig. 4.3). The surface displayed artifacts caused by the RF coil, which were used as intrinsic landmarks. Secondly, a non-reflective similarity transformation was calculated by mapping the MR data onto the optical surface (Fig. 4.3). Three types of landmarks were used: tumor sites, coil position, and body edges. A least square method was used to optimize the transformation matrix. Finally, the same transformation was applied to the whole MRI image stack. HR-MRI images were used as

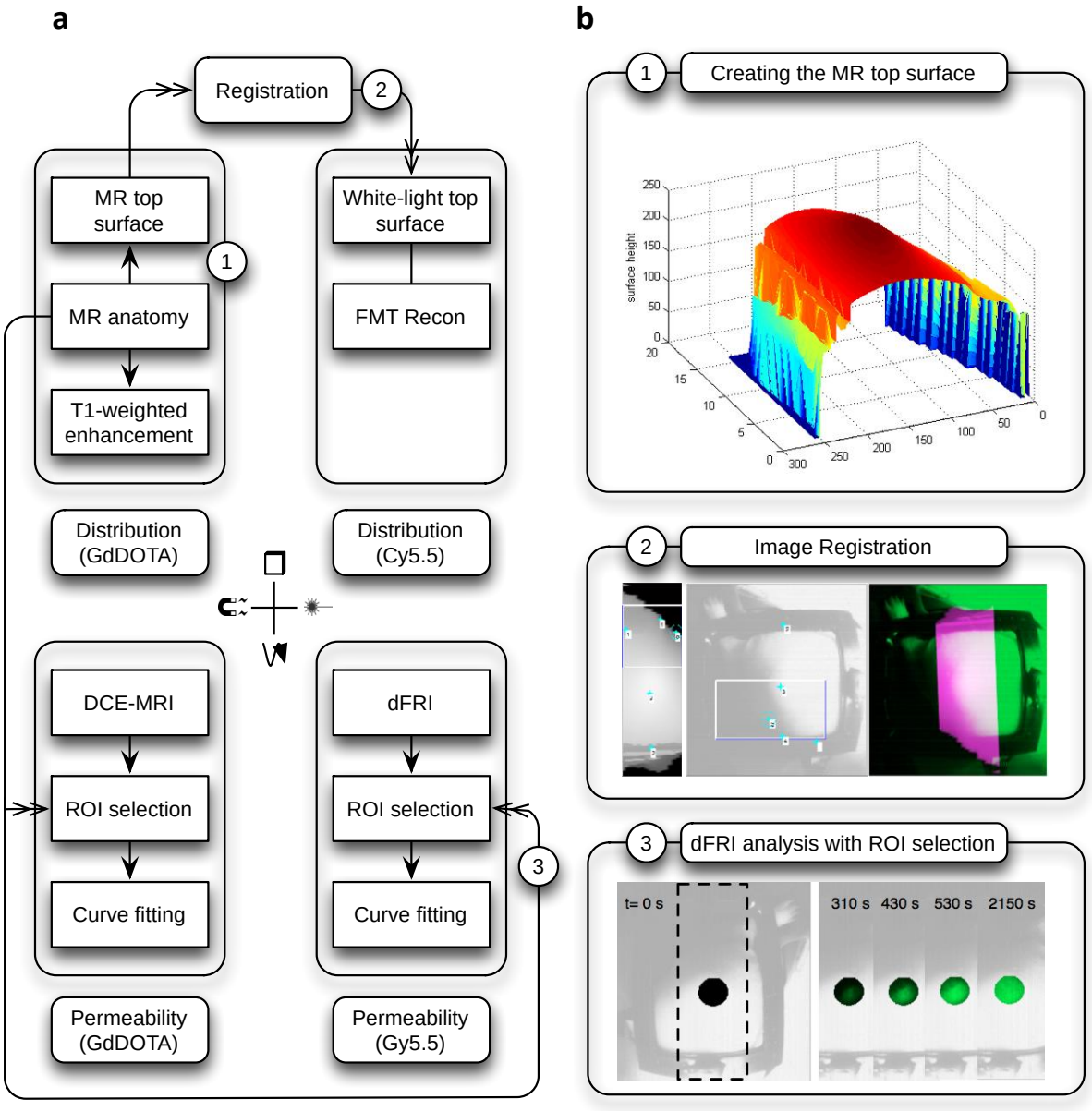

Fig. 4. 3 Schematic of data analysis. The four blocks in (a) refer to static HR MRI (upper left), DCE-MRI (lower left), FMT (upper right), and dFRI (lower right) data. By creating the MRI top surface, MR and optical data are co-registered. MR structural reference serves as the mask for ROI selection for DCE-MRI and dFRI. (b) Three most important steps in data processing: 1) generation of top surface from the static MRI data, 2) image registration by selecting three types of landmarks (tumor sites, coil position, and body edge) on both MR top surface (left) and white light image (middle), 3) the quantitative analysis of dFRI data using the ROI indicated.

reference frame for FMT and dFRI analysis. T_1 (T_2)-weighted MR enhancement images were inherently registered and did not require any additional transformation.

4.2.6.3 Analysis of Dynamic MRI and Optical Data

A) Vascular Permeability

Extravasation of GdDOTA and Cy5.5 was estimated using a two-compartment model [6, 16]. Assuming the plasma concentration of the imaging agent $c_{p,Gd}(t)$ to behave as a step function ($c_{p,Gd}(t)=0$ for $t<0$ and $c_{p,Gd}(t)=c_{p,Gd}$ for $t\geq 0$) and the plasma fractional volume v_p to be much smaller than the extracellular fractional volume $v_{e,Gd}$, we obtain for the tissue concentration of GdDOTA:

$$c_{t,Gd}(t) = v_{e,Gd} \cdot c_{p,Gd} \cdot \left[1 - \exp\left(-\frac{k_{Gd}}{v_{e,Gd}} \cdot t\right)\right] \qquad (4.1)$$

k_{Gd} being the transfer constant. The initial slope becomes $c_{p,Gd} \cdot k_{Gd}$, i.e. proportional to transfer constant k_{Gd} describing the permeability of the vessel wall, while the final uptake $c_{t,Gd}(\infty)=v_{e,Gd} \cdot c_{p,Gd}$ constitutes a measure for the interstitial leakage space $v_{e,Gd}$.

Tissue concentrations of GdDOTA, $c_{t,Gd}(t)$ were estimated from the DCE-MRI signal enhancement $S(t)/S(0)$ according to [6],

$$c_{t,Gd}(t) = \frac{R_{10}}{r_{1,Gd}} \cdot \left(\frac{S(t)}{S(0)} - 1\right) \qquad (4.2)$$

where $S(t)$ and $S(0)$ represent MRI signal intensity at time t and prior to contrast agent administration, respectively, $R_{10}=1/T_{10}$ the tissue relaxation rate in the absence of the contrast agent and $r_{1,Gd}$ the molar relaxivity for GdDOTA.

For the dFRI experiment the concentration profile $c_{t,Cy}(t)$ was deduced directly from the fluorescence signal intensity $S(t)$. For the regression analysis a ROI was selected based on the HR anatomical image and k_{Gd} (k_{Cy}) determined from regression analysis of the experimental uptake curves using equation (4.2), while $v_{e,Gd}$ and $v_{e,Cy}$ were determined from the signal intensities of the respective pre- and post-contrast images.

B) Perfusion

Endorem and AngioSense signal changes are dominated by the contributions of the respective agents in the plasma compartment. For Endorem, assuming a linear relationship between relaxation rate $R_2^*(t)$ and amount of tracer in plasma $c_{p,Endo}(t) \cdot v_p$, the amount of tracer can be estimated according to

$$c_{p,Endo}(t) \cdot v_p \propto -ln\left(\frac{S(t)}{S(0)}\right) \qquad (4.3)$$

with $S(0)$ and $S(t)$ being the MRI signal intensity prior and at time t after the administration of the contrast agent (Endorem). For $t \to \infty$ the relative tumor blood volume (rTBV) or v_p can be deduced as

$c_{p,Endo}(\infty)$ and is assumed to be in steady state, while in the initial phase following tracer administration the slope $\partial c_{p,Endo}(t)/\partial t$ serves as indicator for perfusion rates.

The analysis of the AngioSense results is straightforward as the plasma concentration $c_{p,Angio}(\infty)$ is assumed to be directly proportional to the measured signal intensity. Thus, the perfusion rate can be derived from the slope of the dFRI curve, while rTBV can be estimated from the FMT images recorded at phase I (pre-administration) and phase III (post-administration).

4.3 Results

4.3.1 Characterization of Mixtures of Imaging Agents

The addition of increasing amounts of GdDOTA to a Cy5.5 solution (2 µM) led to an enhancement effect of the fluorescence signal of up to 50 % for a GdDOTA concentration of 100 mM (Fig. 4.4), yet these concentrations were significantly higher than typical tissue concentrations, and we therefore assume

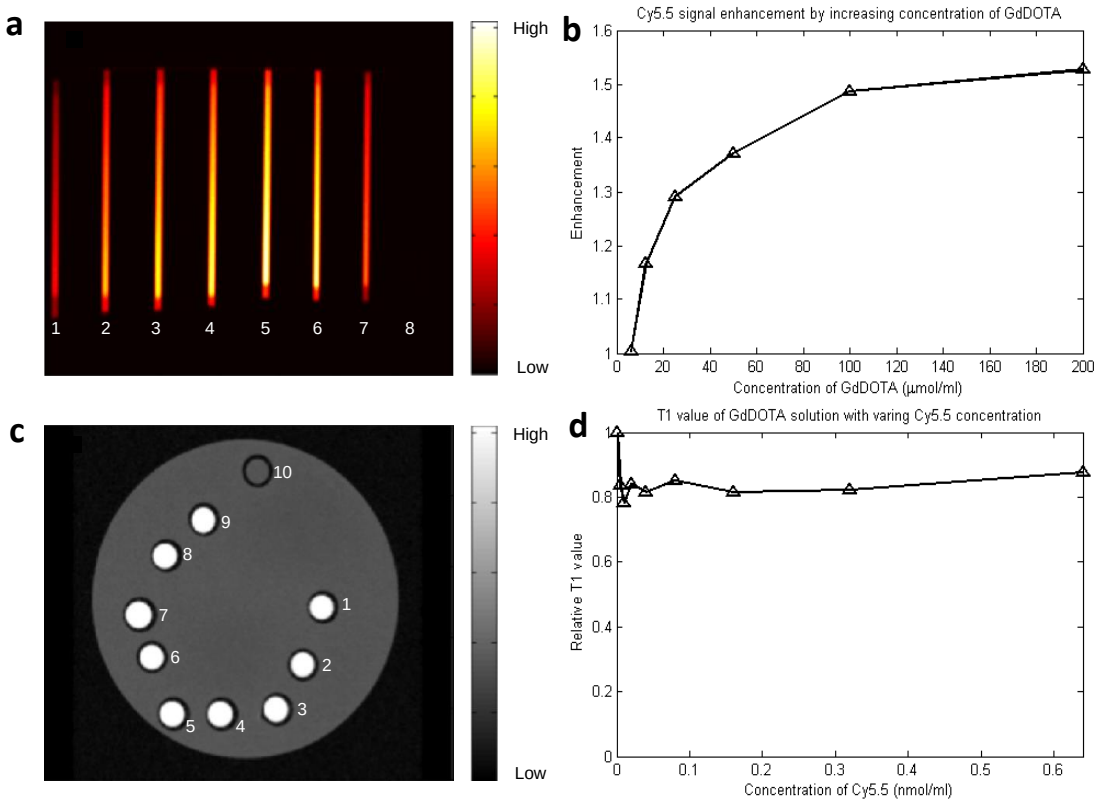

Fig 4. 4 Interference of imaging agents. (a) Effect of GdDOTA on Cy5.5 fluorescence intensity. The figure shows the results of a phantom recorded in Maestro system. Capillaries #1 to #6 comprise Cy5.5-GdDOTA mixture with varying amounts of GdDOTA (6.25, 12.5, 25, 50, 100, 200 µmol/ml) and fixed Cy5.5 (2 nmol/ml), while #7 contains only Cy5.5 (2nmol/ml) and #8 only GdDOTA (25 µmol/ml), yielding no fluorescent signal. (b) Cy5.5 fluorescent intensity is enhanced by addition of GdDOTA. (c) Effect of Cy5.5 on GdDOTA relaxation time. Tubes #1 to #8 contain Cy5.5-GdDOTA mixture with varying Cy5.5 (0.05, 0.1, 0.2, 0.4, 0.8, 0.16, 0.32, 0.64 nmol/ml) and fixed GdDOTA (1.25 µmol/ml), #9 only GdDOTA (1.25 µmol/ml) and #10 only PBS. (d) The curve for normalized T_1 values of Cy5.5-GdDOTA mixture indicates no effect of Cy5.5 on the relaxation rate of GdDOTA solution for low concentrations of Cy5.5.

that the GdDOTA did not affect the Cy5.5 in vivo signal. Similarly, we did not observe measurable effects of Cy5.5 on the R1 relaxivity of GdDOTA solutions.

4.3.2 Dynamic Uptake of Imaging Agents as Indicator of Vascular Permeability and Perfusion

Fig. 4.6 shows the tissue concentration as a function of time during the administration at t=300 s of the mixtures GdDOTA/Cy5.5 (permeability) and Endorem/AngioSense (perfusion). Concentration–time profiles were computed from experimental data using equation (4.2) and (4.3), respectively. They have been normalized for both modalities for comparison. Results are shown for individual mice for both dFRI (Fig. 4.6a, b) and DCE-MRI measurements (Fig. 4.6c, d). The simultaneous nature of the experiment is reflected in Fig. 4.6b, d, showing an experimental delay in administration of the contrast agent/dye mixture for one of the animals, which was accurately captured by both modalities. The mean

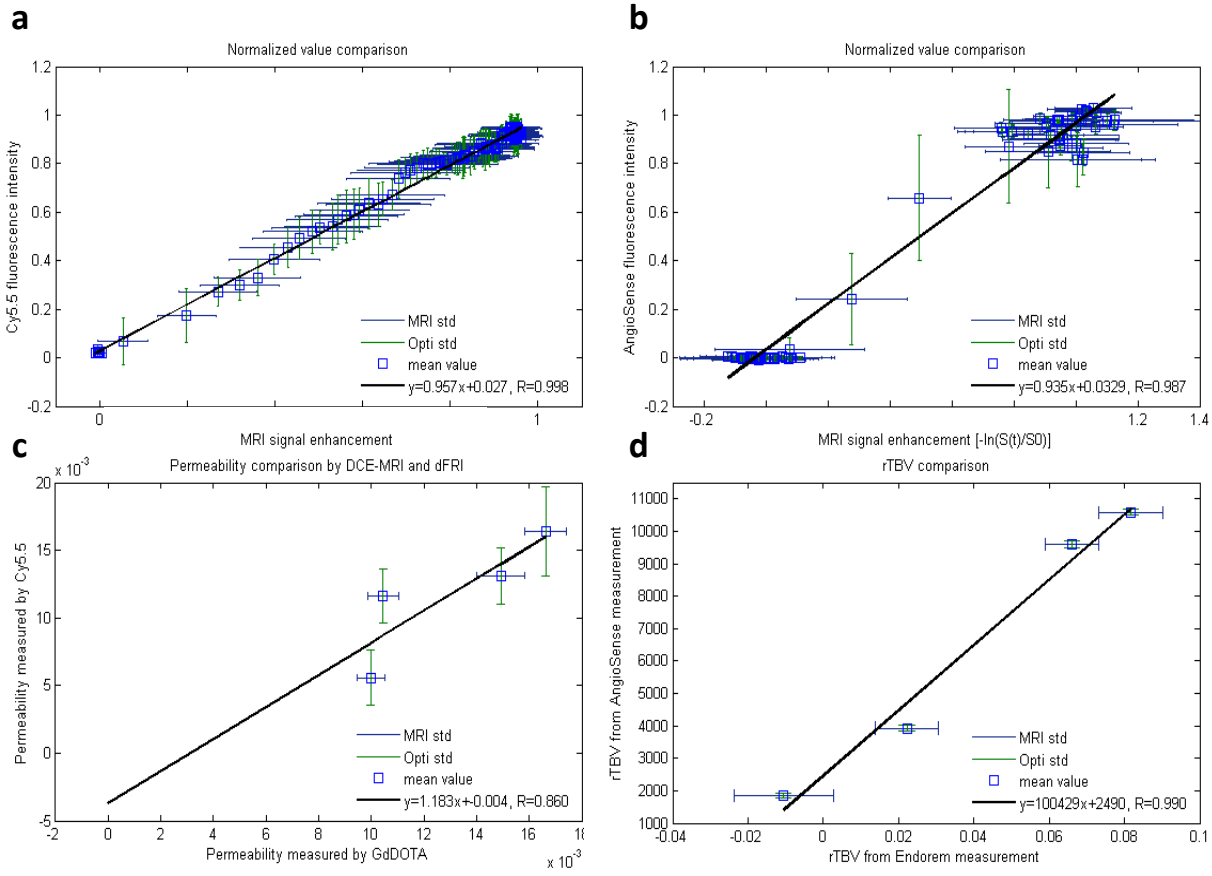

Fig 4. 5 Correlation of intensity normalized fluorescence and MRI measurements. The intensity of the two signals were compared for each measurement point. (a) Correlation of normalized values from Cy5.5 fluorescence intensity and MR signal enhancement with GdDOTA (adjusted to time resolution 10s). (b) Correlation of normalized values from AngioSense fluorescence intensity and MR signal enhancement with Endorem (adjusted to time resolution 2s). (c) Correlation of permeability coefficients (k_{Cy} and k_{Gd}) estimated from Cy5.5 and GdDOTA measurements; (d) Correlation of rTBVs estimated from AngioSense and Endorem measurements. For all images, standard deviation of MR and Optical results is described horizontally and vertically. Correlation coefficients (R values) are displayed in each figure.

values±standard deviation are shown in Fig. 4.6e, f, comparing fluorescence (blue) and MRI (red) signal intensities. For both types of experiments, the correspondence of the fluorescence and MRI measurement is excellent.

This correspondence of fluorescence and MRI readouts was further corroborated by calculating the correlation of the two curves. For the comparison of permeability measurements, the MRI data had to be downsampled to 10 s by averaging the values over subsequent 10 s intervals. The correlation

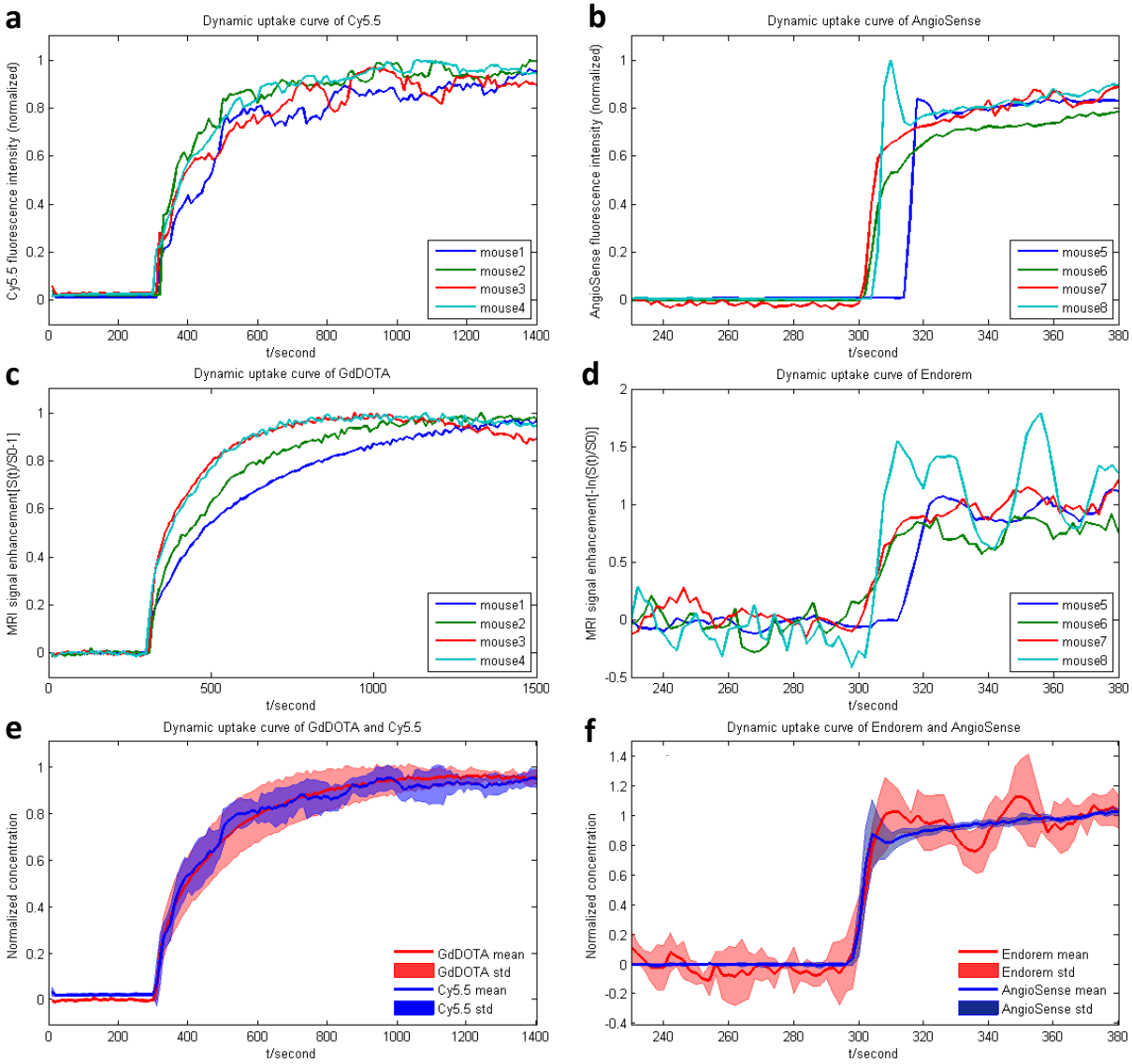

Fig 4. 6 Dynamic uptake curves for permeability and perfusion measurements: (a) dynamic uptake of Cy5.5 as derived from dFRI mode, (b) dynamic uptake of AngioSense from dFRI mode, (c) dynamic uptake of GdDOTA from DCE-MRI measurement and (d) dynamic uptake of Endorem from DSC-MRI measurement. Figs (a) to (d) show responses of individual mice as indicated in the panels. (e) Comparison of averaged dynamic uptake curves of Cy5.5 and GdDOTA (mean±std) for assessing vascular permeability in tumor. (f) Comparison of averaged dynamic uptake curves of AngioSense and Endorem as perfusion markers (tumor blood volume). In (e) and (f) MRI data are displayed ib red and dFRI data in blue. For both, standard deviation is shown in light colors.

coefficient comparing Cy5.5 and GdDOTA concentrations was R=0.998, while the slope of the regression line was a=0.957 (Fig. 4.5a). Including skin contribution in the ROI used for MRI data analysis in order to better mimic the dFRI situation did not significantly alter this value. The quality of the regression analysis is also reflected when comparing data of individual animals, yielding R values of 0.971, 0.968, 0.996, and 0.976 and slopes of a=0.976, 0.979, 0.981, 0.931, respectively. The correlation between normalized AngioSense and Endorem concentrations (Fig. 4.5b) was slightly inferior with R=0.987 and a=0.935, mainly due to the fact that the temporal resolution of 2 s was insufficient to properly capture the dynamics of tracer uptake. Correspondingly, data cluster around values of 0 and 1, respectively, which explains the high coefficient of correlation.

Vascular permeability is typically characterized by the transfer constant K^{trans} (k_{Gd} and k_{Cy} in our nomenclature, equation (4.1), which was estimated from the initial slope of the concentration-time curves. The corresponding correlation of K^{trans} derived from fluorescence and MRI measurements yielded an R value of 0.860 and a slope of a=1.18 (Fig. 4.5c). Similarly, the final uptake of imaging agent was estimated from exponential fitting, yielding an R value of 0.914 for the comparison Cy5.5 versus GdDOTA (Fig. 4.7a).

Compared with permeability measurement, the procedure of first bolus passage is much faster (5 - 10 s). The value of rTBV was calculated by averaging all data points during the last 100 s of the dynamic measurement phase yielding a good correspondence (R=0.990; Fig.5d). Perfusion rates were estimated by computing the slope $\partial c_p/\partial t$ during the first 6 s after administration of AngioSense and Endorem, and good agreement was achieved with R value of 0.909 (Fig. 4.7b).

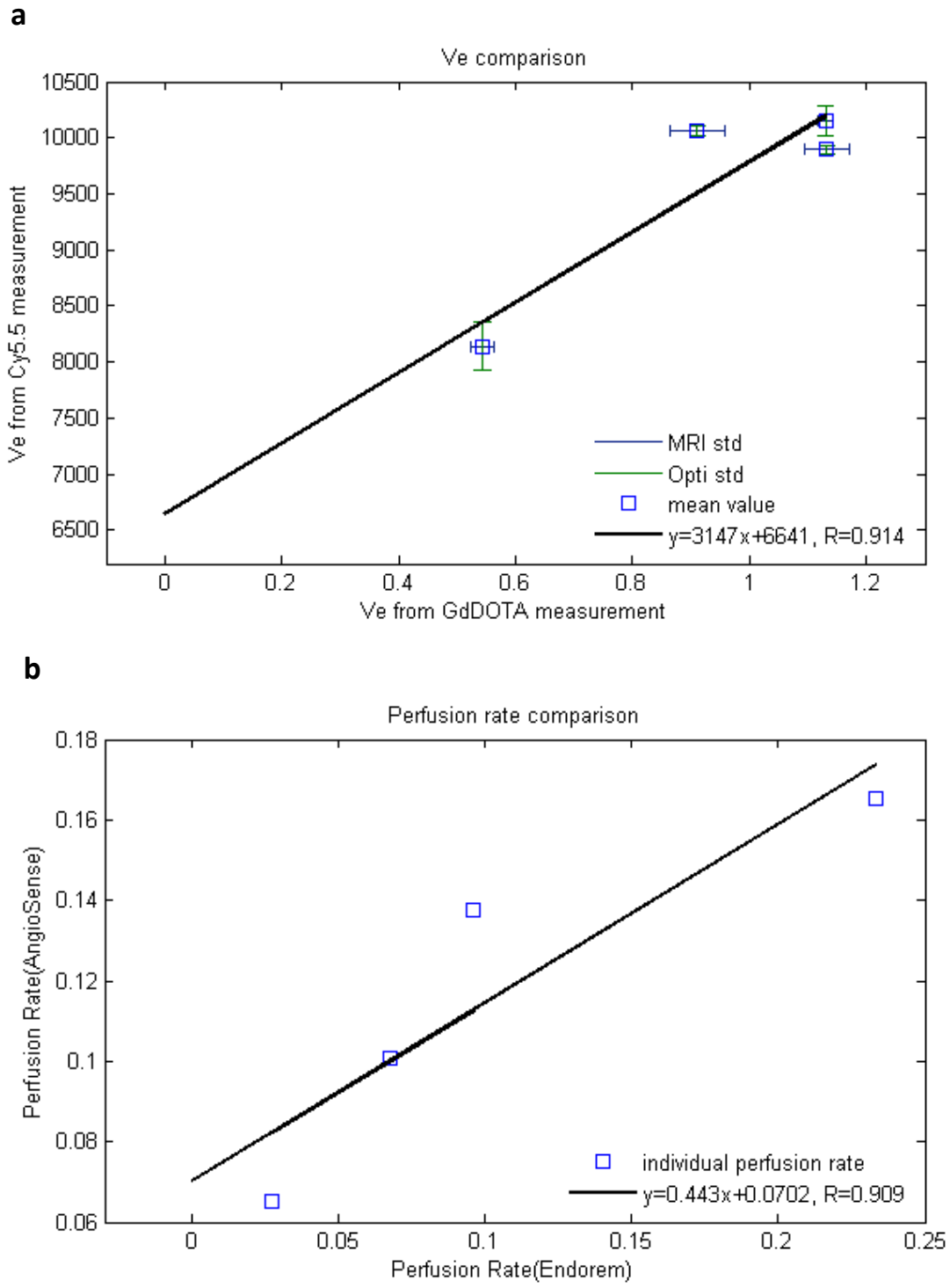

Fig 4. 7 Additional information extracted from dynamic study: (a) Correlation of total amount of extravasated tracer as measure of v_e. (b) Correlation of perfusion rate measured during the initial slope after administration of contrast agent (in the first 6 seconds).

4.3.3 Estimation of Imaging Agent Uptake by Pre- and Post-Contrast MRI and FMT Images

To assess tracer distribution in the tumor, we compared the images representing the final uptake of fluorescence and MRI agents. In Fig. 4.8, the first two rows represent the final distribution of Cy5.5 (Fig. 4.8b, e) and GdDOTA (Fig. 4.8c, f) as derived from FMT and HR-MRI images recorded 35 min following the tracer administration and the bottom rows that of AngioSense (Fig. 4.8h, k) and Endorem (Fig. 4.8i, l). Uptake images (color scale) are overlaid on anatomical reference scans (gray scale). The MRI data set shows that GdDOTA uptake (color) is highly heterogeneous across the tumor, with some uptake at the tumor periphery and significant uptake in regions of the tumor center (Fig. 4.8c, f). FMT reconstruction also reveals some heterogeneity in the distribution of Cy5.5, although the reconstruction suffers from inferior spatial resolution and some image reconstruction artifacts (Fig. 4.8b). This becomes even more obvious for images recorded with AngioSense, which is confined to vascular structures in the early phase following administration. The dye distribution reconstructed from the FMT data was found to extend beyond the tumor margin for mouse #3(Fig. 4.8h). The MRI images reveal that, in this case, the major signal sources are the vessels located at the tumor periphery (Fig. 4.8i). By convolving these point sources with the FMT point-spread function, it is inevitable that non-zero dye concentrations will be found outside of the tumor, yet the centers-of-gravity of dye and MRI contrast agent distribution were found to largely overlap for all mice.

For quantitative comparison, the MRI and fluorescence intensities have been averaged across two regions-of-interest (ROIs) comprising the central region of the tumor (ROI 1) and the other located in the adjacent skeletal muscle (ROI 2). Similarly, the MRI data recorded prior and following Endorem administration revealed heterogeneity of tracer uptake across the tumor, which was also reflected by the AngioSense uptake (Fig. 4.8n).

4.4 Discussion

MRI-based methods characterizing neoangiogenesis in tumors have become standard for tumor staging and for the evaluation of anti-angiogenic therapy [4-6]. While the method is inherently translational, its preclinical use is restricted by the limited availability of animal MRI systems. Alternative imaging strategies based on fluorescent readouts thus become attractive as such systems are increasingly available in research labs. Fluorescence imaging is sensitive and provides the temporal resolution required for dynamic measurements of dye uptake by the tissue, yet light scattering in tissue renders the extraction of quantitative information difficult. Therefore, validation of the fluorescence readout with established DCE-MRI assessing vascular permeability and DSC-MRI estimating tumor perfusion and local blood volume is essential. As tumor vascular physiology is chaotic and fluctuating,

simultaneous dynamic measurement of parameters characterizing the tumor vascular system using a hybrid FMT/MRI is considered critical. This was achieved by monitoring the changes in signal intensity with both imaging modalities simultaneously following the administration of a mixture of imaging agents.

The experimental data revealed an excellent correlation between dFRI and DCE-MRI uptake data for the permeability measurements both at the group level and for individual mice with R values>0.95 and a slope of the curve corresponding to the theoretical value within error limits. When comparing the permeability coefficients for GdDOTA and Cy5.5, a slightly inferior R value of 0.860 has been found. This might be explained by the much lower number of data points available (one per animal) and by the simplicity of the two-compartment model used. The model does not account for imaging agent clearance from the tumor compartment, an assumption that holds during the first phase of agent uptake, but not during later stages. Also, vascular permeability depends on the molecular structure of the imaging agent and hence should be different for Cy5.5 and GdDOTA, although this effect appears minimal as reflected by the R values. The higher degree of signal fluctuation of the fluorescence signal might be accounted for by infusing higher Cy5.5 concentrations. The correlation between MRI and fluorescence measurement for assessing tumor perfusion using intravascular imaging agents is inferior mainly due to the fact that the signal dynamics were too fast to be accurately captured, even at 1 s temporal resolution. The high R value arises from the fact that the correlation is dominated by the clustering of data points around (0,0) and (1,1), with only few intermediate points. Accurate comparison of perfusion measurements would require a temporal resolution better than 0.5 s.

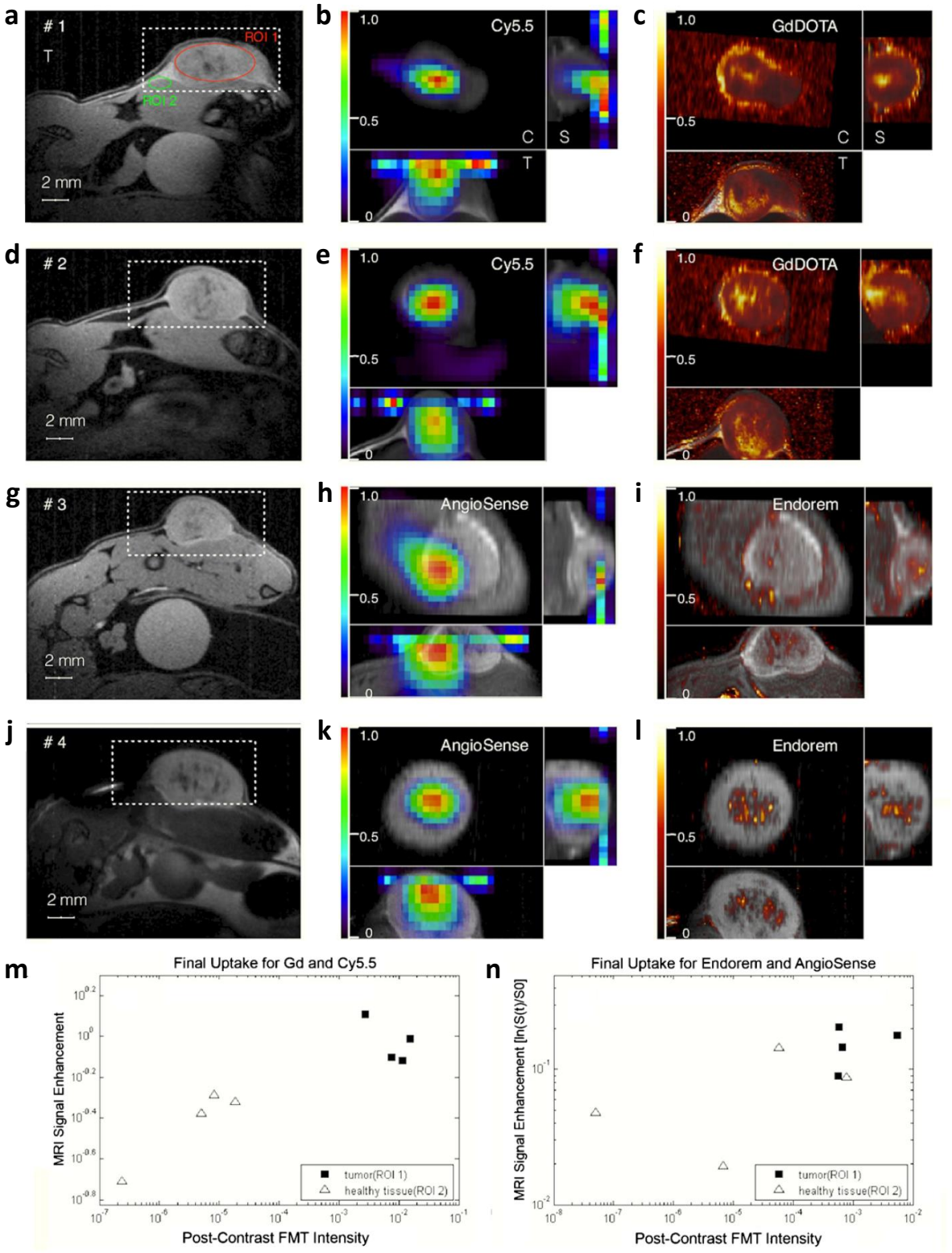

Fig 4. 8 Static images illustrating final uptake of imaging agents in 3D. The left column (a,d,g,j) shows HR-MRI anatomical reference. The mice are lying on the side with the spine placed on the left side. The circular structure in the center is the bladder. The tumor is implanted in the left thigh of the animals; The middle column (b,e,h,j) depicts the distribution of optical dyes as derived from FMT reconstruction. Images are shown as colored overlay on gray-scale anatomical MR images. The right column (c,f,i,l) shows the corresponding distribution of the MRI contrast agents from DCE/DSC-MRI. The first and second row (#1, #2) represent permeability measurement by Cy5.5-GdDOTA mixture while the third and forth (#3, #4) are perfusion measurement by AngioSense-Endorem mixture. Three views in each readout are displayed in transverse (T), coronal (C) and saggital (S) manners. For quantitative analysis (m,n) the average signal intensities of FMT and MRI measurements were compared for ROI located in the tumor tissue (ROI 1) and a second one in healthy tissue (ROI 2).

Parameters describing static vascular features such as the extracellular leakage space or the tumor blood volume could be estimated once the tissue and plasma concentrations of the imaging agents have reached their steady state. Values derived from pre- and post-contrast MRI and FMT data should yield comparable results to the final enhancement values derived from the dynamic uptake curves. MRI results reveal heterogeneity across the tumors with a high degree of vascularization at the tumor periphery and in some central regions (Fig. 4.8). In general, there was a good correlation between the distribution of GdDOTA and Endorem: regions displaying high blood volume also displayed significant vascular leakage. We also found good correspondence between the dye distribution derived from FMT and the MRI contrast agent distribution, although due to its limited spatial resolution and the blurring effect by the point-spread function in the reconstruction, FMT did not capture this heterogeneity to the same degree. Nevertheless, the comparison with MRI revealed that the centers-of-gravity of the fluorescent dye and MRI contrast agent distribution were essentially identical. Even though the FMT data presented source reconstruction artifacts at the surface of the imaging volume, the volume-averaged intensity values correlated well with the respective MRI results, in particular for the comparison of Cy5.5 versus GdDOTA. To achieve the resolution determined by the uptake kinetics of imaging agents (time resolution of the order of 1 s), dynamic measurements had to be carried out in the dFRI mode using single-point excitation. Obviously, the method does not provide 3D information on intratumoral tracer distribution and hence on tumor heterogeneity. On the other hand, FMT imaging is limited due to shortcomings of current data reconstruction algorithms (low spatial resolution, artifacts at the sample boundary, sample considered homogeneous). In this context, the use of prior information derived from structural MRI should improve the quality of the FMT reconstruction [17-20].

4.5 Conclusion

We have described a hybrid imaging setup for simultaneous fluorescence and MR imaging. Feasibility has been demonstrated by measuring the uptake of extracellular and intravascular imaging agents in a mouse tumor model. DCE-MRI is an accepted translational technique for evaluating, e.g., anti-angiogenic drugs and therefore constitutes a reference for the non-validated FMT/dFRI experiments. The direct comparison revealed that fluorescence-based measurements provide accurate (semi-) quantitative information of comparable quality to MRI (apart from inferior spatial resolution) and therefore constitutes an attractive low-cost alternative.

Nevertheless, quantification of stand-alone fluorescence data remains an issue as the quality of reconstruction depends on the availability of accurate geometric information. Also, time resolution for full 3D FMT data acquisition is currently not compatible with the kinetics of the physiological processes involved. On the other hand, many biological processes occur at a much slower scale. Using the

sensitive imaging method (FMT) to visualize molecular targets and their modulation by pharmacological interventions and the fast 3D method (MRI) to monitor their implications on physiological processes might constitute an attractive application of a true hybrid setup.

1. Judenhofer, M.S., H.F. Wehrl, D.F. Newport, C. Catana, S.B. Siegel, M. Becker, A. Thielscher, M. Kneilling, M.P. Lichy, and M. Eichner, *Simultaneous PET-MRI: a new approach for functional and morphological imaging.* Nature medicine, 2008. **14**(4): p. 459-465.
2. Zhang, K., H. Herzog, J. Mauler, C. Filss, T.W. Okell, E.R. Kops, L. Tellmann, T. Fischer, B. Brocke, and W. Sturm, *Comparison of cerebral blood flow acquired by simultaneous [15O] water positron emission tomography and arterial spin labeling magnetic resonance imaging.* Journal of cerebral blood flow & metabolism, 2014. **34**(8): p. 1373-1380.
3. Weis, S.M. and D.A. Cheresh, *Tumor angiogenesis: molecular pathways and therapeutic targets.* Nature medicine, 2011. **17**(11): p. 1359-1370.
4. Jahng, G.-H., K.-L. Li, L. Ostergaard, and F. Calamante, *Perfusion magnetic resonance imaging: a comprehensive update on principles and techniques.* Korean journal of radiology, 2014. **15**(5): p. 554-577.
5. Østergaard, L., *Principles of cerebral perfusion imaging by bolus tracking.* Journal of Magnetic Resonance Imaging, 2005. **22**(6): p. 710-717.
6. Rudin, M., P.M. McSheehy, P.R. Allegrini, M. Rausch, D. Baumann, M. Becquet, K. Brecht, J. Brueggen, S. Ferretti, and F. Schaeffer, *PTK787/ZK222584, a tyrosine kinase inhibitor of vascular endothelial growth factor receptor, reduces uptake of the contrast agent GdDOTA by murine orthotopic B16/BL6 melanoma tumours and inhibits their growth in vivo.* NMR in biomedicine, 2005. **18**(5): p. 308-321.
7. Eisenblätter, M., C. Höltke, T. Persigehl, and C. Bremer, *Optical techniques for the molecular imaging of angiogenesis.* European journal of nuclear medicine and molecular imaging, 2010. **37**(1): p. 127-137.
8. Wall, A., T. Persigehl, P. Hauff, K. Licha, M. Schirner, S. Müller, A. von Wallbrunn, L. Matuszewski, W. Heindel, and C. Bremer, *Differentiation of angiogenic burden in human cancer xenografts using a perfusion-type optical contrast agent (SIDAG).* Breast Cancer Research, 2008. **10**(2): p. R23.
9. Montet, X., J.-L. Figueiredo, H. Alencar, V. Ntziachristos, U. Mahmood, and R. Weissleder, *Tomographic fluorescence imaging of tumor vascular volume in mice.* Radiology, 2007. **242**(3): p. 751-758.
10. Ntziachristos, V., A. Yodh, M. Schnall, and B. Chance, *Concurrent MRI and diffuse optical tomography of breast after indocyanine green enhancement.* Proceedings of the National Academy of Sciences, 2000. **97**(6): p. 2767-2772.
11. Davis, S.C., K.S. Samkoe, K.M. Tichauer, K.J. Sexton, J.R. Gunn, S.J. Deharvengt, T. Hasan, and B.W. Pogue, *Dynamic dual-tracer MRI-guided fluorescence tomography to quantify receptor density in vivo.* Proceedings of the National Academy of Sciences, 2013. **110**(22): p. 9025-9030.
12. Ntziachristos, V., C.-H. Tung, C. Bremer, and R. Weissleder, *Fluorescence molecular tomography resolves protease activity in vivo.* Nature medicine, 2002. **8**(7): p. 757-761.
13. Choi, M., K. Choi, S.-W. Ryu, J. Lee, and C. Choi, *Dynamic fluorescence imaging for multiparametric measurement of tumor vasculature.* Journal of Biomedical Optics, 2011. **16**(4): p. 046008-046008-7.
14. Stuker, F., C. Baltes, K. Dikaiou, D. Vats, L. Carrara, E. Charbon, J. Ripoll, and M. Rudin, *Hybrid small animal imaging system combining magnetic resonance imaging with fluorescence tomography using single photon avalanche diode detectors.* IEEE transactions on medical imaging, 2011. **30**(6): p. 1265-1273.
15. Ntziachristos, V. and R. Weissleder, *Experimental three-dimensional fluorescence reconstruction of diffuse media by use of a normalized Born approximation.* Optics letters, 2001. **26**(12): p. 893-895.
16. Rudin, M., *Molecular imaging: principles and application in biomedical research*. 2005: Imperial College Press.
17. Darne, C., Y. Lu, and E.M. Sevick-Muraca, *Small animal fluorescence and bioluminescence tomography: a review of approaches, algorithms and technology update.* Physics in medicine and biology, 2013. **59**(1): p. R1.

18. Ale, A., V. Ermolayev, E. Herzog, C. Cohrs, M.H. De Angelis, and V. Ntziachristos, *FMT-XCT: in vivo animal studies with hybrid fluorescence molecular tomography-X-ray computed tomography.* Nature methods, 2012. **9**(6): p. 615-620.
19. Hyde, D., R. de Kleine, S.A. MacLaurin, E. Miller, D.H. Brooks, T. Krucker, and V. Ntziachristos, *Hybrid FMT–CT imaging of amyloid-β plaques in a murine Alzheimer's disease model.* Neuroimage, 2009. **44**(4): p. 1304-1311.
20. Schweiger, M. and S. Arridge, *The Toast++ software suite for forward and inverse modeling in optical tomography.* Journal of biomedical optics, 2014. **19**(4): p. 040801-040801.

Chapter 5

Conclusion & Outlook

5. 1 FMT-MRI - System Design and Characterization

Hybrid imaging systems that enable registering molecular information on an anatomical reference have become essential tools in biomedical application, spearheaded by the combination of positron emission tomography and x-ray computerized tomography (PET-XCT) [1, 2], which is meanwhile a clinically established workhorse. Apart from providing structural information, XCT information is also used to carry out the attenuation correction essential for reconstruction of the PET data. The combination FMT-XCT was a natural development based on the PET-XCT experience. Technical realization was relatively straightforward by integration of the optical components developed in the XCT gantry [3, 4]. As for PET-XCT, for FMT-XCT structural data was used both as anatomical reference and as prior information in the FMT reconstruction [3]. While advantages of a molecular imaging technology such as FMT with XCT are obvious, it is somewhat limited as conventional XCT only provides structural information based on the differences in beam attenuation by different tissues.

The combination of FMT and MRI appears certainly more versatile as MRI contrast depends on a variety of independent parameters and can easily be manipulated by the operator. On the other hand, it is technically more challenging, as the FMT information has to be collected from a sample located in a strong magnetic field. Different strategies have been considered to transmit light to the sample and collect information on the fluorescence distribution on the sample surface: remote excitation using a free laser beam or optical fibers to bring the light from the source to the sample, remote detection using a fiber bundle between the optic system close to the sample and the camera located outside of the magnetic fringe field, or on-site detection using camera systems not susceptible to the magnetic field.

Early hybrid FMT-MRI systems used a set of fibers for excitation and detection of the FMT signal [5]. These systems were impractical and needed a lot of space due to the fact that fibers were typically mounted in radial orientation with the associated geometrical constraint of the limited fiber bending radius. As a result these systems were usually used in combination with clinical MRI scanners, which however show inferior performance when imaging small animals such as mice due to lower field

strengths. Furthermore, as fibers for excitation were in a fixed arrangement there was no versatility regarding excitation schemes. This prompted the development of a FMT-MRI 1.0 system with a free beam-geometry [6, 7] designed as an insert for a small animal MRI scanner in our laboratories at UZH/ETH Zurich [8]. Inspired by hybrid PET MRI-systems, it used SPAD detectors for detection of the fluorescent signal inside the MRI magnet. Fluorescence dyes were excited with a laser transmitted in a free beam configuration to the sample inside the MRI, with scanning devices mounted on a support outside of the magnet's fringe field. The use of free laser beam design provided versatility regarding the excitation scheme and proof-of-principle of the concept including the use of light detectors inside the MRI could be established [8]. However, the system was still not very practical. Whenever the system was set up or the position of the FMT probe was moved, the laser beam had to be recalibrated in a cumbersome calibration procedure, such that it accurately scanned a ROI of typically 16 mm x 20 mm with a positional accuracy of better than 0.5 mm at a distance of approximately 3 meters from the scanning device. Moreover, a free laser beam is a safety-concern, in particular when working in the near-infrared spectral domain, as it might be reflected at metallic surfaces. Moreover, extra-care had to be taken to keep a corridor free for the laser beam to avoid interruption irrespective of the deflection angle, a challenge given the limited space inside the small animal MRI scanner. Apart from these limitations, the system also suffered from limitations in achievable FOV, sensor resolution and sensitivity.

5.1.1 Hybrid FMT-MRI 2.0

The FMT-MRI 1.0 constituted the starting point for the current PhD project, which had the objective of designing a compact hybrid system, which is easy to install and operate, does not require calibration steps prior to each experiment and should provide improved sensitivity at a better spatial resolution and cover a larger FOV. The first measure was to replace the SPAD detector by a CMOS camera of superior pixel resolution (1024x1024 instead of 128x128). Sensitivity was improved by cooling the sensor to temperatures below zero degrees to reduce dark current. This was achieved by an insulating housing made from hard foam, a thermoelectric cooler, a water-flushed aluminum cooling block and a copper fork for effective heat transfer between cooling block and image sensor. These measures improved the SNR of the camera by a factor of 3. Cross-talk between the MRI and the CMOS detector was eliminated by shielding the latter with copper tape, which further improved the camera sensitivity by a total factor of 4 and largely restored the SNR values of the MR signal to the values measured in the absence of the CMOS camera (improvement by a factor of 32). Moreover, line artifacts that were observed when collecting MRI images during CMOS detector operation, were avoided. Finally, redesign of the positioning mechanics allowed smooth, reproducible and accurate positioning of the FMT probe at the magnet center.

The improved performance of the hybrid FMT-MRI 2.0 system was demonstrated in a study of tumor angiogenesis. Signal changes in MRI and FMT were simultaneously monitored during intravenous infusion of cocktails of fluorescent dyes and MRI contras agents. Use of extracellular agents yielded information on the leakiness of tumor blood vessels (vascular permeability) while the use of intravascular imaging agents yielded information on perfusion and blood volume. Given the temporal resolution of seconds required dictated by the animals physiology, the FMT system was used for collecting 2D images only, while full 3D images were recorded at baseline and during steady state following tracer infusion [9]. The study showed that FMT/dFRI are valid low-cost alternatives for DCE-MRI commonly used for evaluating the vascularity leaks necessary for prediction of the effect of e.g. anti-angiogenic drugs and that the improvements of the FMT-MRI system provide the sensitivity required for biological studies.

Nevertheless, the study also highlighted deficiencies of the FMT-MRI 2.0 system, in particular the issue with system calibration that was still too time consuming for routine use. This prompted a complete redesign of the system. Avoiding calibration during individual experiments required the integration of the scanning devices into the FMT probe – scanning device, focal imaging plane (i.e. the adjustment by the objective lens system), and detector have to be arranged in fixed geometry. The FMT probe should allow for both reflection and transmission imaging and should be connected to the laser source with few (two) optical fibers (one for reflection, one for transmission mode). Within the encased FMT probe the laser light should propagate in free beam geometry. Given the space constraints miniaturized laser scanner devices have to be used and these devices must be insensitive to static and dynamic magnetic field. Such a concept drastically simplifies the handling of the system. Thus, very crucial steps have been taken in advancing the system from a proof-of-concept prototype for specialized people to a system that is accessible to biologist and many biomedical studies.

5.1.2 Hybrid FMT-MRI 3.0

Key elements of the FMT-MRI 3.0 system are the miniaturized gimbal-less two-axis MEMS mirrors using electrostatic actuation. In particular, their performance in the strong magnetic field of 9.4T of the small animal MRI scanner has to be carefully evaluated. Scanning of FMT source patterns inside the magnet were shown to be highly repeatable with a deviation of a few microns from their nominal positions, showing no or minimal susceptibility of the MEMS scanners to a static magnetic field. This completely changed when operating the mirrors during MRI data acquisitions. Massive deviations from nominal positions have been observed, which may be indicative of MEMS mirror oscillations likely arising from mechanical vibrations due to switching of magnetic field gradients. To warrant proper operation of the system additional improvements are required. Different avenues may be pursued. The easiest one is to mechanically isolate the FMT probe from the MRI system. The current probe fits

quite tightly with a minimal gap between the outer wall of the probe and the inner wall of the gradient system. Increasing this gap and mounting the probe on a support not connected to the magnet may reduce the problem. Alternatively, damping elements might be used to decouple the probe support from the magnet system. The use of MEMS mirrors with different vibrational susceptibility (different resonance frequency) might be considered. Finally, decoupling of the two measurements may be achieved by separating MRI and optical data collection in time, i.e. by using the recovery delay inherent in many MRI sequences, during which no gradients are switched, for acquiring the optical data, i.e. data are collected in an interleaved manner. The last options can be integrated in a straightforward manner by using of the TTL outputs of the MRI system to trigger data acquisition of the optical system. Yet in the long-term, true simultaneous acquisition should be envisaged.

A second important aspect was to replace the prototype detector systems by a commercial detector, which can be easily replaced if needed. With the board-level camera incorporating a novel sCMOS sensor, that fuses the benefits of both CCD and CMOS, we found an image detector with superior image quality. It offers extra high sensitivity, low readout noise, high frame rate, high resolution and high dynamic range. We modified the detector by removing magnetic parts to make it suitable for the MRI scanner. To further enhance sensitivity the sCMOS image sensor is cooled to 10°C with an in-house built cooling system consisting of a thermoelectric cooler and a water-flushed impermeable copper block. A temperature of 10°C was considered optimal as it largely reduced dark current noise, but still was higher than the dew point at our standard lab conditions. Therefore, additional measures to protect the sensor from vapor condensation were not required. To increase the field-of-view we used a fish eye lens as objective lens, and the intrinsic distortion corrected by data preprocessing. In order to mechanically protect the camera and to minimize interference with the MRI system, the camera was encased in a camera housing produced with a 3D-printer, which was designed to maximize the working distance between objective lens and the sample. We took special care to minimize holes and make seams overlap sufficiently wide to warrant efficient shielding. For shielding, a thin film of aluminum with 2.5 µm thickness was deposited on the inner side of the encasing using physical vapor deposition. In addition, the camera cable was shielded using aluminum foil, which further reduced cross-talk between the MRI system and the camera. Without shielding the SNR measure for a MRI phantom was reduced by a factor of 18x from SNR=181 to SNR=10 when the camera was running simultaneously. The shielding drastically improved the situation: simultaneous camera operation reduced the SNR in MRI only by a factor of 2.

Specific signal detection at the excitation and emission wavelength required the use of bandpass filters, which were incorporated using a drawer-mechanism, which simplifies mechanical switching of the filters. Currently only two bandpass filters are implemented, which is certainly a limitation of the

setup. A next extension would include either a filter wheel or even better tunable filters than can be electronically adjusted to the correct wavelength domain.

Simple operation implies a minimal number of connections to drivers and controllers. In our case, we had to connect the light source, the drivers for the two MEMS devices, the detector interface, the power supply for the thermoelectric cooler, and the radiofrequency preamplifier. In addition, tubes for water circulation had to be connected. All these connections were plug and play and easy to handle. Two single mode optic fibers (reflection and transmission mode) were used to connect the FMT probe to the laser source. Reflection and transmission mode operation can be selected using a fiber switch. The single-mode fiber reduces the divergence of the exiting beam around 25-fold compared to a multi-mode fiber and makes a compact and metal-less design possible with a 1.8 mm-diameter, cylindrical-shaped GRIN lens. The cylindrical shape of the GRIN lens simplifies focusing, yielding a clean approximatively Gaussian-shaped beam profile with a beam-diameter of 220 µm FWHM, a good correspondence to the point source model used in FMT.

The FMT probe has been designed such that the probe can be exchanged without interfering with any of the components relevant for FMT operation. The probe has two doors on both sides that can be opened, and the sample platform can be removed sideways in a drawer like fashion. The mouse platform comes with a water heating to keep mice warm under anesthesia, an incorporated anesthesia setup, and earbars can be flexibly positioned, such that any part of the mouse can be centered in the FOV of the hybrid system. Once the mouse is prepared, the drawer can be inserted into the FMT probe and the system is ready for the experiment.

Finally, an operating software tool has been developed in MATLAB that minimizes user interaction. Inputs required are the exposure time of the camera and the number and position of points in x and y direction; no inputs required for the laser power, which is kept at a fixed power and an OD filter is inserted for excitation mode. The program then automatically initiates the scanning of the source and takes an image at each source point.

Feasibility tests have revealed that in many respects the system fulfills the initial requirement. A FMT phantom experiment imaging a fluorescent dye (Cy5.5) inside a tissue-mimicking phantom at 3 mm depth revealed good sensitivity. Signal-to-noise ratio was found SNR=303 in reflection mode with a laser power of 390 nW and SNR=33 in transmission mode at a laser power of 3 mW using 1 mM concentration of the fluorescent dye Cy5.5. Based on the fact that both a laser power of six orders of magnitude higher and longer camera integration times could be readily used, it can be expected that a concentration below 1 mM by a similar order of magnitude can be detected at 3mm depth.

Preliminary data obtained in a mouse melanoma model measured with FMT-MRI 3.0 in reflection mode before and after injection of 20nmol ProSense680, a fluorescent marker of tumor associated protease activity, also indicated that the system is sensitive enough to detect molecular processes non-invasively. Label administration led to a significant increase in SNR from SNR=7.6 to SNR=30.

5.2 FMT-MRI 3.0 – Deficiencies and Potential Remedies

While FMT-MRI 3.0 constitutes a major improvement compared to its predecessor designs and many of the issues were solved, there are still some deficiencies that have to be addressed to achieve reliable performance.

1) The most important one is to control scanning during MRI data acquisition, which has already been addressed. While effects of the static magnetic field on MEMS operation appear negligible (apart from a constant shift, that can easily be accounted for), transient magnetic fields and more likely the mechanical vibrations associated with gradient switching severely compromise scanning accuracy. In fact, scanning during MRI data acquisition is not feasible and interleaved acquisition protocols must be considered synchronizing FMT and MRI scanning. Technological improvements addressing these aspects have been announced. The manufacturer of the MEMS mirrors has recognized the need for vibration-resistant MEMS mirrors and is currently working on solutions [10, 11]. New devices will probably be available soon potentially enabling true simultaneous hybrid FMT/MRI experiments. Alternatively, MEMS mirrors with smaller diameter might be used. This would increase the peak resonance frequencies of the device. Whether this would reduce the susceptibility to MRI associated vibrations remains to be shown. Finally, while care has been taken to avoid direct mechanical contact between the gradient system and the FMT probe, vibrations may still be transmitted via the linear guide system that is attached to the magnet. Hence, passive or even active damping of the FMT probe mount as a whole might be considered.
2) There are substantial power losses along the optic path and the power at the focal plane of the imager is of the order of 15% of the nominal laser power. This can be approached by either trying to optimize optical coupling at each junction or by increasing the power of the laser source (currently 100mW).
3) Decoupling between the FMT and MRI system may be optimized by introducing radiofrequency chimneys at all openings in the aluminum shield.

5.3 Outlook

There is a wide range of foreseeable applications for a hybrid fluorescence/MRI imaging that enables the annotation of high-resolution structural and functional information with molecular and cellular signatures. Examples include most fields of biomedical research, e.g. tumor biology and neurobiology (stroke, neurodegenerative diseases, etc). The major limitation is limited penetration of light into a turbid medium such as biological tissue. Depending of the wavelength used and the tissue examined light penetration to a few centimeters is feasible. This limits clinical application to superficially located structures (including internal surfaces when using endoscopic techniques [12]. For experimental research in mice light penetration is sufficient to penetrate the whole body [13]. While true hybrid operation is not mandatory when using the high resolution method as anatomical reference, it becomes critical when monitoring dynamic process with both modalities [9].

The hybrid FMT-MRI 3.0 system has been designed such that it can be combined with any MRI system provided the clear bore (inside the gradient system) is larger than 115mm. Of course, the resonance frequency of the transceiver coil has to be matched to the magnetic respective field strength. Another important design aspect was versatility, i.e. the system should be easily adaptable to different modes of operation. Apart from fluorescence imaging using either the reflection or transmission mode as described in this thesis, the system could also be used for image-guided manipulation of the biological system using laser light. This might include optogenetic stimulation of neural circuits by laser induced activation of channelrhodopsins [14] or photodynamic therapy by laser induced activation of photosensitive drugs [15]. Given the wide range of potential biomedical applications and given the fact that the focus of the thesis was the system development, focus of the rest of the section will be on imaging technology.

Camera technology is currently a rapidly evolving field and further improvements in sensitivity and dynamic range can be expected. The FMT systems can benefit from that making them faster and more sensitive, which would allow studying dynamic processes and monitoring biological events occurring at low abundance. New camera designs can be integrated in a straightforward manner.

The principle of optical tomography involves scanning of a light source across the sample surface and recording fluorescence images for each source position. Two aspects regarding scanning should be addressed: a) accuracy and b) speed.

a) Accuracy: For reconstruction purposes, the source position has to be known as accurately as possible. As already discussed, in order to facilitate system operation, the optical components have to be arranged in fixed geometry, which implies that the scanning devices have to be an integral part of the FMT probe located in the magnet. MEMS devices have been found attractive for the purpose

as they are small and do not contain magnetic components. Issues arising with the use of MEMS in an MRI system (vibrations) have been extensively discussed in the previous section.

b) Speed: FMT scanning is intrinsically slow due to its sequential nature. This is reminiscent of the early days of nuclear magnetic resonance (NMR) spectroscopy, during which NMR spectra were acquired by sweeping the resonance frequency across the spectral range. The introduction of Fourier NMR has completely changed the picture [16]. Whether similar principles may be used in FMT is currently unclear. Position dependent frequency encoding of the light sources might offer an option to allocate frequency specific signal components to source locations and thus enable parallelization of acquisition procedures (M. Rudin, personal communication).

Biological systems are complex and it is typically advisable to measure several parameters simultaneously. Fluorescence imaging methods may be multiplexed in a straightforward manner combining the use of several fluorophores with spectral deconvolution. There are different options available for a realization of such a multispectral device. The simplest one is to use a filter-wheel with several bandpass filters in combination with suitable lasers sources that can be selected using e.g. a fiber switch. A second option, which would save space, which is critical for the hybrid system as this has to be fitted into the FMT probe, would be to use a tunable filter [17]. A third option, which probably is the most flexible version, is using hyperspectral image sensors [18-20]. These image sensors have integrated filters at several wavelengths on each pixel. This would provide multispectral information, and FMT would strongly benefit from that because it enables simultaneous imaging of the excitation and emission mode, and therefore it removes accuracy loss due to motion of the mouse breathing or physiology changing, and it increases the acquisition speed. Difficulties might arise due to the fact that the excitation and fluorescence signals differ largely in intensity. This could be solved by adding up many images taken at short integration times avoiding saturation of the pixels. Hyperspectral cameras would also be useful to separate fluorophore specific from non-specific background signals thereby improving the signal to background ratio.

While this thesis focused on the hardware side of a hybrid FMT-MRI system, major developments are currently occurring regarding image reconstruction. The reconstruction problem of FMT is ill-posed and thus only iterative solutions are possible. Moreover, the object to be imaged is irregular shaped and of heterogeneous composition with many tissue interfaces at which transmission and reflection effects occur. Incorporation of prior structural information enables better confinement of the problem and thus should yield improved reconstruction results. The spatial distribution of optical absorption and scattering coefficients can be determined based on the tissue classification derived from MRI. Care has to be taken during the regularization process not to overfit the data and introduce bias. In addition, a device with FMT reconstruction done simultaneously with FMT imaging would enhance the usability

of the system. This could be achieved with a reduced number of FMT sources and would require fast computation. It could help to obtain a better control and increased flexibility during FMT acquisition and make it possible to search for accumulation of fluorescent dye in the body and allow to increase the data acquired in that location. In the current discussion we have focused on aspects related to fluorescence tomography. Yet the design is also suited for other molecular imaging applications such as bioluminescence and Raman hybrid imaging [21, 22]. For bioluminescence imaging, only the camera module is required as light is generated by a chemiluminescence, and hence the technical issues discussed related to mechanical vibrations are not relevant. The important criterion is a light tight encasing as any stray light would be detrimental. Hybrid bioluminescence-XCT systems are currently commercially available (IVIS series, Perkin-Elmer Inc.; Xtreme, Bruker GmbH) and are extensively used in biomedical research [23, 24]. For more detailed information on Raman spectroscopy and imaging the reader is referred to the literature [25]. The system requirements for Raman imaging are largely compatible with the design of FMT-MRI 3.0: key elements are laser source, scanning device (for spatial encoding) and a sensitive detector module, so minor adaptations will be unavoidable.

5.4 Final Conclusions

In summary, this thesis describes the development and characterization of the novel hybrid FMT-MRI system (FMT-MRI 3.0). From its first version (FMT-MRI 1.0 system), used for proof-of-concept but impractical for daily operation, the system evolved to a completely redesigned hybrid FMT-MRI 3.0 system with massively improved handling and overall improved camera performance fitting the system for routine use. A major change was the introduction of a fixed geometry arrangement that eliminated time-consuming system calibration and considerably improved handling and robustness of the system. Both camera cooling and shielding to avoid electromagnetic interference (EMI) were found essential. A compact device for scanning the laser beam across the sample such as the MEMS laser scanner was found ideal for source scanning. However further optimization is required to reduce vibration susceptibility for simultaneous FMT-MRI imaging. The development of the system demanded compact engineering and careful selection of materials and components for MRI compatibility.

The hybrid FMT-MRI 3.0 system combines multimodality with easy handling and carries great potential for molecular imaging in small animals with various applications in basic biomedical research such as detection and characterization of a disease phenotype and evaluation of novel therapies (pharmacokinetic and pharmacodynamics studies).

1. Beyer, T., D.W. Townsend, T. Brun, and P.E. Kinahan, *A combined PET/CT scanner for clinical oncology.* The Journal of nuclear medicine, 2000. **41**(8): p. 1369.
2. Kinahan, P., D. Townsend, T. Beyer, and D. Sashin, *Attenuation correction for a combined 3D PET/CT scanner.* Medical physics, 1998. **25**(10): p. 2046-2053.
3. Ale, A., V. Ermolayev, E. Herzog, C. Cohrs, M.H. De Angelis, and V. Ntziachristos, *FMT-XCT: in vivo animal studies with hybrid fluorescence molecular tomography-X-ray computed tomography.* Nature methods, 2012. **9**(6): p. 615-620.
4. Schulz, R.B., A. Ale, A. Sarantopoulos, M. Freyer, E. Soehngen, M. Zientkowska, and V. Ntziachristos, *Hybrid system for simultaneous fluorescence and x-ray computed tomography.* IEEE transactions on medical imaging, 2010. **29**(2): p. 465-473.
5. Davis, S.C., B.W. Pogue, R. Springett, C. Leussler, P. Mazurkewitz, S.B. Tuttle, S.L. Gibbs-Strauss, S.S. Jiang, H. Dehghani, and K.D. Paulsen, *Magnetic resonance–coupled fluorescence tomography scanner for molecular imaging of tissue.* Review of Scientific Instruments, 2008. **79**(6): p. 064302.
6. Deliolanis, N., T. Lasser, D. Hyde, A. Soubret, J. Ripoll, and V. Ntziachristos, *Free-space fluorescence molecular tomography utilizing 360 geometry projections.* Optics letters, 2007. **32**(4): p. 382-384.
7. Ripoll, J., R.B. Schulz, and V. Ntziachristos, *Free-space propagation of diffuse light: theory and experiments.* Physical review letters, 2003. **91**(10): p. 103901.
8. Stuker, F., C. Baltes, K. Dikaiou, D. Vats, L. Carrara, E. Charbon, J. Ripoll, and M. Rudin, *Hybrid small animal imaging system combining magnetic resonance imaging with fluorescence tomography using single photon avalanche diode detectors.* IEEE transactions on medical imaging, 2011. **30**(6): p. 1265-1273.
9. Ren, W., A. Elmer, D. Buehlmann, M.-A. Augath, D. Vats, J. Ripoll, and M. Rudin, *Dynamic Measurement of Tumor Vascular Permeability and Perfusion using a Hybrid System for Simultaneous Magnetic Resonance and Fluorescence Imaging.* Molecular Imaging and Biology, 2016. **18**(2): p. 191-200.
10. Milanovic, V., A. Kasturi, and J. Yang. *Novel fluidic packaging of gimbal-less MEMS mirrors for increased optical resolution and overall performance*. in *SPIE Defense+ Security*. 2016. International Society for Optics and Photonics.
11. Milanović, V., A. Kasturi, J. Yang, Y.R. Su, and F. Hu. *Novel packaging approaches for increased robustness and overall performance of gimbal-less MEMS mirrors*. in *SPIE OPTO*. 2017. International Society for Optics and Photonics.
12. Tjalma, J.J., P.B. Garcia-Allende, E. Hartmans, A.G.T. van Scheltinga, W. Boersma-van Ek, J. Glatz, M. Koch, Y.J. van Herwaarden, T.M. Bisseling, and I.D. Nagtegaal, *Molecular fluorescence endoscopy targeting vascular endothelial growth factor a for improved colorectal polyp detection.* Journal of Nuclear Medicine, 2016. **57**(3): p. 480-485.
13. Hyde, D., R. de Kleine, S.A. MacLaurin, E. Miller, D.H. Brooks, T. Krucker, and V. Ntziachristos, *Hybrid FMT–CT imaging of amyloid-β plaques in a murine Alzheimer's disease model.* Neuroimage, 2009. **44**(4): p. 1304-1311.
14. Lee, J.H., R. Durand, V. Gradinaru, F. Zhang, I. Goshen, D.-S. Kim, L.E. Fenno, C. Ramakrishnan, and K. Deisseroth, *Global and local fMRI signals driven by neurons defined optogenetically by type and wiring.* Nature, 2010. **465**(7299): p. 788-792.
15. Dolmans, D.E., D. Fukumura, and R.K. Jain, *Photodynamic therapy for cancer.* Nature reviews cancer, 2003. **3**(5): p. 380-387.
16. Ernst, R.R. and W.A. Anderson, *Application of Fourier transform spectroscopy to magnetic resonance.* Review of Scientific Instruments, 1966. **37**(1): p. 93-102.
17. Hirokubo, N., H. Komatsu, N. Hashimoto, M. Sonehara, and T. Sato, *Wideband visible wavelength range MEMS Fabry–Perot tunable filter with highly accurate calibration system.* IEEE Sensors Journal, 2013. **13**(8): p. 2930-2936.
18. IMEC. *Hyperspectral Imaging*. [cited 2017 June 22th]; Available from: https://www.imec-int.com/en/hyperspectral-imaging.

19. Luthman, A.S., S. Dumitru, I. Quiros-Gonzalez, J. Joseph, and S.E. Bohndiek, *Fluorescence hyperspectral imaging (fHSI) using a spectrally resolved detector array.* Journal of Biophotonics, 2017.
20. Kaluzny, J., H. Li, W. Liu, P. Nesper, J. Park, H.F. Zhang, and A.A. Fawzi, *Bayer filter snapshot hyperspectral fundus camera for human retinal imaging.* Current eye research, 2017. **42**(4): p. 629-635.
21. Amendola, V., S. Scaramuzza, L. Litti, M. Meneghetti, G. Zuccolotto, A. Rosato, E. Nicolato, P. Marzola, G. Fracasso, and C. Anselmi, *Magneto-Plasmonic Au-Fe Alloy Nanoparticles Designed for Multimodal SERS-MRI-CT Imaging.* Small, 2014. **10**(12): p. 2476-2486.
22. Cialla, D., A. März, R. Böhme, F. Theil, K. Weber, M. Schmitt, and J. Popp, *Surface-enhanced Raman spectroscopy (SERS): progress and trends.* Analytical and bioanalytical chemistry, 2012. **403**(1): p. 27-54.
23. Van Oosten, M., T. Schäfer, J.A. Gazendam, K. Ohlsen, E. Tsompanidou, M.C. De Goffau, H.J. Harmsen, L.M. Crane, E. Lim, and K.P. Francis, *Real-time in vivo imaging of invasive-and biomaterial-associated bacterial infections using fluorescently labelled vancomycin.* Nature communications, 2013. **4**: p. 2584.
24. Lim, E., K. Modi, A. Christensen, J. Meganck, S. Oldfield, and N. Zhang, *Monitoring tumor metastases and osteolytic lesions with bioluminescence and micro CT imaging.* Journal of visualized experiments: JoVE, 2011(50).
25. McVeigh, P.Z., R.J. Mallia, I. Veilleux, and B.C. Wilson, *Widefield quantitative multiplex surface enhanced Raman scattering imaging in vivo.* Journal of biomedical optics, 2013. **18**(4): p. 046011-046011.

Abbreviations

ABS	Acrylonitrile Butadiene Styrene
AIC	Animal Imaging Center
API	Application Programming Interface
CAD	Computer Aided Design
CCD	Charge-Coupled Device
CMOS	Complementary Metal-Oxide-Semiconductor
CW	Continuous Wave
DCE-MRI	Dynamic Contrast Enhanced-MRI
DSC-MRI	Dynamic Susceptibility Contrast MRI
dFRI	Dynamic Fluorescence Reflactance Imaging
DOT	Diffuse Optical Tomography
DSNU	Dark Signal Non-Uniformity
EGFR	Epithelial Growth Factor Receptor
EMC	Electromagnetic Compatibility
EMI	Electromagnetic Interference
EPI	Echo-Planar Imaging
FID	Free Induction Decay
FLASH	Fast Low Angle Shot
FMT	Fluorescence Molecular Tomography
FOV	Field-of-View
FPGA	Field-Programmable Gate Array
FWHM	Full Width at Half Maximum
FRI	Fluorescence Reflectance Imaging

GRIN	Graded Index
HR	High resolution
MEMS	Microelectromechanical Systems
MRI	Magnetic Resonance Imaging
NIR	Near Infrared
OD	Optical density
PBS	Phosphate Buffered Saline
PCB	Printed Circuit Board
PE	Photoelectric Effect
PET	Position Emission Tomography
PVD	Physical Vapor Deposition
PRNU	Pixel Response Non-Uniformity
RARE	Rapid Acquisition with Relaxation Enhancement
RF	Radio Frequency
RM	Reflection Mode
RMS	Root Mean Square
ROI	Region of Interest
rTBV	Relative Tumor Blood Volume
RTE	Radiative Transfer Equation
sCMOS	scientific CMOS
SDK	Software Development Kit
SEM	Scanning Electron Microscopy
SNR	Signal-to-Noise Ratio
SPAD	Single Photon Avalanche Diode
SPECT	Single-Photon Emission Computed Tomography

TE	Echo Time
TEC	Thermoelectric Cooler
TM	Transmission Mode
TR	Repetition Time
USAF	US Air Force
3D	Three-Dimensional

Acknowledgments

I would like to thank everybody who contributed to this PhD thesis, especially to

- Prof. Markus Rudin for being my supervisor and his profound support during my thesis. I could ask any questions and always found an open ear
- Prof. Martin Wolf for being my co-advisor and for his helpful discussions and advice during the progress reports
- Dr. Mark Augath for his engineering input and his support with all kind of MRI-related matters
- Markus Küpfer for the many shared hours in the workshop, our discussions about feasibility of mechanic designs and his productions of pieces for the hybrid FMT MRI systems
- Wuwei Ren for being my project partner. He focused on the FMT reconstruction part. Thank you for the valuable discussions and inputs. We spent many hours together in the lab, at conferences and discussing papers
- Dr. Katerina Dikaiou and Dr. Florian Stuker for initiating me to FMT and introducing me to the AIC lab
- Dr. Felix Schlegel, Christian Horea and Dr. Markus Vaas for many valuable technical inputs
- Jürg Meyer for his efficient and professional support related to the PCO camera
- David Beyeler for his support related to CSEM camera
- Dr. Qiong Ye for the nice discussions at many enjoyable beverages
- Bruno Willi for his valuable IT support
- Dr. Aniña Pescatore and Yajur Arora for proofreading parts of my thesis manuscript
- Ruedi Elmer, Lotti Kölliker, Norman Juchler and Thomas Walser for their support and inputs
- The AIC group for the nice atmosphere, many discussions and inputs
- All my friends and my family for their support

The project was financially supported by the National Competence Center for Biomedical Imaging (NCCBI).